

**ALL-MICROWAVE CONTROL OF HYPERFINE STATES IN ULTRACOLD
SPIN-1 RUBIDIUM**

A Dissertation
Presented to
The Academic Faculty

By

Matthew J. Boguslawski

In Partial Fulfillment
of the Requirements for the Degree
Doctor of Philosophy in the
School of Physics

Georgia Institute of Technology

December 2019

Copyright © Matthew J. Boguslawski 2019

**ALL-MICROWAVE CONTROL OF HYPERFINE STATES IN ULTRACOLD
SPIN-1 RUBIDIUM**

Approved by:

Professor Michael S. Chapman,
Advisor
School of Physics
Georgia Institute of Technology

Professor Colin Parker
School of Physics
Georgia Institute of Technology

Professor Martin Mourigal
School of Physics
Georgia Institute of Technology

Professor Brian Kennedy
School of Physics
Georgia Institute of Technology

Professor Gregory Durgin
School of Electrical and Computer
Engineering
Georgia Institute of Technology

Date Approved: August 22, 2019

You can't stop the waves, but you can learn to surf.

Jon Kabat-Zinn

To my Friends, Family, and Everyone dear to me.

ACKNOWLEDGEMENTS

This thesis describes some, not all, of the research projects I worked on during my PhD studies. During this PhD, I have learned an incredibly diverse set of skills including how to learn about, approach, and solve new or complicated problems. This PhD represents the culmination of a great deal of hard work and learning. Along the way, I was impacted by numerous people—more than I'll be able to name here. These people have helped in countless ways including assisting my learning, helping with my experiments, aiding in my personal development, supporting me, cheering me up and keeping me happy, or providing me with fun or creative outlets while I was busy or stressed working on this PhD. I would like to acknowledge and thank everyone involved in my PhD journey. Thank you all!

Several individuals at Georgia Tech played significant roles in my PhD journey. I would like to acknowledge my advisor, Mike Chapman. Mike was easily available to support in whatever way he was capable. Mike has a propensity for asking questions which lead to new, interesting topics to consider. One particularly appreciated habit of Mike: when he first comes into the lab to check on you and the experiment, he always asks how you are. Then he actually listens, which determines the content of conversation that follows. On good days, Mike starts a conversation about many ideas of interesting topics to study in the experiment. On bad days, Mike offers some words of encouragement and support. Thank you for helping me accomplish this PhD. I would additionally like to acknowledge and thank all the committee members who reviewed this thesis. I'd also like to acknowledge the NSF for funding the projects I have worked on during this PhD.

I have worked with and learned so much from many students during my time in this lab. Thai Hoang had an incredible driving energy and thorough knowledge of the experiment and related physics. Thai was around to help me during my first year in the lab. From Martin Anquez, I learned how to run the BEC experiment. I learned all the voodoo that kept the spreadsheets of the experimental time sequences functional (which kept the experiment

running). I learned all the lab lore and many lab superstitions, along with a great deal of important physics relevant to the experiment. Martin also made sure the lab members would get out for lunch (Taco Tuesdays!) whenever possible, which was always appreciated.

Bharath H. M. was my classmate and labmate for the majority of my time in the lab. Bharath is a remarkable physics and mathematician, yet extraordinarily humble. Bharath was always willing to stop and explain concepts or help solve problems. I worked closely with Bharath to rebuild the BEC experiment (twice). Together, Bharath and I worked through an incredible number of different problems, and we kept the lab moving forward while it was only the two of us running the experiment.

A couple of graduate students have joined the lab since Bharath and I arrived. Maryrose Barrios has been a friendly face around the lab. Maryrose is willing to work the late shift to help finish data sets started during the day. Her work is quite meticulous and thorough. Maryrose was always happy to read through things I had written and would freely share words of encouragement. Lin Xin has been quite a joy to have in the lab. Lin joined having little experience with the hands-on aspects of experimental physics; but this did not stop Lin. Since joining the lab, Lin has become quite adept with all aspects of the experiment, from the hardware and lasers, to the control system and data analysis. Lin is a very reliable worker who will grind through hours of data acquisition without complaint. It has been a pleasure teaching and working with Lin. Lin and Maryrose were a tremendous source of help for the experiments described in this thesis.

Additionally, I'd like to acknowledge all of my classmates, with whom I worked through all of the core physics classes during the first year of the PhD program. We shared many good times, many stressful times, and many late nights struggling through tricky homework problems. Thank you all!

During the years working towards this PhD, there were many exciting successes, along with many stresses and frustrations. There were many people outside of the lab that need to be acknowledged. These are the people with whom I could celebrate my successes, and

who provided essential encouragement and support, as well as much-needed distractions and stress relief.

My parents need a big thank you for all their support throughout my years at tech. The rest of my family, as well. Mom, Dad, Chris, Brian, Colin and Shae—thank you for all your support and encouragement over the years. My family has been an essential support system during this final (particularly stressful) step of writing up my work in this thesis.

Thank you to all my roommates over the years. Byron— we had a good stay in quite the budget apartment. Dan and Yoolim, we had a couple great years in our tiny apartment. To my current housemates Shae, Matt, Maddie, and Jackie— I’ve greatly enjoyed living with all of you. We’ve shared many good times, and you were all there for support whenever I was having a hard time. I know you all will be beyond happy when this thesis is (actually) complete and submitted. Thank you all!

I’d like to acknowledge Alison Tseng, who offered a great deal of support during my first years of classes and working in the lab.

During my PhD, dance was an essential creative outlet and opportunity for exercise for me. Many of the wonderful people I met though dance impacted me greatly while I was pursuing my PhD. My dance coaches—Yuliya Besarab and Sergiy Samchynskyy. Yuliya has known me through nearly my whole time at Georgia Tech. Sergiy, who is constantly busy, took us on as his only amateur couple and before too long was making lesson time for us a priority. From both Sergiy and Yuliya, I have learned much more than expected. I’ve learned how to dance. But I’ve also learned about myself, about life, about how to think about complicated problems. How to *almost* rumba walk correctly. One of the greatest aspects I appreciate about both Sergiy and Yuliya is their willingness to explain concepts in full detail, in the exact way they think about whichever concept. They will take the time to make sure you understand deeply the why behind doing something so well that you hardly need the instruction of how it’s done any longer. I have not had an experience like this from a teacher anywhere else. I could go on, but thank you Sergiy and Yuliya!

To Connie Liu—you were the first person I'd run to in celebration of the good times and accomplishments, and you have been there to support me during so many difficult times—thank you! I have learned so much with Connie, and together we shared countless unforgettable moments. We have worked long and hard for impressive accomplishments together. We even placed first in Championship-level international standard at a national ballroom dance championship while we were both busy working to finish our PhDs, crushing a goal we set for ourselves! Together, we explored the opposite side of the world together, forming more unforgettable memories. You have been such a source of inspiration for me and a tremendous source of encouragement during my PhD. Thank you for ALL the ways you have helped!

Thank you as well to all the ballroom dancers at Georgia Tech. Thank you to Daniel Boman and Kelsey Johnson for rebuilding the club from the ground up. Thank you to Lana Hanlon and Alexander Sun for all the game nights and movie nights. Thank you to everyone in the club—these years would not have been the same without the GTBDC and all its members!

TABLE OF CONTENTS

Acknowledgments	v
List of Tables	xiii
List of Figures	xiv
Chapter 1: Introduction and Background	1
1.1 Quantum State Control	4
1.2 State Control in Chapman Labs	9
Chapter 2: Technical and Apparatus Details	11
2.1 The BEC Aparatus	11
2.1.1 Vacuum Chamber	11
2.1.2 Magnetic Field Coils and Control	20
2.1.3 BEC Experiment Sequence	21
2.1.4 Measurement via Imaging of the BEC	22
2.2 Microwave Antenna Design and Setup	26
2.2.1 Antenna Testing	27
2.2.2 Antenna Designs and Hardware	31

Chapter 3: Using Circularly Polarized Microwaves to Selectively Drive Hyper-fine Transitions	41
3.1 Abstract	41
3.2 Introduction	41
3.2.1 Motivation and Background	41
3.2.2 Overview of Study	47
3.2.3 Preliminaries	48
3.2.4 Bias Field Direction vs Transition Strength	59
Chapter 4: Circularly Polarized Microwaves – Experimental Measurements . .	64
4.1 Experimental Procedure	64
4.1.1 Zeroing the Field	65
4.1.2 Atoms as a Microwave Field Measure	66
4.1.3 Nulling the Field – Clock Transition	68
4.2 Polarization Selection of σ -Transitions	71
4.2.1 Larmor Decoherence – Fitting Slow Rabi Rates for Blocked Transitions	72
4.2.2 Angular Dependence of Bias Field	78
4.3 All-Microwave Λ Transitions	81
4.3.1 Λ Transition – Simulations	83
4.4 Λ Transition – Experiment	87
4.4.1 Holonomic, Non-Adiabatic Gate	97
4.5 Low Field Microwave Transitions	98
4.5.1 Low Field Simulations	98

4.5.2	Low Field Selectivity	99
4.6	Concluding Remarks	103
Chapter 5: Tripod Transition		105
5.1	Tripod Transition– Theory	106
5.2	Special Case: Λ Transition	109
5.3	Example Bright State	110
5.4	Adiabatic vs Non-Adiabatic Evolution	111
5.5	Attempts at a Tripod Implementation	113
5.5.1	Light Shift	114
5.5.2	Calculation for Light Shift and Scattering Rate	115
5.5.3	Multi-Tone Microwave Setup	123
5.6	Concluding Remarks	127
Chapter 6: Conclusion		129
6.1	Circularly Polarized Microwave Manipulations	129
6.2	The Tripod	130
6.3	The End.	130
Appendix A: The Magnetic Dipole Transition Matrices		132
Appendix B: Temporal Dark MOT Sequence		134
Appendix C: Circuits Used in Apparatus		135
C.1	IGBT Circuit	135

C.2	60Hz Line Trigger	137
C.3	Unity Gain Buffer Circuit	138
C.4	Slave Laser Current Modulation Circuit	139
Appendix D: Fluorescence Collection Calculation		141
Appendix E: Bakeout Procedure		143
References		154

LIST OF TABLES

2.1	Typical powers in each MOT beam. These are labeled by fiber designations as can be seen in Figure 2.5.	17
2.2	Helical antenna design parameters for 6.834 GHz antenna operating in axial mode. This antenna produces circularly polarized radiation.	36
4.1	A tabulation of the Rabi frequencies measurements seen in Figures 4.4—4.7.	77
5.1	The eigenenergies and corresponding eigenvectors for Hamiltonian 5.1 . . .	108
5.2	Transition matrix elements for the π polarization $F = 2 \rightarrow F'$ D1 transitions in ^{87}Rb . For these transitions, the initial and final m_F are equal ($m'_F = m_F$).	117
5.3	Light shift at 200 MHz detuning	118
5.4	Light shift at 50 MHz detuning	118
5.5	Light shift at 25 Hz detuning	119

LIST OF FIGURES

1.1	The stimulated Raman transition showing the Λ -type level structure. The single-photon coupling strengths for this transition are Ω_1 and Ω_2 , with a resulting two-photon Rabi rate indicated as $\Omega_{2\gamma}$. This shows the case of two-photon resonance, where both coupling fields are detuned from the excited state transition by the same amount δ	6
1.2	The STIRAP transition. (left) The Λ -type level structure. The single-photon coupling strengths for this transition are Ω_1 and Ω_2 . This shows the two-photon resonance case, where both coupling fields are detuned from the excited state transition by the same amount δ . (right) An illustrative schematic of time-dependent coupling strengths for a STIRAP transition from the initial state $ 1\rangle$ to the final state $ 2\rangle$, portraying the counter-intuitive ordering for the pulses.	7
2.2	Several views of the CAD models for the lens mounts. (a) The CO_2 laser input lens assembly. The lens is a 27.94 mm diameter, 38.1 mm effective focal length zinc-selenide aspheric lens from II-VI Infrared, Inc., anti-reflection coated for 10.6 μm . (b) The imaging lens assembly. The lens is a Thorlabs AL3026-B. (c) The CO_2 laser output lens assembly. The lens is a Thorlabs LE7981-F, a zinc-selenide meniscus lens.	14
2.1	The science chamber—the Kimball physics spherical octagon chamber within which the BEC experiments are performed. (a) A photo of the inside of the chamber with all components in place. (b) A CAD model of the science chamber, pumping section not shown. (c) A cut-away view of the CAD model showing the internal lens mounts and hardware.	14

2.3	A view of the BEC apparatus vacuum chamber. The spherical octagon is in the foreground of the image with the pumping section connected off the back. This is a version Bharath H. M. and I built before building the current version of the apparatus. This shows the similar pumping setup and arrangement to science chamber compared to the current version. In quite a surprise turn of events, the Rb dispenser in this chamber was depleted, leading to low atom numbers in the experiment and consequently the newest version of the chamber.	15
2.4	Schematic representation of the chamber. The x and z axes are denoted, the y axis is out from the page. One bias coil of each pair is indicated. . . .	16
2.5	The modification to the optical fiber setup for the MOT lasers. Each fiber illuminates one axis for the MOT; these fibers are labeled as “MOT 1,” “MOT 2,” and “MOT 3.” The MOT 1 fiber is used for the vertical MOT beam. The MOT 2 and MOT 3 fibers are the two horizontal axes.	18
2.6	The beam path for the D1 light shift laser setup	20
2.7	Several fluorescence images stitched together vertically to show the time-of-flight expansion within the Stern-Gerlach field. The images were taken at incremental times following the release of the atoms from the trap and are shown in false-color to enhance the visibility of contrast. The text above each frame states how long the Stern-Gerlach coils have been switched on (left, “ms SG Duration”) and how long before the probe time each frame was taken (right, “ms before probe”). In each frame, the $m_F = -1$, $m_F = 0$, and $m_F = +1$ components of $F = 1$ are on the left, center, and right of the image, respectively. The center of adjacent populations are separated by $\approx 550 \mu\text{m}$ at 19 ms.	24
2.8	(a) A schematic of the $4f$ imaging setup. Two lenses are used to image light from the atoms onto the camera sensor. The first lens, the “imaging lens” is inside the chamber, one focal length ($f_1 = 26 \text{ mm}$) away from the atomic cloud (red dot). This lens images the atoms at $+\infty$. The second “re-imaging lens” with focal length $f_2 = 100 \text{ mm}$ images the atoms onto the camera sensor. The total length of the optical path (on the principal axis) is the sum of two times each focal length ($2f_1 + 2f_2$), a total of four focal lengths. (b) A schematic of the modified imaging setup. Compared to (a), the separation between the two lenses is reduced (d_1).	26

2.9	Setup used for crossed linear polarization testing, i.e. the “linear analyzer test.” The antenna on the bottom of the image (the circular waveguide antenna constructed from copper tube) is the receiver antenna, mounted on an angular rotation mount. The antenna at the top is a log-periodic antenna (green, triangular) and would be the transmitting antenna in this case. Cable connections to antennas not shown.	30
2.10	Photographs of several antenna types. (a) A BNC mounted half-wave dipole antenna for 6.834 GHz. (b) A dual cylindrical waveguide antenna (c) A WA5VJB log-periodic antenna (d) An Archimedean spiral antenna	33
2.11	The Matlab Antenna Designer model of the helical antenna.	37
2.12	The Matlab generated 3D radiation profile. The color scale shows the gain in dB.	38
2.13	An example of the paper layout used to form the helical antenna. The blue rectangles are cut out and the two “1/4” rectangles are folded along the vertical lines. The holes are spaced vertically to match the pitch of helix at 1/4 turn (90°). The dots are punched out as guide holes for the helix of wire. The three layouts are used together to hold the geometry of the helix.	38
2.14	An assembled helical antenna (3 views). The paper form from Figure 2.13 can be seen supporting the helical coil.	39
3.1	The ground state $5^2S_{1/2}$ hyperfine energy levels in rubidium-87. The approximate energy spacings are labeled in terms of $\Delta \approx 700$ Hz/mG, giving the shift due to the linear Zeeman effect of the transitions compared to the clock transition. The spacing between each of the m_F levels for $F = 1$ and $F = 2$ are $\Delta_1 = 702.4$ Hz/mG and $\Delta_2 = 699.6$ Hz/mG, respectively.	50
3.2	The ground state hyperfine structure. The matrix elements from matrix Eqn. 3.12 are shown with the corresponding σ_+ transitions, illustrating the selected transitions corresponding to the non-zero matrix elements for microwave transitions for a σ_+ polarized microwave field.	56
3.3	An illustration showing the plane of circulating microwave magnetic field (Gray plane with red field vector) and the coordinate system as seen by the atoms rotated about the x -axis by the angle θ . The z -axis represents the bias field direction and the quantization axis for the atoms.	61
3.4	The angular dependence of the σ_{\pm} and π transitions compared to the field direction. The curves show the amplitude of the e_+ microwave field projected into the atomic basis as the field is rotated about the x -axis.	62

4.1	Measurement of the magnetic field squared as the trim field was scanned along the trim- y axis. The least squares fit (curve shown in red) gives the magnetic field parameters listed in the table.	66
4.2	Malus's law data measured using a linearly polarized, circular waveguide antenna, measured at angles between the field orientations of the minimum (0°) and maximum ($\pm 90^\circ$) Rabi rates. The inset on left indicates the angle θ between the microwave magnetic field direction ($B_{\mu w}$) and the bias field direction (B_z). The inset on right shows an expanded view around the minimum frequency. The smallest frequency which could be determined was 30 ± 20 Hz. The maximum frequency measured was 4220 ± 30 Hz. . .	68
4.3	Data showing the dependence of the clock transition frequency vs the bias field offset angle. The 0° angle is set to be the minimum frequency. This data was taken with a 200 mG bias field. The black curve shows the best fit to the theory. The red curves show offsets of $\pm 1^\circ$ for comparison. The minimum reported Rabi rate was 90 ± 20 Hz.	69
4.4	Fast, polarization selected σ_+ , Δ_+ transition: $ 1, 0\rangle \rightarrow 2, +1\rangle$. (Top) The transition is highlighted in green. (Bottom) The measured Rabi cycle. The point markers show measured values (error bars show one standard deviation). The curve shows the least-squares fit. The best fit Rabi frequency in ρ_0 was 13717 ± 19 Hz	73
4.5	Slow, polarization blocked σ_- , Δ_- transition: $ 1, 0\rangle \rightarrow 2, -1\rangle$. (Top) The transition is highlighted in dashed red. (Bottom) The point markers show measured values (error bars show one standard deviation). The curve shows the least-squares fit for the interval from $0 \mu s$ to $500 \mu s$. The best fit Rabi frequency in ρ_0 was 303 ± 4 Hz	74
4.6	Fast, polarization selected σ_- , Δ_- transition: $ 1, 0\rangle \rightarrow 2, -1\rangle$. (Top) The transition is highlighted in green. (Bottom) The point markers show measured values (error bars show one standard deviation). The best fit Rabi frequency in ρ_0 was 13717 ± 38 Hz	75
4.7	Slow, polarization blocked σ_+ , Δ_+ transition: $ 1, 0\rangle \rightarrow 2, +1\rangle$. (Top) The transition is highlighted in dashed red. (Bottom) The point markers show measured values (error bars show one standard deviation). The curve shows the least-squares fit for the interval from $0 \mu s$ to $500 \mu s$. The curve shows the least-squares fit. The best fit Rabi frequency in ρ_0 was 339 ± 6 Hz . . .	76
4.8	(<i>duplicate</i>) The angular dependence of the σ_\pm and π transitions compared to the field direction. The curves show the amplitude of the e_+ microwave field projected into the atomic basis as the field is rotated about the x -axis. .	80

4.9	The angular dependence of the σ_{\pm} transition on the field direction (c.f Figure 4.8). The markers show the measured Rabi rates with error bars of one standard deviation (error bars smaller than the point markers). At 0° , ratio of Rabi rates is $1/43$. The curves show the theory with the amplitude set by the maximum measured Rabi frequency and 0° set by the bias field alignment from the field-nulling procedure.	81
4.10	Energy level diagram highlighting (in green) the couplings for a $\Delta m_F = +1$ (top) and a $\Delta m_F = -1$ (bottom) Λ transition. The frequency degenerate (unwanted) transition is highlighted in thick, dashed red.	82
4.11	A simulation of the populations when the Λ transition is driven without the polarization selectivity. (a) shows the measure of all the populations, the $F = 1$ and the $F = 2$ states, as fractions of the total number of atoms. (b) shows only the number of atoms in the $F = 2$ states.	84
4.12	A simulation of the polarization-selective Λ transition. (a) shows the measure of all the populations, the $F = 1$ and the $F = 2$ states, as fractions of the total number of atoms. (b) shows only the number of atoms in the $F = 2$ states.	85
4.13	A simulation of the polarization-selective Λ transition, in the case of an elliptical polarization showing a small coupling to $ 2, 1\rangle$, an undesired level for the Λ transition. The undesired coupling is set for a selectivity of $1/7$. (a) shows the measure of all the populations, the $F = 1$ and the $F = 2$ states, as fractions of the total number of atoms. (b) shows only the number of atoms in the $F = 2$ states.	86
4.14	The Rabi rates related to the Λ transition. (a) The level structure, indicating which transition corresponds to which Rabi rate below. (i) One of the two Λ legs— the clock Rabi rate. This is a π transition. The measured Rabi frequency was 7923 ± 13 Hz (ii) One of the two Λ legs—the σ_+ , Δ_- transition. The measured Rabi frequency was 7824 ± 24 Hz. (iii) This transition would be degenerate to the Λ transitions. This transition is only weakly driven as seen by the very slow Rabi rate. This is a consequence of the circular polarization of the microwave field, allowing a successful Λ transition. The measured Rabi frequency was 316 ± 13 Hz. (iv) Another selected σ_+ transition (Δ_+). This transition can be measured to determine the Rabi rate for (ii), using a ratio of the transition matrix elements. The measured Rabi frequency was 13736 ± 38 Hz.	90
4.15	A Λ transition using the circular polarized microwave field to select only the desired level couplings. (a) shows the measure of all the populations, the $F = 1$ and the $F = 2$ states, as fractions of the total number of atoms. (b) shows only the number of atoms in the $F = 2$ states.	92

4.16	An attempted Λ transition without the selectivity of the circularly polarized microwave field. (a) shows the measure of all the populations, the $F = 1$ and the $F = 2$ states, as fractions of the total number of atoms. (b) shows only the number of atoms in the $F = 2$ states.	94
4.17	A two-level Δ_+ transition measured to show the fidelity and level of noise in such a measurement; to compare with the optimized Λ transition (Figure 4.18). (a) shows the full Rabi cycle (b) shows a finer scan around the π -pulse time of maximum transfer to the $ 2, +1\rangle$ state. There was a transfer of 99.5% of the population to this state. (c) shows the 2π -pulse time when population returned to the $ 1, 0\rangle$ state, where 99.1% of the population returns to this state.	95
4.18	An optimized Λ transition using the circularly polarized field. This transition is a measure of the fidelity of the all-microwave Λ transformation. Here, the angle of the bias field, and the powers and frequencies of the microwave fields were scanned around the expected values. The result was a Λ transition with 99.5% fidelity. (a) shows the full Λ transition Rabi cycle. (b) shows a finer scan around the time of maximum transfer to the $ 1, -1\rangle$ state. There was a transfer of 99.5% of the population to this state. (c) shows the population revival in the $ 2, 0\rangle$ state, where 98.8% of the population returns to this state.	97
4.19	This is a simulation showcasing the selection of a single transition via polarization selectivity, with level spacings defined by the Zeeman splitting at 15 mG. These are simulated microwave spectra using parameters to match the experiment. (a) shows the polarization-selective case. (b) shows the non-selective case.	99
4.20	Microwave spectra taken at a low 15 mG bias field. (a) A microwave spectrum is measured with polarization selection. The microwave drives only the $ 1, 0\rangle \rightarrow 2, +1\rangle$ transition. (b) A spectrum is measured without the polarization selection. Several states are populated.	101
4.21	Microwave Rabi taken at a low 15 mG bias field showing the difference between the polarization selected and non-selected transitions. (a) Rabi rate in polarization selective case. (b) Rabi rate in non-selective case.	102
5.1	The tripod transition, called so because of the shape of the three level couplings. The quantities Ω_1 , Ω_2 , and Ω_3 are the single-photon Rabi rates. A detuning in frequency, δ , is shared by all the driving fields.	105

5.2	The tripod transition, three-level coupling to a mediating state. The Rabi rate of each coupling is denoted as Ω_i for $i = 1, 2, 3$. The detuning of each driving field is δ	107
5.3	The tripod evolution of the initial state $ 1, 0\rangle$ under the Hamiltonian 5.1 with the bright state $ B_{rf}\rangle$, Eqn. 5.9. The legend on the right indicates the states corresponding the different plotted lines. Here, $\Omega = 15$ kHz and the detuning was zero ($\delta = 0$ Hz). For this bright state and detunings, the revival time $t_n = n \cdot 209 \mu\text{s}$. Note: the $ 1, 1\rangle$ and $ 1, -1\rangle$ states coincide exactly.	111
5.4	The tripod in the eight-level hyperfine structure. The tripod transformation couplings are highlighted in green. The undesired degenerate coupling is highlighted in dashed red.	114
5.5	The light shift used to detune the undesirable Δ transitions and lift the degeneracy around the tripod transitions. Here, Δ_{LS} represents the light-shifted energy level. The green arrows show the tripod couplings. The solid red arrows show the degenerate Δ transitions. The red dashed arrows illustrate the applied light shift from the D1 laser light.	115
5.6	Microwave spectra showing the effect of the 200 MHz detuned light shift. Energy level diagrams (on left) indicate the transition with the corresponding spectrum measured (on right). The red vertical arrows indicate the presence of the light shift. (a) The $ 1, 0\rangle \rightarrow 2, +1\rangle$ resonance with no light shift applied is measured at 70.6 kHz. (b) The $ 1, +1\rangle \rightarrow 2, 0\rangle$ resonance is measured at 83.8 kHz with an initial rf $\pi/2$ -pulse and the light shift applied. (c) The $ 1, 0\rangle \rightarrow 2, +1\rangle$ resonance is measured at 94.4 kHz with the light shift applied. (d) The $ 1, 0\rangle \rightarrow 2, 0\rangle$ resonance is measured at 11.1 kHz with the light shift applied. The differential light shift is approximately between the values $(94.4 \text{ kHz} - 70.6 \text{ kHz}) - 11.1 \text{ kHz} = 12.7 \text{ kHz}$, and $94.4 \text{ kHz} - 83.8 \text{ kHz} = 10.6 \text{ kHz}$, calculated from the measured light shifts presented here	122
5.7	Schematic setup for multi-tone microwave signal generation. The multi-tone signal is produced by the AWG (Sigilent SDG 2042X). The microwave signal is produced by an SRS SG384 signal generator, with the output switched and frequency doubled before the mixer. The upconverting mixer (Minicircuits ZMX-8GLX) receives the rf multi-tone signal on the IF input and the microwave-frequency input on the LO input. The output (RF) is amplified by the Alga Microwave amplifier (model ALPA 647240-50-01).	124
5.8	The level structure indicating which transitions were driven in the multi-tone Λ shown in Figure 5.9.	125

5.9	A two-tone Rabi cycle. Two microwave tones are applied through the multi-tone setup. (a) Shows the measurement with the the atoms in both $F = 1$ and $F = 2$. (b) Shows the measurement with only the populations in $F = 2$. (c) Shows the calculated atoms in $F = 1$, computed as the difference between the populations in (a) and (b).	126
5.10	A simulation of the two-tone Rabi cycle, using Rabi rates as measured in the experiment. The populations show qualitative similarities with Figure 5.9. The Λ transition, highlighted green in Figure 5.9, suffers from the degeneracy of another transition, shown highlighted dashed red in Figure 5.9.	127
B.1	A time line showing the multiple steps involved in the temporal dark MOT sequence	134
C.1	IGBT circuit, including Stern-Gerlach gradient coils as the inductive load.	135
C.2	An oscilloscope trace of a measurement of the current in the Stern-Gerlach coils switched off with the IGBT circuit. The current, measured with a current probe, is the blue trace (CH2) with 1 mV corresponding to 1 mA.	136
C.3	60Hz line trigger circuit.	137
C.4	The approximate waveform at several points in the 60Hz line trigger circuit. The letters correspond to probe locations lettered similarly in Figure C.3.	138
C.5	Connections for the unity-gain buffer circuit.	139
C.6	The slave current modulation amplifier circuit.	140
D.1	A schematic of a fluorescence imaging setup used for an example calculation of the expected number of reported camera counts per atom. The atoms are represented schematically as the red dot on the left side. The lenses are shown schematically in yellow (black outline). Here, an example setup with a 50 mm (1" diameter) re-imaging lens and a 780 nm line filter in place. The current version of the apparatus typically uses a 100 mm (2" diameter) re-imaging lens and no line filter.	142

SUMMARY

The manipulation of quantum spin states in a spinor Bose-Einstein condensate is critical for nearly all types of studies in these systems. State control methods are used to initialize the state of the system, apply Hamiltonian terms to modify the dynamics, and to measure properties of the quantum states. This thesis details the implementation of circularly polarized microwaves to selectively drive hyperfine transitions in the context of a spin-1 Bose-Einstein condensate of rubidium. This provides a new powerful tool for addressing specific transitions in the presence of frequency-degenerate transitions, allowing for new possibilities in state control. With this tool, we demonstrate a factor of $1/45.3$ reduction in the coupling strength between polarization selected and blocked transitions by the application of a circularly polarized microwave field. This newly-developed tool is used to explore a couple of important applications.

First, this polarized field is used to couple only three levels, out of all eight levels in the $F = 1, 2$ hyperfine structure of ground-state rubidium-87, to drive an otherwise degenerate Λ system with a 99.5% fidelity in state transfer from one base state of the Λ to the other. This Λ transition has applications such as in implementing a non-adiabatic holonomic gate within the spin-1 states and could be extended to give full $SU(2)$ control over two of the spin-1 states.

Second, the circularly polarized field is applied to selectively drive hyperfine transitions in low bias fields, where the Zeeman splitting between the spin-1 states is small and comparable to the spectral linewidth of the driving field. In such low fields, microwave transitions without polarization selection scramble the state, as there are couplings between multiple levels within the hyperfine structure. This thesis demonstrates the selection of transitions using polarization control of the microwave field to solve this problem. These measurements imply the utility of circular polarization selected transitions for more rapid manipulations than otherwise possible.

CHAPTER 1

INTRODUCTION AND BACKGROUND

In this thesis, we develop methods to selectively drive circularly polarized transitions in rubidium-87 Bose-Einstein condensates. This provides a new method to allow for better state control of spinor condensates, which has potential applications in new measurement techniques. This chapter will begin by introducing spinor condensate research and quantum state control, to provide context. Then the contributions of this thesis will be described.

Welcome to Spinor Physics

The 2001 Nobel prize in physics was awarded to three scientists—Eric Cornell, Wolfgang Ketterle and Carl Wieman for achieving Bose-Einstein condensation in dilute atomic vapors, a new state of matter with remarkable properties. The first Bose-Einstein condensate (BEC) was achieved in 1995 [1, 2], made possible through the development of laser cooling and trapping methods for atoms, work that earned Steven Chu, Claude Cohen-Tannoudji and William Phillips the 1997 Nobel prize in physics [3, 4, 5]. Bose-Einstein condensate is a quantum state of matter in which identical bosonic particles condense into the lowest quantum energy state at extremely low temperatures. The BEC quickly became a new testing ground for quantum physics. Early experiments demonstrated the matter wave properties of BECs such as coherence and interference in the condensate, much like light waves [6, 7]. Taking the analogy with light waves further, several groups quickly demonstrated atom lasers by leaking a coherent matter wave out of the BEC [8, 9, 10]. For these earliest results, the BEC was magnetically trapped in a single spin state, preventing spin dynamics between the magnetic sublevels of the BEC atoms. Before too long, multi-component BECs were demonstrated with populations in multiple hyperfine states [11, 12]. Then in 1997, the Ketterle group transferred the BEC from the magnetic trap to an optical trap, al-

lowing for the confinement of multiple hyperfine states of the atoms [13]. This was the start of the studies in spinor BECs, which feature dynamics associated with a spin degree of freedom. Not too long after this first spinor BEC, our group demonstrated the formation of a spinor BEC directly in an optical trap [14]. These early spinor BECs were used to study the formation of domains of the spin components, their miscibility, and spin textures [15, 16]. Soon, these spinor condensates became a workhorse for studying many quantum mechanical phenomena [17, 18].

In our lab, following the all-optical formation of the spinor BEC, studies were conducted on spin mixing driven by the quantum fluctuations at low fields [19], which led shortly thereafter to studies of coherent spin mixing [20, 21]. This showed coherent oscillations within populations of the spin components in the ^{87}Rb spinor BEC which were well described by a mean field theory. Following this work, sub-poissonian number squeezing was measured [22]. This number squeezing is a result of the spin-mixing collisions in the spin-1 BEC which produces exactly correlated numbers of atoms in opposite spin states via atomic four-wave mixing. Not long after, our group made measurements of spin-nematic squeezing [23]. This squeezing in the spin and nematic variables of the system was demonstrated following a rapid quench of the magnetic field. Measurements of this squeezing required state control methods to rotate the squeezed quadrature into the measurement basis and to perform a tomography to measure the squeezing. The result of this spin-nematic squeezing was a factor of -8.3 dB reduction in the variance compared to the standard quantum limit (SQL), where the SQL is the limit in variance for uncorrelated particles.

Elsewhere in the field, there have been a great number of further studies in squeezed states [24], with a current maximum squeezing of -20.1 ± 0.3 dB in an atomic system [25]. Squeezed states in atoms have been put to use for metrologic improvement in clocks [26] and magnetometers [27, 28]. Additionally, there has been a push to make use of quantum correlations outside of squeezed states to improve measurements, as these states represent

only a small subclass of entangled states accessible in cold atom experiments. In another result from our lab, non-gaussian fluctuations in the spin-1 BEC were measured following a magnetic field quench [29]. Several other non-gaussian states have been prepared including Dicke states [30, 31, 32, 33], Twin-Fock states [34], and NOON states [35].

Entanglement is a necessary ingredient in quantum computing, quantum simulation and quantum metrology. In ion and photonic systems, there has been entanglement demonstrated between as many as 20 ions [36] and 20 photons [37], but entanglement must be considered differently in the many body systems of neutral atoms where entanglement has been measured between thousands of atoms [38, 39]. Despite the high levels of entanglement accessible to these many body atomic systems, there is no clear cut way to measure the entanglement. This problem is additionally complicated in the case of a spinor BEC, where the particles are indistinguishable bosons and collective measurements are made on the state. In this case, a common method is to define a squeezing parameter, which quantifies the enhancement in the variance of an observable for the squeezed state compared to that of a classical state. From this squeezing parameter, a minimum level of entanglement can be inferred [40, 41, 42, 43, 44]. In a similar vein, the Fisher information provides a measure of the limit of precision in estimation of a phase for a given state, thereby quantifying the metrologic precision of this state. And like the squeezing parameter, the Fisher information gives a bound on the entanglement of the state [45]. These types of parameters are valuable for squeezed states, where an effect of the entanglement is a quadrature with decreased noise. However, these measures do not provide a tight bound on the entanglement.

Beyond these inferred measures of entanglement, there are more direct quantifications of entanglement if the correlations between different modes (e.g. different spatial modes) can be measured [46]. Recently, several such measurements were made in ultracold atom systems [47, 48, 39]. In these studies, the Einstein-Podolsky-Rosen (EPR) paradox ([49, 50]) was violated through strong correlations between the separate modes.

Current experiments such as these are limited by the small number of observable quantities accessible to measurement. In many cases, one of the primary difficulties in these such experiments is designing a suitable measurement scheme to capture properties of the quantum state. However, if normally inaccessible observables in these systems could be mapped into a conveniently measurable basis, these limitations could be overcome. This inaccessible observable mapped to a measurable quantity can provide a positive operator valued measure (POVM) for the expectation value of the desired observable [51]. Such a solution would be possible through quantum state control. This state control is the ability to effect a designed transformation on the state of the system, without introducing excess noise and while preserving coherence in the system [52]. In the spin-1 BEC specifically, this control would provide many valuable capabilities. For example, multiple POVMs of a single BEC could be made by mapping quantities to the unpopulated ($F = 2$) hyperfine level for measurement. This creates the possibility of measuring the full state vector for each BEC preparation [53]. This measurement capability would allow properties of the state to be measured directly without the need for complicated state tomography schemes [54]. Such quantum state control could additionally open the door for new ways to use entanglement as a resource. One such example in the spin-1 BEC is a unitary transformation which maps the spin-nematic squeezed state to a metrologically-valuable Larmor-squeezed state, with a squeezing enhanced magnetic field sensitivity. Clearly, *quantum state control* would provide maximal flexibility in manipulation and measurement in these quantum systems.

1.1 Quantum State Control

Quantum state control of atomic hyperfine states has been an important and actively investigated field that dates back all the way to the pioneering work by Rabi [55]. Such control at the simplest level is at the heart of atomic clocks and magnetic resonance. More complicated systems involving multiple levels have also been investigated, stimulated in large

part by quantum information.

The simplest case of quantum state control is realized in a two-level, or spin-1/2 system, where an external oscillating field can directly couple two states. This is the two-level Rabi problem, a standard quantum mechanics textbook problem (e.g. [56]), where an oscillating external field interacts with the spin of the system and drives population oscillations, or “Rabi flopping” between the two states at a characteristic Rabi frequency (or Rabi rate). The coupling field phase, amplitude, and detuning from the two-level energy spacing provide enough control to realize arbitrary SU(2) transformations on the state. However, this simple two-level problem often cannot be realized in experiments. In many cases, the splitting between the two levels is at an unfavorable frequency for application of the coupling fields; or, as is the case in the ^{87}Rb spin-1 BEC, there may exist degenerate transitions preventing a simple, closed, two-level coupling. In other cases, control based on other transitions can provide advantages. For instance, optical transitions are commonly chosen when specific sites need to be spatially addressed in an experiment (e.g. in a linear chain of ions or in a lattice), since the driving field can be provided by a laser focused onto a specific site.

In such scenarios, a common approach is to take advantage of a third *mediating* level. Then a transformation is performed on the two desired levels (let’s call these the “computational basis” states, $|1\rangle$ and $|2\rangle$) by coupling both of these levels to this third mediating state (let’s call it $|e\rangle$) with two oscillating fields. Here, an arbitrary SU(2) transformation can be performed on the two-level subspace $\{|1\rangle, |2\rangle\}$ if there is sufficient control over the two coupling fields, i.e., their amplitudes, relative phases, and frequencies [57]. But there is an added complication in for this three-level approach—spontaneous emission from the mediating state introduces a new decoherence mechanism [58].

One solution to this problem is the detuned stimulated Raman transition, whereby the two oscillating field frequencies are detuned from the transitions to the mediating state by the same amount, satisfying a two-photon resonance [59, 60, 61]. With sufficient detuning

from these single-photon transitions, this stimulated Raman transition produces population oscillations between the computational basis states with low excitation to the excited state, minimizing the effect of decoherence due to spontaneous decay from this level. A schematic of the energy levels and couplings for this type of transition can be seen in Figure 1.1. This stimulated Raman transition drives oscillations at a (two-photon) Rabi frequency of $\Omega_{2\gamma} \propto \frac{\Omega_1\Omega_2}{\delta}$. Here Ω_1 and Ω_2 are the single-photon Rabi frequencies and δ is the shared detuning from the resonant frequency as indicated in Figure 1.1. Since this two-photon Rabi frequency is inversely proportional to the detuning, large field amplitudes (large Ω_1 and Ω_2) are needed for fast stimulated Raman transitions at large detunings.

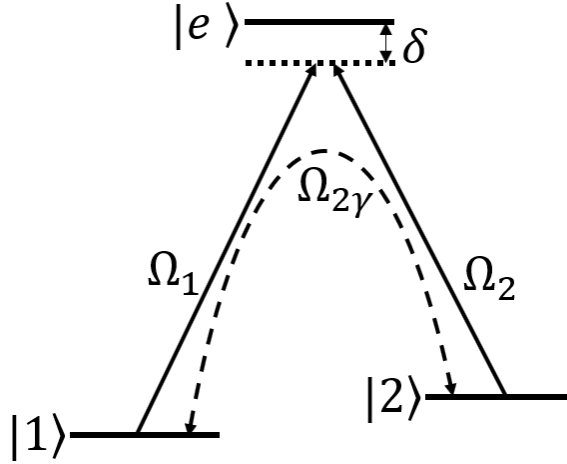


Figure 1.1: The stimulated Raman transition showing the Λ -type level structure. The single-photon coupling strengths for this transition are Ω_1 and Ω_2 , with a resulting two-photon Rabi rate indicated as $\Omega_{2\gamma}$. This shows the case of two-photon resonance, where both coupling fields are detuned from the excited state transition by the same amount δ .

These stimulated Raman transitions have become a staple tool in quantum information and are widely used to implement single-qubit gates for manipulations of trapped ion systems [62, 63], atoms in optical lattices [64], and quantum dots [65].

Another solution to the problem of decoherence from spontaneous decay was introduced in 1990: stimulated rapid adiabatic passage (STIRAP) [66]. STIRAP is based on trapping the state of the system in a *dark state* of the field-interaction Hamiltonian, an

eigenstate of the Hamiltonian which is not excited by the coupling fields. By slowly tuning the coupling field parameters, the Hamiltonian is adiabatically varied, allowing the dark state to adiabatically follow. This way, the dark state can be swept adiabatically from the initial state (e.g. $|1\rangle$) to the final state (e.g. $|2\rangle$) as the state of the system follows without being excited to the mediating state ($|e\rangle$), thus preventing spontaneous emission. For STIRAP, the coupling fields are turned on in what might be a counter-intuitive order, where for an initial state $|1\rangle$, the field coupling the levels $|2\rangle \leftrightarrow |e\rangle$ is turned on first, followed by the field coupling the levels $|1\rangle \leftrightarrow |e\rangle$. This is illustrated in Figure 1.2. The primary limitation for the STIRAP process is the necessity of knowing the initial state, in order to start with the correct dark state.

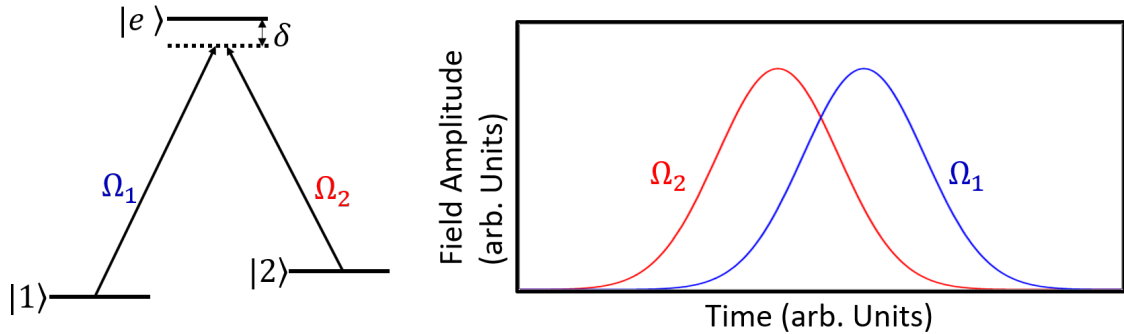


Figure 1.2: The STIRAP transition. (left) The Λ -type level structure. The single-photon coupling strengths for this transition are Ω_1 and Ω_2 . This shows the two-photon resonance case, where both coupling fields are detuned from the excited state transition by the same amount δ . (right) An illustrative schematic of time-dependent coupling strengths for a STIRAP transition from the initial state $|1\rangle$ to the final state $|2\rangle$, portraying the counter-intuitive ordering for the pulses.

These Λ -type transitions form the basis for a non-adiabatic holonomic gate ([67, 68]), which are necessary building blocks for the realization of non-adiabatic holonomic quan-

tum computing—quantum computing based on noise resilient geometric phases [69, 70]. Such non-adiabatic gates have been realized experimentally in superconducting transmon systems [71] and in nitrogen-vacancy centers in diamond [72, 73]. Beyond two-level control, these methods have been extended to systems with a three-state computational basis (the “tripod” configuration) [74, 75] and considered in a multi-state computational basis [57].

Additionally, other methods of multi-state control have been applied in atomic systems. An important body of work on this subject comes from the groups of Poul Jessen and Ivan Deutsch, showing an implementation of arbitrary control within the 16-dimensional Hilbert space spanned by the $F = 3$ and $F = 4$ hyperfine levels (each having $(2F + 1)$ sublevels) in ground state ^{133}Cs . Here, state control is accomplished with the application of several fields: a static bias magnetic field, two phase-modulated radio-frequency (rf) fields orthogonal to the bias field, and a phase-modulated microwave field. Complex software-generated modulation functions are calculated for each of these fields to design unitary transformations for the hyperfine levels. This work can be seen in, for instance, refs. [76, 77]. Recently in an application of quantum state control, arbitrary state readout was studied by mapping the $F = 1$ hyperfine levels in a ^{87}Rb BEC (again with $(2F + 1)$ sublevels) onto the larger Hilbert space of all the $F = 1$ and $F = 2$ hyperfine levels [54]. This readout allowed for the measurement of spin-nematic squeezing without performing state tomography by directly measuring expectation values related to the spin and nematic observables S_x and Q_{yz} for the same prepared BEC, where S_x and Q_{yz} are collective spin-1 operators [78]. Each measured pair of these observables (S_x, Q_{yz}) provides a measure of the state distribution projected into the $S_x Q_{yz}$ -plane, with several such measurements reliably representing the state distribution. It is worth highlighting that these measurements are based on microwave manipulations between hyperfine levels. Conventionally with fewer accessible observables, the spin-nematic squeezing is measured by rotating a quadrature from the $S_x Q_{yz}$ -plane into the measurement basis and collecting statistics based on measurements

in the spin operator S_z for similarly prepared squeezed states to determine the expectation value of $\langle S_z^2 \rangle$ [23]. This measurement for several tomography angles corresponding to angles of the measured quadrature in the $S_x Q_{yz}$ -plane; then the state distribution can be reconstructed via a computed backprojection. Although in this case the squeezed quadrature of interest can be successfully measured with standard state manipulations, the potential utility of the arbitrary measurement can be seen—this particular arbitrary measurement is just one example of the power of additional state control in a quantum system.

1.2 State Control in Chapman Labs

Thus far, there are few manipulations available to control the quantum state in our spin-1 BEC. In the recent non-abelian geometric phase study, headed by my predecessor Dr. Bharath H. M., the application of some limited loops in the spin-1 system were studied. For these loops, we were able to perform sufficient rotations with carefully designed sequences of microwave and radio-frequency pulses [79]. Following this, we began a study on the geometry of the spin-1 state based on measurements of spin-fluctuation tensor [53]. During this study, it became quite clear that noise intrinsic to the state manipulations overwhelmed the measurements. This study was ended because of this excess noise, determined to be due to detuned couplings to undesired states. A more selective or sophisticated control scheme would allow for such measurements to be made. This is direct motivation for a circularly polarized microwave field which selectively drives desired transitions while blocking undesired transitions.

Thesis Contributions

The work in this thesis includes studies in the ^{87}Rb spin-1 BEC exploring topics of state control. The central experimental result is the demonstration of polarization selective microwave transitions using a circular polarized microwave source that we developed appropriate to this and similar cold atom experiments. This provides a new powerful tool for

addressing specific transitions in the presence of frequency-degenerate transitions, allowing for new possibilities in state control. A factor of $\approx 1/50$ reduction is demonstrated in the coupling strength between polarization selected and blocked transitions by the application of this circularly polarized microwave field.

The circularly polarized microwave is applied in a selective three-level Λ transition, which would otherwise suffer from degeneracies without the selection rule afforded to the circularly polarized microwaves. Using the circularly polarized microwave field, this Λ transition is demonstrated with a 99.5% fidelity in state transfer from one base state of the Λ to the other, comparable to two-level transition fidelities measured in our system.

In addition to the Λ transition, the circularly polarized field is applied to selectively drive hyperfine transitions in low magnetic fields, where the Zeeman splitting between the spin-1 states is small and comparable to the spectral linewidth of the driving field. In such low fields, microwave transitions without polarization selection scramble the state as there are couplings between multiple levels within the hyperfine structure. It is shown that the selection of transitions using polarization control of the microwave field solves this problem. These measurements imply the utility of circular polarization selected transitions for more rapid manipulations than otherwise possible, since the nearby transitions within the microwave linewidth can be blocked.

This thesis will conclude with short descriptions of a couple additional projects based on state control in the spin-1 BEC. A four-level “tripod” control scheme is presented as a means to achieve arbitrary $SU(3)$ control and measurement of the spin-1 state. An attempt to implement an all-microwave based tripod transition will be described.

CHAPTER 2

TECHNICAL AND APPARATUS DETAILS

The experiments in this thesis were performed in the newest version of the BEC apparatus. Our lab has had the Bose-Einstein condensate project running (through multiple versions) since the all-optical BEC formation in 2002. Since this time, the chamber and supporting systems have evolved as multiple generations of graduate students have worked on this project. This evolution of the apparatus can be seen through the experimental details in the group theses [80, 81, 78, 82, 83, 53]. The current version includes a newly built vacuum chamber for the BEC, as well as several other modifications and improvements to the supporting systems. The experiments described in this thesis and our group’s recent work on non-abelian geometric phases in the spin-1 BEC [79] mark the first results obtained within the current version of the BEC apparatus.

This chapter will begin by detailing the BEC apparatus, highlighting the changes made in the new version of the apparatus and describe the systems relevant to the understanding the workings of the experiments presented in this thesis. The second part of the chapter will detail the developments in microwave hardware which are a central to the body of work in this thesis. The discussion will include a description of testing methods for antennas, as well as descriptions of several microwave antenna designs.

2.1 The BEC Apparatus

2.1.1 Vacuum Chamber

The spinor BEC experiments are performed on ^{87}Rb within an ultra-high vacuum (UHV) chamber. The main section of this UHV chamber system, the “science chamber,” is a 6.0” Kimball physics spherical octagon (Figure 2.1). A magneto-optical trap (MOT) is

formed at the center of this chamber [84]. This MOT provides cold atoms which are loaded directly into an optical dipole trap at the focus of a 10.6 μm wavelength CO_2 laser. The BEC is formed directly by evaporative cooling in this optical trap by decreasing the trapping potential (by lowering the CO_2 laser power) and the trap waist to keep densities high enough for rethermalization [80, 81]. The trap is formed with a maximum of 60-100 W of laser power, which necessitates the use of specific viewports for high-power 10.6 μm light. The chamber is therefore fitted with two opposing zinc-selenide viewports with anti-reflection coatings for 10.6 μm light, which allow the CO_2 laser light to pass through the chamber. These windows are on the perimeter of the octagon. There are AR-coated pyrex glass viewports on five of the other ports around the perimeter of the octagon used for the MOT light and imaging. The last of the perimeter octagon ports is connected to the pumping section of the UHV chamber. Additionally, there are large AR-coated pyrex viewports on 6" flanges on the top and bottom of the science chamber. It is through these large viewports that the microwave field will be transmitted (to be discussed below). The pumping section consists of a 40 L/s Varian Starcell ion pump and a titanium sublimation pumping section, used to maintain UHV ($\approx 10^{-11}$ torr) in the chamber. Additionally, there is a Varian all-metal bellows valve for connecting this chamber to our "pumping station," a setup we use to pump the chamber down to high (or ultra-high) vacuum after assembly and during the bakeout process. This bakeout procedure is described in the appendix.

The octagon science chamber can be seen in Figure 2.1, both as a CAD model, and a photo of the inside of the chamber in its current state. Within the chamber, there are three lens mount assemblies machined from Macor ceramic to hold each of three lenses one focal length from the geometric center of the chamber. The lenses are fixed in place within the mounts with non-magnetic titanium hardware. These assemblies are held in place with groove grabbers specific to the Kimball physics chamber. The design of these lens mount assemblies is new to this version of the BEC experiment. The two opposing lenses, which are also on axis with the zinc-selenide viewports (this is the CO_2 laser axis), hold the

focusing lenses for the dipole trap and collimate the light before exiting the chamber. These lenses define the location of the trap within the chamber. The third lens assembly is at a right angle to the other two. This assembly holds a high numerical aperture aspheric lens—the “imaging lens”. This is the imaging lens, with its high numeric aperture of $NA = 0.51$ ($f = 26$ mm, Thorlabs AL3026-B lens) allows for the collection of a large fraction (up to 6.5%) of the full (4π) solid angle of light emitted in fluorescence of the atoms. The lens mounts can be seen inside the science chamber in Figure 2.1. Models of the lens mount assemblies themselves are shown in Figure 2.2.

The imaging lens assembly has two threaded holes on one of the top surfaces used to secure the ends of SAES-brand rubidium dispensers. These dispensers are the source of rubidium for the experiments. Running a current through these dispensers activates the release of rubidium via ohmic heating. Each dispenser is connected on one end to the chamber (grounded) and on the other end to an electric feed-through which supplies current. This allowed us to wire connections separately to both dispensers with a single two-connection electronic feed-through on the vacuum chamber. One of these dispensers is turned on during the MOT loading time (typically a 15 s period for each cycle of BEC formation) and then off during the evaporative cooling and BEC formation portion of the cycle to improve the vacuum lifetime during BEC experiments. The second dispenser is redundant, and in place for the eventual depletion of the first dispenser. Additionally, three blue light LEDs are used for light-induced atom desorption (LIAD) [85], positioned pointing towards the chamber center through the large top and bottom viewports. These blue lights are similarly switched on only for the MOT loading period. As the rubidium dispenser is depleted, the LIAD lights become more significant to the atom loading. The effectiveness increases as more rubidium is deposited within the chamber.

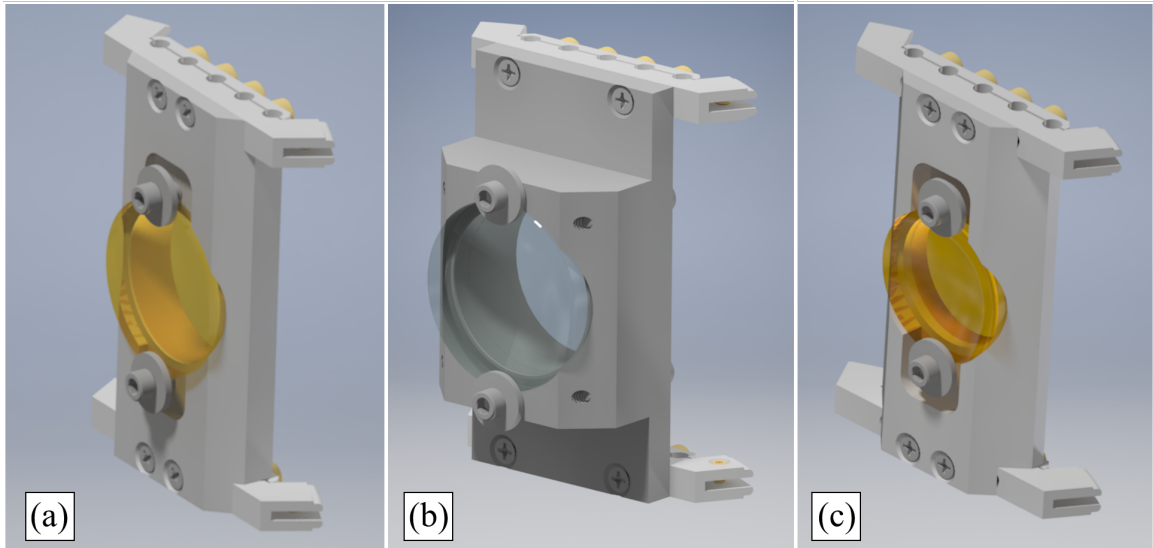


Figure 2.2: Several views of the CAD models for the lens mounts. (a) The CO₂ laser input lens assembly. The lens is a 27.94 mm diameter, 38.1 mm effective focal length zinc-selenide aspheric lens from II-VI Infrared, Inc., anti-reflection coated for 10.6 μm. (b) The imaging lens assembly. The lens is a Thorlabs AL3026-B. (c) The CO₂ laser output lens assembly. The lens is a Thorlabs LE7981-F, a zinc-selenide meniscus lens.

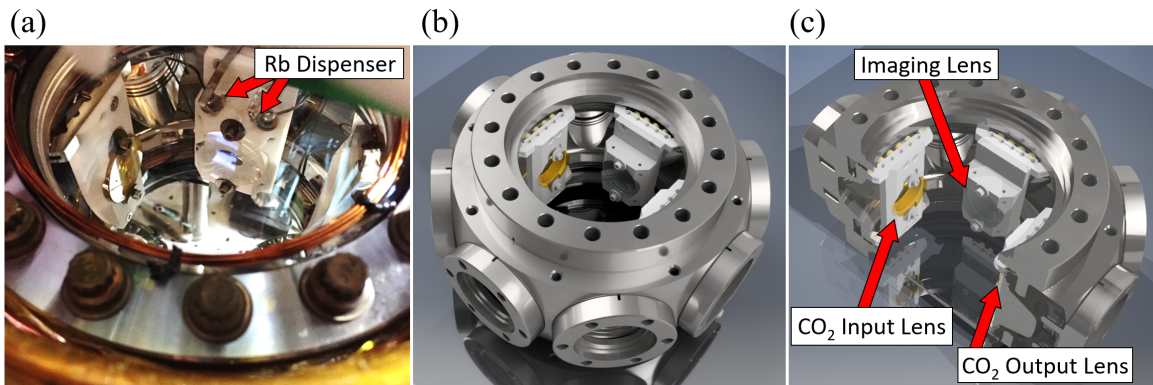


Figure 2.1: The science chamber—the Kimball physics spherical octagon chamber within which the BEC experiments are performed. (a) A photo of the inside of the chamber with all components in place. (b) A CAD model of the science chamber, pumping section not shown. (c) A cut-away view of the CAD model showing the internal lens mounts and hardware.

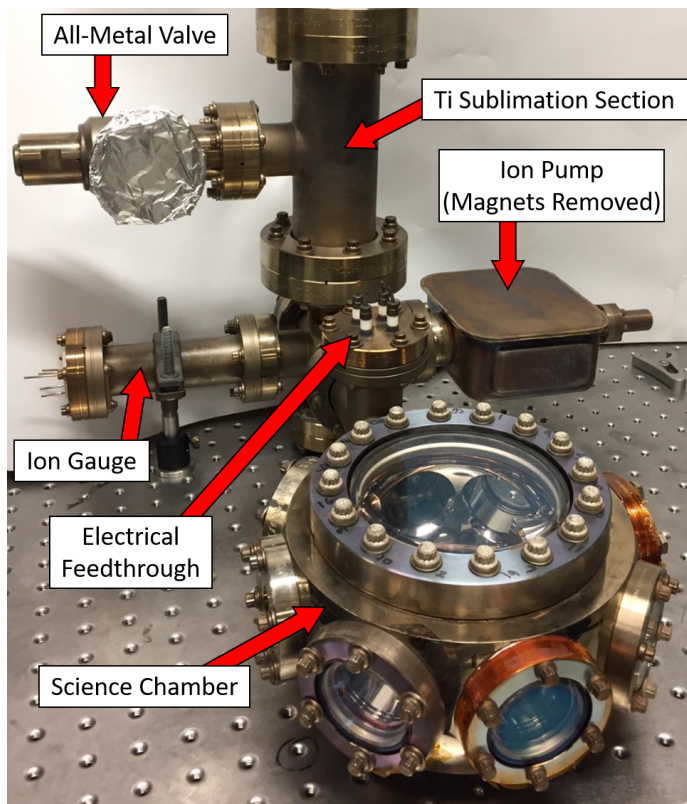


Figure 2.3: A view of the BEC apparatus vacuum chamber. The spherical octagon is in the foreground of the image with the pumping section connected off the back. This is a version Bharath H. M. and I built before building the current version of the apparatus. This shows the similar pumping setup and arrangement to science chamber compared to the current version. In quite a surprise turn of events, the Rb dispenser in this chamber was depleted, leading to low atom numbers in the experiment and consequently the newest version of the chamber.

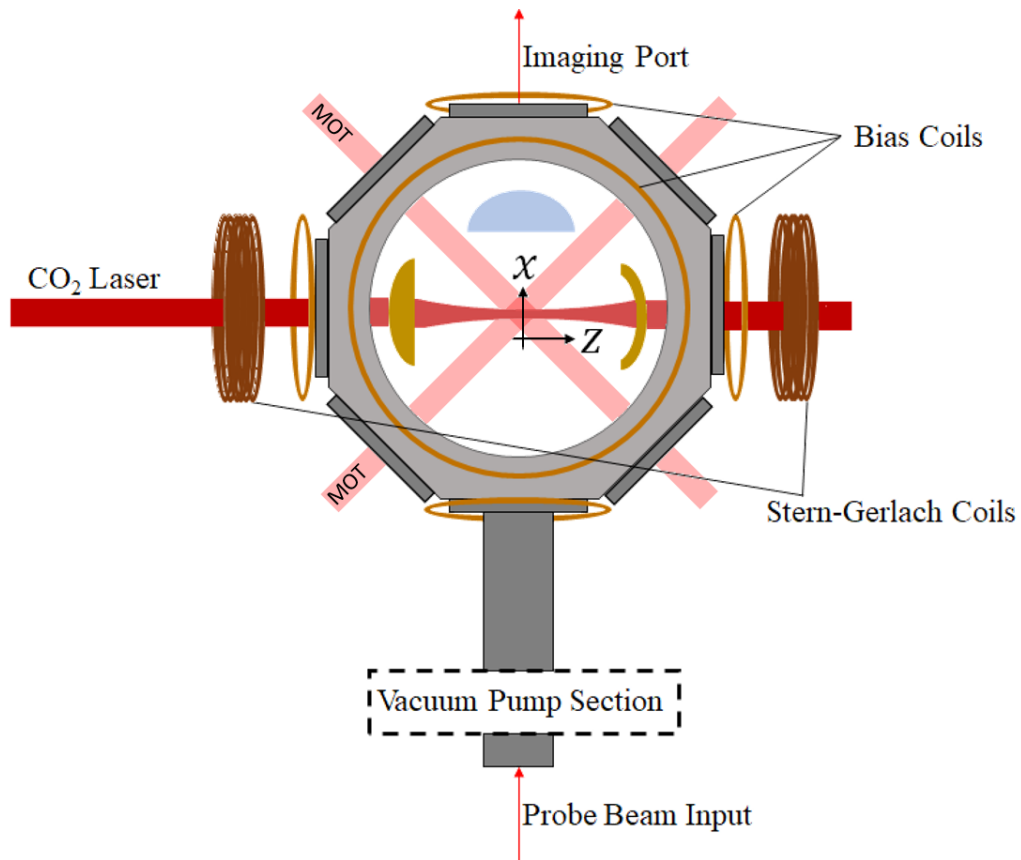


Figure 2.4: Schematic representation of the chamber. The x and z axes are denoted, the y axis is out from the page. One bias coil of each pair is indicated.

Table 2.1: Typical powers in each MOT beam. These are labeled by fiber designations as can be seen in Figure 2.5.

Fiber #	Cycling Power	Repump Power
MOT 1	35 mW	9 mW
MOT 2	35 mW	3 mW
MOT 3	35 mW	3 mW

Laser Systems

These experiments require sophisticated laser setups for cooling the atoms, imaging for measurement, and various other uses. The main cooling laser provides light for the MOT and for imaging the atoms. For the MOT, this “cycling” laser is slightly red detuned (6 MHz) from the $F = 2 \rightarrow F' = 3$ cycling transition of the D_2 line. The laser setup allows for an adjustable detuning of up to -200 MHz from the $F = 2 \rightarrow F' = 3$ cycling transition, with large detuning used during the temporal dark MOT step. The laser detuning is set to resonance (0 MHz detuning) for fluorescence imaging. A repump laser, resonant with the $F = 1 \rightarrow F' = 2$ transition, is also required to pump atoms that decay into the $F = 1$ state back into the cycling transition for the MOT. This repump laser is also used to pump atoms out of the $F = 1$ state for state measurement.

Compared to the previous version of the laser setup, repump light is now combined with all the MOT beams before this light is coupled into optical fibers for delivery to the experimental chamber. The laser systems up to this fiber coupling section have remained largely the same from the previous version of the experiment, except for periodic maintenance and repair [78, 82]. This new fiber coupling section of the laser setup is shown schematically in Figure 2.5. Each of the three optical fibers from this setup is used to illuminate one axis of the MOT. A new feature is a shutter in the MOT 1 beam path is used to block the vertical MOT beam. This shutter is used to reduce scatter when imaging the atoms with a camera on the vertical axis. Typical MOT beam powers are given in table 2.1.

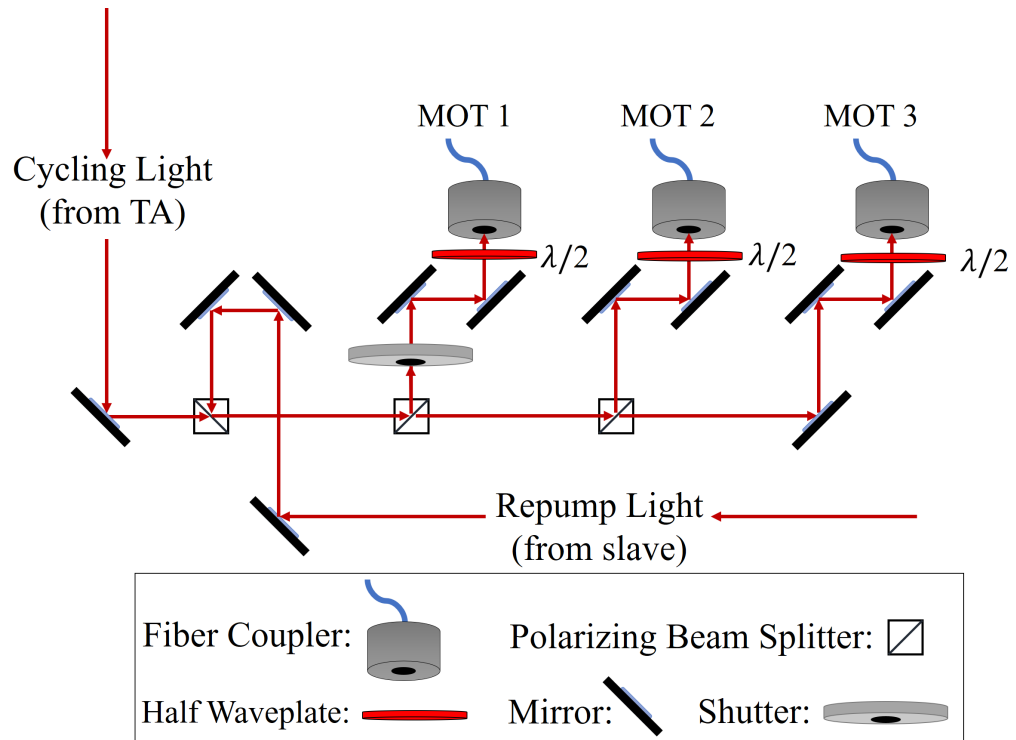


Figure 2.5: The modification to the optical fiber setup for the MOT lasers. Each fiber illuminates one axis for the MOT; these fibers are labeled as “MOT 1,” “MOT 2,” and “MOT 3.” The MOT 1 fiber is used for the vertical MOT beam. The MOT 2 and MOT 3 fibers are the two horizontal axes.

An additional laser system has been added to the BEC apparatus with a wavelength near the D1 line of ^{87}Rb , approximately 795 nm. This laser is locked to the crossover peak between $F = 2 \rightarrow F' = 1, 2$, giving a lock point that is -408.3 MHz detuned from the $F = 2 \rightarrow F' = 2$ transition. For a larger detuning, the lock point can also be set to the $F = 2 \rightarrow F' = 2$ transition. A double-pass acousto-optic modulator (AOM) setup with adjustable frequency shifts this light closer to resonance. A typical configuration would be shifting the light by 2×229 MHz with the AOM, giving light at $+50$ MHz detuning from the $F = 2 \rightarrow F' = 2$ transition. There are two optical fiber couplers in this setup. One uses the undiffracted order from the AOM to monitor the wavelength of the laser on a wavemeter, which is used to monitor the laser but is not necessary for typical operation. The second optical fiber carries light to the chamber, replacing the absorptive probe when used. Switching the rf signal to the AOM allows this light to be turned on or off. This laser system is build for applying a light shifts to lift degeneracies in the hyperfine transitions. A detailed discussion of this light shift will be presented in Chapter 5.

gradient along the long trap axis, also aligned along the CO₂ laser axis

The chamber has three sets of trim coils along orthogonal axes. These coils are used to cancel the ambient magnetic field to as low as ≈ 1 mG and apply a controlled bias field during the experimental cycle while the BEC is held in the trap. These coils are additionally used in the spinor BEC experiments to set the quantum phase for the ground state (polar vs ferromagnetic phase). For the experiments described in this thesis, the alignment of the magnetic field is critical for the polarization based selection of transitions to work—this point will be described in detail below. The direction of the bias field is set by applying components of the bias field on each of the trim axes.

2.1.3 BEC Experiment Sequence

The formation of the BEC occurs in a several step sequence, totaling about 20 s for each BEC formation. The experiment starts with MOT loading for 15 s. Then for 310 ms following the MOT period, an empirically determined temporal dark-MOT compression sequence transfers the atoms to the CO₂ laser optical dipole trap in the $F = 1$ state. This involves several steps, including decreasing the magnetic field gradient, decreasing the repump laser power, and increasing the detuning of the cycling laser light. This sequence is detailed in the appendix.¹ At this point, the evaporation begins. A motorized translation stage moves the lens in a telescope in the CO₂ laser beam path, tightening the trap waist, increasing density for efficient rethermalization. At the same time, the power in the CO₂ laser trap is decreased from maximum power (≈ 60 W) to a final power of about 60 mW, lowering the trap potential.² The evaporation continues for 4.3 s (typically). During this time, the Stern-Gerlach gradient coils are turned on to an intermediate field strength, applying

¹The atom loading has been made somewhat more robust by adding repump light to all of the MOT beam fibers, compared to the previous setup which had a separate fiber to combine the repump light with only the vertical MOT beam. Additionally, a unity gain buffer circuit (see appendix) was added to reduce the AOM driver to reduce power fluctuations due to ground loops at low control voltages. These changes have eliminated the need for a daily optimizing scan of the repump power during the temporal dark MOT.

²This CO₂ laser power ramp is determined by piece-wise decreasing the CO₂ laser power in several small ramps, each to half the final CO₂ laser power of the previous ramp, and finding the time for each small ramp which maximizes the measured phase space density.

an additional potential to the $m_F = \pm 1$ atoms. These atoms are preferentially lost in the evaporation, purifying the population into the $m_F = 0$ state. A large bias field (≈ 1 G) is applied during the purification so the spinor BEC is initialized into the high-field polar ground state. Once this evaporation ramp including purification and state initialization is complete, experiments are performed on the spin-1 BEC. Following these experiments, measurements are made to count the number of atoms in each m_F state.

2.1.4 Measurement via Imaging of the BEC

The typical measurement in our spinor BEC experiment is made by performing a Stern-Gerlach separation of the spin states, followed by either fluorescent or absorptive imaging. For this measurement, the atoms are released from the trap by switching off the CO₂ laser power at the chamber by switching off an AOM earlier in the CO₂ laser beam path. At the same time, the IGBT circuit (described in appendix) quickly switches on current to the Stern-Gerlach coils, to about 450 A in 1 ms. As the atoms fall in the Stern-Gerlach gradient, the cold atom cloud is pulled apart into clouds containing populations of different m_F . The gradient is calculated to be ≈ 12 gauss/cm, with this value calculated from a measured Stern-Gerlach separation of $550 \mu\text{m}$ with the gradient field on for 17 ms. Note that the two ground state hyperfine levels ($F = 1, 2$) have opposite signs of g-factor, g_F . Therefore, in the Stern-Gerlach separation, atoms in the $|F = 1, m_F = \pm 1\rangle$ and $|F = 2, m_F = \mp 1\rangle$ states are measured in the same location. The atoms are allowed to fall for 19 ms before imaging the separate clouds. At time-of-flight (TOF) longer than 19 ms, light is lost due to vignetting within the imaging system. Figure 2.7 shows multiple fluorescence images as a time-of-flight sequence of the atom cloud falling in gravity. In this figure, separation of the clouds due to the Stern-Gerlach gradient is apparent. We choose a long TOF (19 ms) for the state measurement to allow for longer Stern-Gerlach separation for a significant separation between the clouds. After this TOF, the populations in the separate clouds are measured by taking an image of the clouds on an Andor iKon CCD camera, and measurements of the

populations are made by binning and counting regions of interest (ROIs) containing each cloud separately.

The measurement image can be either absorptive or fluorescent. Absorptive imaging used to examine spatial features of the BEC, since there is less distortion of the clouds due to radiation pressure in absorptive imaging compared to fluorescence imaging. This is useful to view spatial features such as spin domains and the spatial distribution during TOF (to verify Bose-Einstein condensation). However, fluorescence imaging has been better optimized in the current setup and performs with lower measurement noise. Additionally, after solving the rf calibration issues (described below), the imaging setup was no longer ideal for absorptive imaging. Therefore, fluorescence imaging was used for the measurements presented in this thesis. In fluorescence imaging, the lasers used for the MOT (shifted to be on resonance) are pulsed on for an exposure time (e.g. $200 \mu\text{s}$). The atoms undergo resonant fluorescence and the emitted light is collected with the imaging lens and re-imaged onto the CCD camera sensor.

A background ROI is also counted using a region of the camera sensor containing no atoms. The background ROI counts are used to calculate a mean number of background counts per pixel. This value times the number of pixels in each ROI is used for background correction. The background-corrected counts for each bin is converted to a number of atoms using a geometric calculation for the expected efficiency of light collection from the atoms (see appendix for calculation).

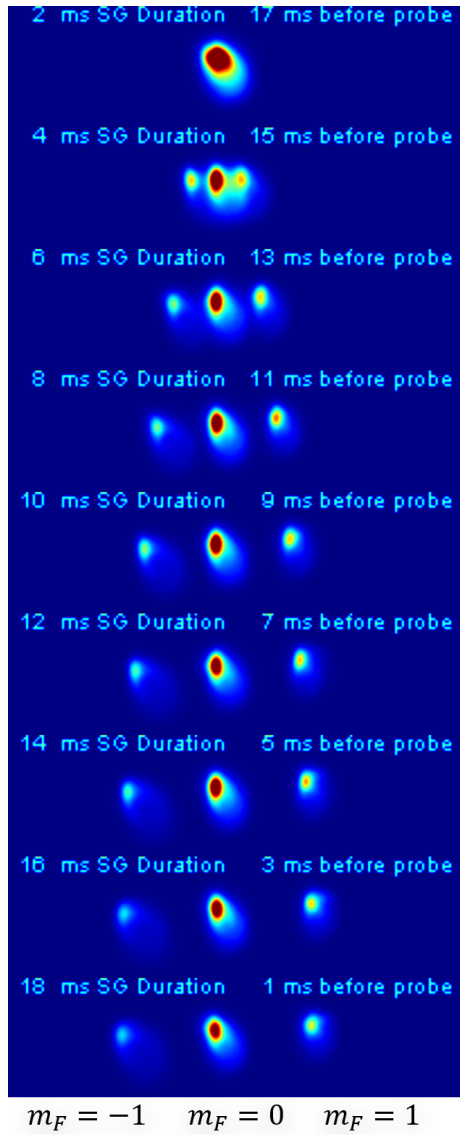


Figure 2.7: Several fluorescence images stitched together vertically to show the time-of-flight expansion within the Stern-Gerlach field. The images were taken at incremental times following the release of the atoms from the trap and are shown in false-color to enhance the visibility of contrast. The text above each frame states how long the Stern-Gerlach coils have been switched on (left, “ms SG Duration”) and how long before the probe time each frame was taken (right, “ms before probe”). In each frame, the $m_F = -1$, $m_F = 0$, and $m_F = +1$ components of $F = 1$ are on the left, center, and right of the image, respectively. The center of adjacent populations are separated by $\approx 550 \mu\text{m}$ at 19 ms.

Labeling Convention for the Measured States

There is an ambiguity to address for the Stern-Gerlach separation into m_F components. With this measurement method there is an option to measure only atoms in the $F = 2$ states or to measure simultaneously the populations in both $F = 1$ and $F = 2$. With the repump light on during imaging, atoms in both $F = 1$ and $F = 2$ are measured, and without this repump light, only the atoms in $F = 2$ are measured. As will be seen in more detail below, these $F = 1, 2$ states have g -factors of opposite-sign but very similar amplitude. As a result, the directions of Stern-Gerlach separation of m_F states is reversed between the $F = 1$ and $F = 2$ levels and populations of opposite sign of m_F coincide. Therefore, this thesis adopts the following labeling convention. For the three population ROIs from the measurements, the ROI containing the population from the $|1, -1\rangle$ state and also potentially the $|2, +1\rangle$ state is labeled “A,” i.e. the number of atoms counted is “ N_A ” and the fractional population calculated for this ROI is “ ρ_A .” Similarly the $|1, +1\rangle$ and $|2, -1\rangle$ ROI is labeled by “B.” All of the $m_F = 0$ atoms are in the center ROI, labeled by “0.” The populations in $F = 1$ can be determined from the subtraction of populations from the two cases; however, the result typically noisy, as it is susceptible to atom number fluctuations in the experiment.

RF Calibration Issues

The number of atoms measured in the spinor BEC project is calibrated through an rf calibration procedure [86, 78]. With the typical “ $4f$ ” imaging setup (see Figure 2.8), excess noise was measured in the rf calibration. After a great deal of troubleshooting, this rf calibration issue was resolved by moving the re-imaging lens as close as possible to the imaging lens viewport of the vacuum chamber. Following this realignment, the atom cloud images appeared sharper and the rf calibration measured results consistent with the geometric calculation for counts-per-atom (geometric calculation described in appendix). It is likely that the imaging lens is misaligned slightly too close to the atomic cloud within the

chamber. In this case, the light is divergent after the imaging lens and can be lost due to vignetting, or imaged diffusely on the camera sensor. Note, the imaging lens is mounted inside the chamber and therefore in a fixed position, as are the CO₂ laser trap optics which define the location of the trap relative to the imaging lens. Additionally, a significant coma aberration is expected for off-axis imaging with the aspheric lens.

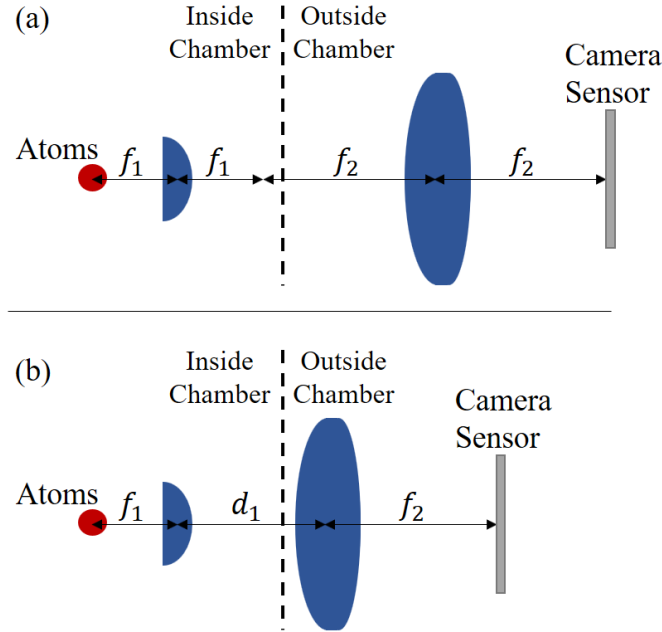


Figure 2.8: (a) A schematic of the $4f$ imaging setup. Two lenses are used to image light from the atoms onto the camera sensor. The first lens, the “imaging lens” is inside the chamber, one focal length ($f_1 = 26$ mm) away from the atomic cloud (red dot). This lens images the atoms at $+\infty$. The second “re-imaging lens” with focal length $f_2 = 100$ mm images the atoms onto the camera sensor. The total length of the optical path (on the principal axis) is the sum of two times each focal length ($2f_1 + 2f_2$), a total of four focal lengths. (b) A schematic of the modified imaging setup. Compared to (a), the separation between the two lenses is reduced (d_1).

2.2 Microwave Antenna Design and Setup

For the experimental investigations that will be presented in the following chapters of this thesis, a primary goal was the successful implementation of the circularly polarized mi-

microwave field, to provide the selectivity desired in hyperfine transitions, with extensions and applications of this. Of central importance to this study is a source of highly circular polarized microwaves (low axial ratio—defined below). For the cold atom experiments, this requirement is met by a careful choice of antenna to transmit the microwave field into the vacuum chamber. We therefore evaluated multiple antennas and developed some antenna testing methodologies.

This section will begin with a description of some of these antenna testing methods. Then there will be descriptions of some antenna types which were considered and evaluated using the described testing methods. This is by no means an exhaustive overview of antenna types, only a small sampling of some relevant or interesting designs, of both linear and circular polarization. Following the overview of antennas, the microwave device setups used in the experiment will be described.

2.2.1 Antenna Testing

This section will describe the testing methods used to evaluate antennas. Testing the individual antennas was a large part of the antenna build process. And although the cold atom apparatus provides an exceptional measure of the properties of the microwave field, it was desirable to test antennas using standard rf equipment first. This is simply because these benchtop measurements were easier to make and significantly quicker to perform.

One of the most important figures of merit for the studies herein is the *axial ratio* for each antenna. The axial ratio is a measure of the ratio of field amplitudes for orthogonal components of the electric field, and is a measure of the ellipticity of the polarization. An axial ratio of 1 corresponds to perfect circular polarization, whereas linear polarization has an infinite axial ratio. This axial ratio is often stated as a decibel value—in decibel, 0 dB corresponds to perfect circular polarization. The axial ratio is given by the ratio of the semi-major and semi-minor axes of the polarization ellipse for the microwave field. If the field amplitude is measured for each of these axes, as in the linear analyzer test below, the

axial ratio, r , is calculated in terms of the minimum and maximum microwave electric field amplitudes E_{max} and E_{min} .

$$r = \frac{E_{max}}{E_{min}} \quad (2.1)$$

In decibel units, the axial ratio is given by

$$r_{[dB]} = 20 \text{Log}_{10} \left(\frac{E_{max}}{E_{min}} \right) \quad (2.2)$$

However, the typical field measurements are in power. Additionally, these powers are often measured in decibel units (e.g. in dBm). For a ratio of powers in decibels (dB), N , between the semi-major and semi-minor axes of the polarization ellipse, the ratio of field powers (P_{max} , P_{min}) is given by

$$P_{max}/P_{min} = 10^{N/20} \quad (2.3)$$

The ratio of field amplitudes is given by the square root of Eqn. 2.3, since the field amplitudes are proportional to the square root of the power. The axial ratio can thereby be determined for the ratio of powers in decibels, N , for the semi-major and semi-minor axes of the polarization ellipse via

$$r = \sqrt{10^{N/20}} \quad (2.4)$$

In decibel units, this axial ratio is given by

$$r_{[dB]} = 20 \text{Log}_{10} \left(\sqrt{10^{N/20}} \right) = 10 \text{Log}_{10} \left(10^{N/20} \right) = \frac{N}{2} \quad (2.5)$$

Linear Analyzer Test

One of the of the main antenna testing methods used was a measurement of the power received by a linearly polarized antenna versus the orientation angle of the antenna polarization. For this measurement, two antennas were set opposing each other. One antenna, the transmitter, was driven at 6.834 GHz by a signal generator (at a maximum power of

+15 dBm). A second analyzer antenna, the receiver, measured the power. This second antenna was mounted on a rotation stage, such that the angle of the linear polarization for this antenna could be rotated. The test was set up by aligning the antennas approximately the distance the antenna would be mounted from the atomic trap (10-20 cm) and the alignment was adjusted to maximize the received power. Then the test was performed by measuring the received power as a function of the angle of the receiver antenna, where the receiving antenna acted as a linear analyzer. The minimum and maximum received powers were measured. The transmitter was the device-under-testing and could be either a linearly or circularly polarized antenna. The linear analyzer test setup is shown in Figure 2.9. These tests were initially performed on the optical table, but later moved to a wood table to prevent field reflections from the metal table surface.

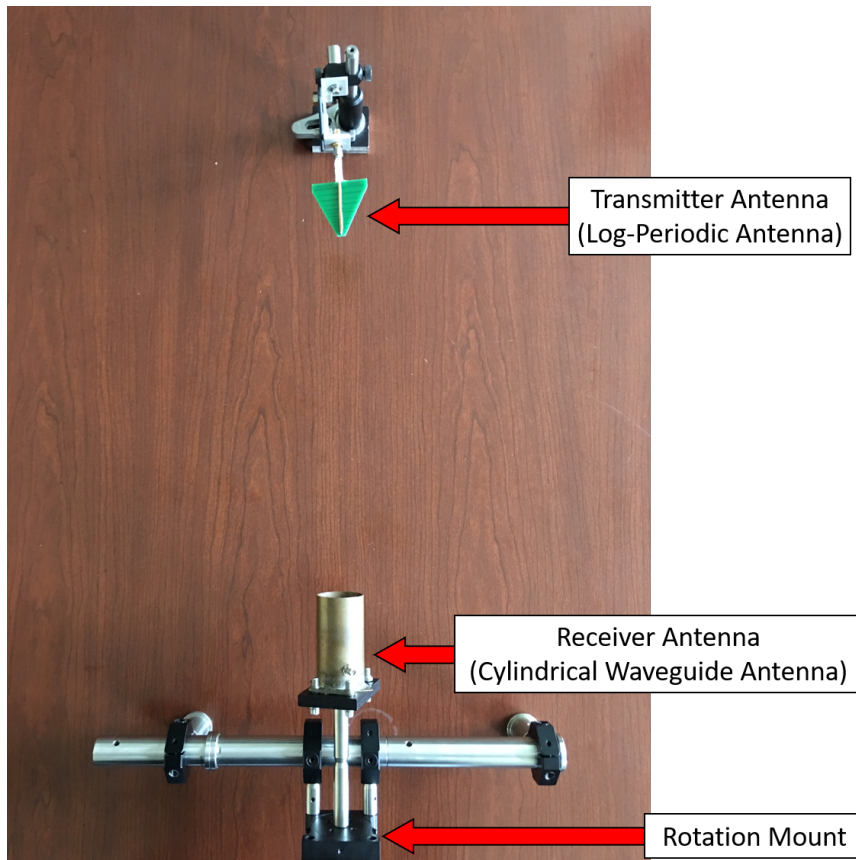


Figure 2.9: Setup used for crossed linear polarization testing, i.e. the “linear analyzer test.” The antenna on the bottom of the image (the circular waveguide antenna constructed from copper tube) is the receiver antenna, mounted on an angular rotation mount. The antenna at the top is a log-periodic antenna (green, triangular) and would be the transmitting antenna in this case. Cable connections to antennas not shown.

The receiver was a linearly polarized cylindrical waveguide antenna, with the received power measured using a spectrum analyzer (HP 8593E). In order to boost the signal level measured by the receiver, we used a couple small signal amplifiers (Minicircuits ZJL-7Z). The power received was measured as the relative angle of rotation between the antennas was varied (at fixed elevation and azimuth angles).

- For a linearly polarized antenna on the transmitting side, the rotation between the antennas simply measured a curve analogous to Malus’s law for crossed polarizers. The difference, measured in decibel (dB), between the maximum and minimum powers

gives a measure of the purity of linear polarization.

- For a circularly polarized antenna, the rotation of the linear analyzer should yield a flat power level for all rotation angles. There is in practice some fluctuation due to the inhomogeneity of the spatial mode of each antenna, as well as any ellipticity to the polarization. The ratio between the minimum and maximum powers measured can be used to calculate the axial ratio.

Helical Antennas as Receivers

An additional testing method involved using both a right- and left-handed helical antenna to compare the difference in power received between the two. Using this method, the maximum discrimination measured was approximately 15 dB between circular polarizations of different handedness. Linearly polarization was measured as the same power received in each handedness. This measurement is limited by the quality of the helical antennas used as analyzers. This provided a quick, but not very precise test for antennas. A simple improvement would be to use improved, low axial-ratio antennas.

2.2.2 Antenna Designs and Hardware

This section details some of the antenna designs considered for different purposes. One of the ideas for the circularly polarized microwave experiment was a hybrid antenna design, using two crossed, linearly polarized antennas with phase and amplitude adjustable signals. Therefore, a handful of linearly polarized antennas were tested. In the end, a single-element circularly polarized antenna was chosen for the experiment, allowing for a less-complicated microwave setup (only one microwave signal needed for this antenna).

Half-Wave Dipole Antenna

The half-wave dipole antenna is a very simple antenna design for a linearly polarized field and is seen to be used in many cold atom experiments. However, this antenna tested to have

a 9 dB power difference between crossed polarizations, which is quite modest polarization purity. One of these antennas is seen in Figure 2.10(a).

Cylindrical Waveguide Antenna

One of the standard linearly polarized antennas we use is a cylindrical waveguide antenna originally designed and built in our lab by Chris Hamley. This antenna consists of a copper tube with a copper cap on one end. A SMA connector with a straight antenna feed (just under a quarter wavelength) is installed a quarter wavelength from the grounded end of this antenna. This style of antenna was measured to have a 30 dB difference in received power between aligned and crossed polarizations, the largest crossed-polarization rejection out of the antennas tested. These antennas are thereby measured to be highly linearly polarized, and were therefore used as the receiver for the other antennas in the linear analyzer tests. Additionally, this antenna type was tested in the experiment to measure a high-contrast Malus's law dataset (see Figure 4.2).

Dual Cylindrical Waveguide Antenna

The dual cylindrical waveguide antenna is a design prototype for a hybrid antenna for circular polarization. This antenna uses two linearly polarized input feeds in the cylindrical waveguide orthogonal to each other and driven by 90° phase offset signals. Compared to the standard cylindrical waveguide antenna, the waveguide here has no endcap. The two input feeds are offset from each other along the length of the cylinder, as this was determined to perform better, potentially by reducing interference between the two feeds. The combination of the two fields can produce circularly polarized radiation. The tradeoff is the complication in the microwave setup, as this antenna needs two independent inputs. This antenna was measured to have 2-3 dB fluctuation in the linear analyzer test. One of these antennas is seen in Figure 2.10(b).

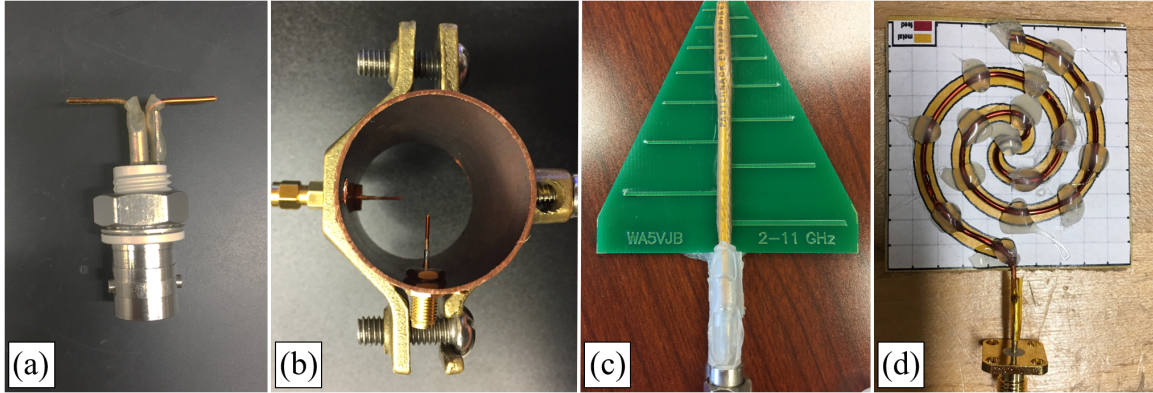


Figure 2.10: Photographs of several antenna types. (a) A BNC mounted half-wave dipole antenna for 6.834 GHz. (b) A dual cylindrical waveguide antenna (c) A WA5VJB log-periodic antenna (d) An Archimedean spiral antenna

Log-Periodic Antenna

The log-periodic (LP) antenna design is a preferred antenna design for high bandwidth applications. LP antennas are typically linearly polarized. We tested a couple WA5VJB log-periodic antennas (from Kent Electronics) to have mediocre polarization quality, with a 10 dB power difference between the aligned and crossed polarizations in the test setup, measured at 6.834 GHz and 10 cm antenna separation. The linear polarization tested better at 3.4 GHz, with a 22 dB crossed power difference. This could be related to the Fraunhofer distance ($d_F = 2D^2/\lambda$ where D is the antenna size and λ is the wavelength) defining the length scale of the near field (vs far field) for the radiation [87]. The Fraunhofer distance was shorter for the lower frequency test. One of these antennas is seen in Figure 2.10(c).

Circularly Polarized Log-Periodic Antenna

A hybrid design uses crossed log-periodic antenna elements to produce circular polarization. The two elements are driven by 90° phase shifted signals. This is a straightforward antenna design for a broadband circularly polarized antenna, taking advantage of the large bandwidth of a log-periodic antenna design [88, 89].

Archimedean Spiral Antenna

The Archimedean spiral antenna is another format capable of producing circularly polarized fields [90]. However, we found this antenna type did not perform well in practice. The Archimedean spiral is a wide bandwidth antenna, similar to the log-periodic antenna; however, the spiral antenna can produce wideband circularly polarized radiation. This antenna format can achieve axial ratios of < 1 dB [91]. We build one Archimedean spiral antenna (seen in Figure 2.10(d)), winding the spiral to a geometry calculated with Matlab Antenna Designer. However, this antenna was tested and performed poorly, with > 8 dB power deviation with the rotation of the linear analyzer antenna. This indicates a large ellipticity to the polarization for this antenna. It is likely that this antenna performance suffered due to the build quality of this antenna, and not the antenna format itself.

Helical Antenna

The helical antenna, a common format for a circularly polarized microwave antenna, was chosen for the experiments below due to its simplicity. In contrast to a hybrid approached (e.g. the dual circular waveguide antenna), this antenna produces a circularly polarized field from a single signal generator source. Additionally, a helical antenna can produce a highly directional radiation pattern, useful in experiment where metal surfaces are present off axis.

A helical antenna was wrapped for 6.834 GHz, corresponding to the hyperfine splitting in rubidium-87. The helical antenna design was informed by ref. [92]. The Antenna Designer add-on to Matlab (R2019a) was used to calculate parameters to use in building the helical antenna, and to recalculate antenna properties for the specific design parameters chosen (wire thickness, ground plane radius). A helical antenna has an axial ratio (on the axis of the helix) described by the simple equation [92]

$$r_{(\text{on axis})} = \frac{2n + 1}{2n} \quad (2.6)$$

where n is the number of turns for the helix. The properties of many-turn helical antennas have also been studied by King and Wong in [93]. Following Eqn. 2.6, we tested helical antennas with 3 turns, 5 turns and more, as a low axial ratio is desired for the experiment performed in this thesis. Using the linear-analyzer test, the 3 turn helical antennas performed the best with 2-3 dB power fluctuation with the rotation of the receiving antenna. It is likely, as well, that some of this fluctuation is a result of spatial inhomogeneity in the radiation patterns of the antennas used in testing. Additionally, the 3 turn helical antennas were measured to have a higher gain at 6.834 GHz. The performance of the 3 turn helix is likely explained by better mechanical stability and symmetry along the length of the helix. In the end, the 3 turn helical antenna worked quite well for this application.

This type of antenna was studied in detail by John Kraus and collaborators [92]. Kraus is credited with the discovery of the axial mode of operation for helical antennas, as is used herein. This is a well characterized antenna format, commonly used satellite communications which benefit from features of this antenna such as a narrow directivity of radiation and a potential for high purity of circular polarization; properties which are also desirable for the cold atom experiment. As a common antenna format (around since 1946), there is a great deal of literature on properties of helical antennas, including research on different modifications to the helical antenna design, such as compact, low-profile helical antennas for use in devices or space-constrained applications [94, 95, 96], or tapered helical antennas to modify the off-axis polarization pattern [97].

Manufacturing a Helical Antenna

Due to the simplicity of the helical antenna, these antennas were constructed by hand, as described in this section. Using the calculated geometry for the antenna, a ground plane was cut out of two-sided copper circuit board. Additionally, a paper form was printed, cut, and folded into shape to hold the helix geometry fixed. The paper form was printed as three pieces (see Figure 2.13). Two of the pieces have a dots with at increments of

a quarter pitch of the helix and are folded to 90° lengthwise. Dots in the paper layouts indicate the location of holes, which are punched out and aligned using push pins. The helix of wire is pre-formed using incrementally smaller mandrels until the radius and pitch are approximately of the correct geometry. At this point, the helix is fed through the paper form. Then, this helix is soldered to a SMA connection through the ground plane, and the paper support is glued into place. One such assembled antenna is shown in Figure 2.14. This is an end-fed antenna and it operates in the axial mode of the helix. The main lobe for the axial mode operation can be seen in the 3D radiation pattern in Figure 2.12.

Table 2.2: Helical antenna design parameters for 6.834 GHz antenna operating in axial mode. This antenna produces circularly polarized radiation.

Antenna Parameters:	
Vertical spacing	1.3 cm
Radius	0.93 cm
Wire thickness	18 AWG
Ground plane radius	2.5 cm
Number of turns	3

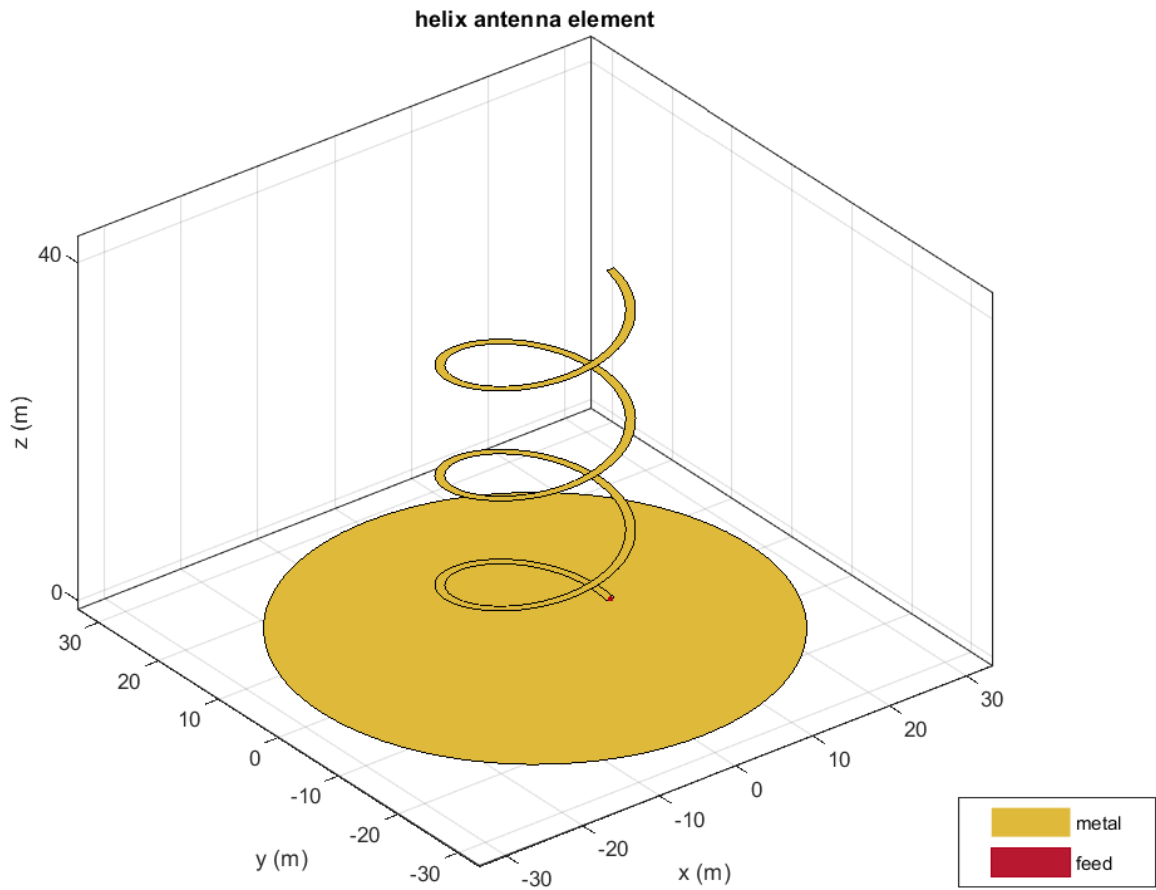


Figure 2.11: The Matlab Antenna Designer model of the helical antenna.

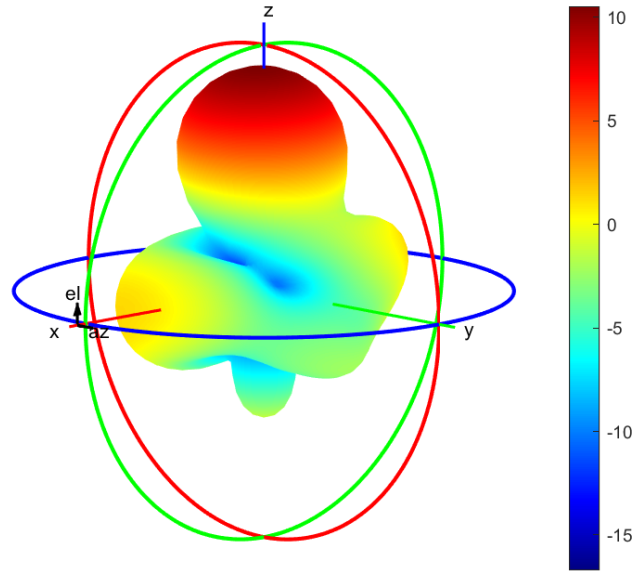


Figure 2.12: The Matlab generated 3D radiation profile. The color scale shows the gain in dB.

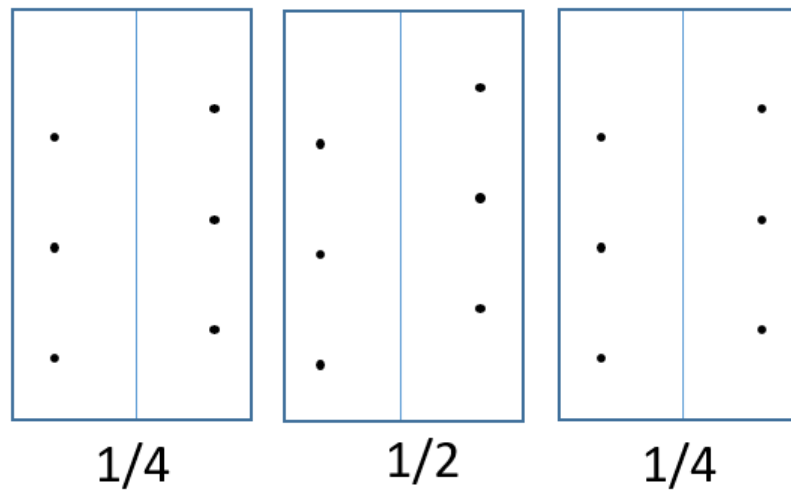


Figure 2.13: An example of the paper layout used to form the helical antenna. The blue rectangles are cut out and the two “1/4” rectangles are folded along the vertical lines. The holes are spaced vertically to match the pitch of helix at 1/4 turn (90°). The dots are punched out as guide holes for the helix of wire. The three layouts are used together to hold the geometry of the helix.

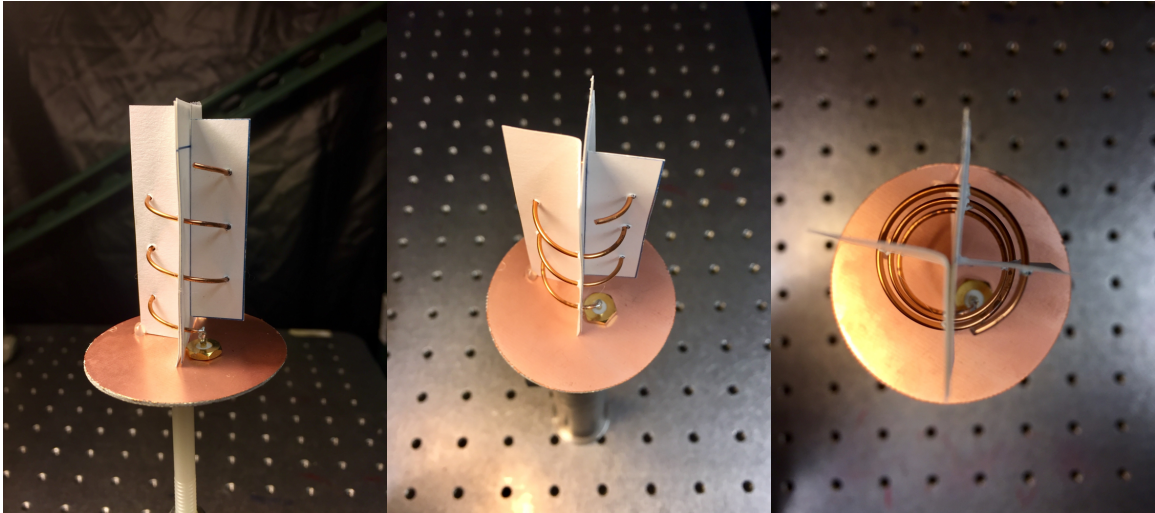


Figure 2.14: An assembled helical antenna (3 views). The paper form from Figure 2.13 can be seen supporting the helical coil.

Additional Antenna Designs

It is worth noting that there is a whole field of microwave antenna design. For the experiment here, the a helical antenna was a good choice due to its simplicity and directivity of radiation. Additionally, since the experiment needed an antenna at 6.8 GHz, and there were not readily accessible circularly polarized antennas available at this frequency, the decision was made to manufacture the antenna. This was feasible for the helical antenna. Given different constraints, there are many other antenna formats which could be considered for producing the circularly polarized field. For example, Prof. Greg Durgin suggested a patch-slot antenna for a circularly polarized field source. It is likely that this antenna format will be tested in future projects in the lab.

Microwave Setup

The microwave signal was produced with a HP E4422B signal generator. Since this signal generator has a maximum output frequency lower than 6.8 GHz, a frequency doubler (Marki D-0204) was used. In the experiment, the output is switched on and off with an

rf switch (Minicircuits ZASWA-2-50DR) controlled by an SRS pulse generator (model DG535). This switch is on the low frequency side (before the doubler) to provide higher switching isolation. The output of this circuit is amplified to approximately 4 W (maximum) of power using an Alga Microwave model ALPA 647240-50-01 amplifier. The amplifier output directly feeds one of the microwave antennas. With this setup, Rabi rates were measured at a maximum of approximately 14 kHz ($= 1/71 \mu\text{s}$) for a $\sigma_{\pm}, \Delta_{\pm}$ transition using the helical antenna.

CHAPTER 3

USING CIRCULARLY POLARIZED MICROWAVES TO SELECTIVELY DRIVE HYPERFINE TRANSITIONS

3.1 Abstract

We have demonstrated a method to use the circularly polarized radiation from a helical microwave antenna to differentially select one of two nearly degenerate transitions between the hyperfine ($F = 1, 2$) ground state ($5^2S_{1/2}$) levels in ^{87}Rb . The angular momentum conservation from the absorption of the circularly polarized microwave allows one transition to be preferentially selected. This is useful in control schemes where the presence of frequency-degenerate transitions interferes with control operations between specific levels. The circularly polarized microwave field is applied to drive a three-level Λ transition with high fidelity. Additionally, the selectivity of transitions provided by this polarized field is demonstrated at low magnetic fields where transitions become highly degenerate.

3.2 Introduction

3.2.1 Motivation and Background

Quantum control of spin states is essential for quantum information processing, quantum metrology, and studies of quantum many-body physics. There are many experimental systems available for studies of quantum mechanics, including trapped ions, cold neutral atoms, nuclear magnetic resonance experiments, superconducting (SQUID) circuits, and nitrogen-vacancy centers in diamond. In all these systems, control of the quantum state is necessary to initialize the system in a given quantum state, modify the dynamics of the system, or read out quantities describing the state of the system. Manipulations of the quantum state in these systems are accomplished with the application of external fields. Many

of these operations are performed quite simply with a single oscillating field, as more flexible methods of control are not as readily available. Nevertheless, sophisticated quantum control is at the heart of quantum information and quantum computing, where high fidelity manipulations of qubits is required to preserve the quantum state information within the computation [98], and many control methods for two-level (qubit) manipulations are well studied, just not applied in other contexts.

These control methods are of interest in ultracold neutral atom systems, which are used to study a diverse plethora of quantum many-body effects, from quantum phase transitions to many-body entanglement and squeezing. This is the type of system used for the experiments involving state control in this thesis. These neutral atoms feature a weak coupling to the environment and can be cooled to extremely low temperatures using conventional laser cooling and evaporative methods, realizing a very pure quantum system. These atoms feature long coherence times and often have hyperfine “clock” transitions which are first-order insensitive to magnetic fields. Because of this, neutral atoms have been used advantageously to implement atomic clocks which provide some of the most precise physical measurements in any system to date [99]. Alkali atoms (e.g. rubidium) are the most widely employed group of cold neutral atoms. Alkalis feature one valence electron and provide a level structure for states which can be manipulated easily with electric and magnetic fields. Due to the convenient spacing of the electronic transitions in these atoms, the necessary laser wavelengths are often readily available for laser cooling the atoms to prepare a cold sample for study. These alkalis were the first atoms used to realize Bose-Einstein condensation and have become one of the prominent systems for modern studies of quantum phenomena.

Our apparatus uses one of these alkali atoms: rubidium-87. These ^{87}Rb atoms are cooled to form a Bose-Einstein condensate of 40k-80k atoms within an optical dipole trap which, compared to a magnetic trap, allows for a spin degree of freedom. The spin states here are the ground-state hyperfine energy levels, a result of the coupling of angular mo-

menta between the electron and the nucleus. This hyperfine level structure is illustrated in Figure 3.1. At low magnetic field, the ground-state hyperfine structure is split into two levels of total angular momentum $F = 1, 2$, with each of these levels split into $2F + 1$ sub-levels. By applying oscillating magnetic fields with the appropriate frequency and polarization, transitions occur between these levels. The transitions between the $F = 1, 2$ levels represent microwave-frequency transitions, whereas transitions between the m_F states of a particular F level are radio-frequency (rf) transitions. This hyperfine structure features a clock transition, $|1, 0\rangle \rightarrow |2, 0\rangle$, which is first-order insensitive to magnetic field fluctuations and has been used as the basis for precise atomic clocks. These microwave and rf transitions, as well as optical-frequency transitions, can be used to perform quantum state control operations within the ground state hyperfine structure.

A Bose-Einstein condensate of ^{87}Rb in the $F = 1$ level provides a three-level spin-1 system, and features a quantum phase transition as a result of the spin-collisional interaction between atoms in the condensate. This interaction can be used to generate interesting quantum states such as spin-nematic squeezed states or Dicke states. In this system, methods to control the state of the BEC atoms are essential. Quantum state control applied within this spin-1 system can provide new avenues for studies of the entanglement generated in these states and allow for improved methods for quantum-enhanced metrology. Further, control within the hyperfine levels can be used to open this system to studies outside of the spin-1 system. One such application is the pseudo spin-1/2 system made by coupling the $|1, +1\rangle \leftrightarrow |2, -1\rangle$ states using a combination of microwave and rf fields, which has been used for two-level studies including spin-1/2 squeezing [100]. This shows how state control can be used to modify the dynamics of the quantum system. Other control applications include more sophisticated methods of state measurement. As an example, squeezing in the spin-1 ^{87}Rb BEC, or spin-nematic squeezing results in a quantum enhancement via squeezing of an observable which is not readily accessible without additional control of the state [23]. However, arbitrary control of the spin-1 state allows new possibilities such as

direct measurement of the squeezed quadrature of the spin-nematic squeezed state, which conventionally requires many measurements to perform a state tomography. Additionally, quantum state control provides the ability to apply an entangled quantum state as a resource to enhance measurements in novel ways. An example of this is a use of quantum state control of the spin-1 state in the ^{87}Rb BEC, where a spin-nematic squeezed state can be transformed into other metrologically valuable states. One such transformed state features a maximal spin vector length and a squeezed Larmor phase noise; two features which could be used to improve magnetometry based on this state.

There are multiple limitations which must be overcome in these neutral atom systems in order to realize effective state control. The fidelity of the manipulations must be kept high, with the noise introduced from the manipulations kept to a minimum. Rapid manipulations are desirable in order to perform manipulations quickly compared to the dynamics in the BEC. Additionally, rapid manipulations are less susceptible to decoherence such as Larmor decoherence, a result of the inherent sensitivity of the transitions within the hyperfine structure to the external magnetic field. However, degeneracies between transitions represent a significant limitation in realizing rapid, high-fidelity manipulations for control within the hyperfine states in ground state ^{87}Rb , and this problem is worsened by increasing the speed of manipulations. These degenerate transitions can be seen in Figure 3.1, Within the spin-1 ($F = 1$) states, the degeneracies prevent simple controlled coupling between adjacent pairs of m_F levels with a single rf oscillating field. Instead, transitions are driven from $m_F = 0$ to equal populations $m_F = \pm 1$. Other coherent transitions will involve a state outside of the $F = 1$ level. Therefore in order to control the specific states in this $F = 1$ spin-1 system, it is necessary to apply multiple oscillatory fields. Within the ground-state hyperfine levels, microwave frequency fields couple $F = 1 \leftrightarrow F = 2$. But once again, degeneracies exist between several of these microwave transitions; specifically, the transitions involving the $m_F = \pm 1$ states.

In this thesis, a avenue for control operations in the presence of these degeneracies

based on microwave transitions between hyperfine levels is explored. By identifying selection rules for the hyperfine microwave-frequency transitions, it will be shown that a circularly polarized microwave field applied in the appropriate orientation will discriminate between two otherwise frequency-degenerate transitions, selecting a transition of a matching polarization, while blocking a transition of the orthogonal polarization. This allows for a reduction of unwanted level couplings from the applied field. As a result, new high-fidelity control methods are made available using this circularly polarized microwave field. One such method is demonstrated via a two-photon coupling between two m_F states in the spin-1 levels. This Λ transition would otherwise suffer from degenerate couplings without the polarization selection. With transition selection from the circular microwave field polarization, a high fidelity coupling between two exclusive $F = 1, m_F$ states is made possible, allowing population transfer between two adjacent $F = 1, m_F$ states. Indeed, this polarized field provides an avenue for mitigating the complications of degenerate transitions, as well as undesired off-resonant driving resulting from the high field amplitudes used for rapid manipulations. This is explored through a study of the transition selectivity provided by the microwave field polarization at low external magnetic fields, where additional degeneracies appear due to the Fourier linewidth of the finite-duration microwave pulse and the small Zeeman splittings (the amplitude of the Zeeman splitting is Δ , see Figure 3.1 and surrounding discussion). This thesis describes the first work of this kind applied to a cold atom system, as circular polarization control has largely been unexplored within this cold atom context.

The use of microwave fields to drive hyperfine transitions in these systems is commonplace; however, circular polarization control has largely been unexplored within the cold atom context. However, the polarization selection of microwave-frequency transitions can be seen in some closely related fields. Let's explore some of these uses. One example is the use of a circularly polarized microwave field as a means to determine the sign of magnetic moments of molecules [101]. These measurements typically use a waveguide to

transmit circularly polarized microwaves. This tool has been available for more than half a century, as can be seen by a 1952 paper: ref. [102], which describes a microwave waveguide setup for the application of linearly or circularly polarized microwaves to measure the Zeeman effect in an absorption cell. A couple of experiments from within the same year implemented this waveguide type of setup, using the handedness of circular polarization to determine the sign of the g -factor of molecules [103, 104]. More recently, experiments have used a microstrip circuit to apply circularly polarized microwaves to address spins of nitrogen-vacancy centers in a diamond [105]. This microstrip is tunable via the two 90° phase shifted inputs, giving control over the ellipticity of the polarization. Another recent result showed manipulations of the spin of a nitrogen-vacancy center in diamond using circularly polarized microwave fields generated from two crossed wires positioned above the nitrogen-vacancy center [106]. Similarly, a combination of a coplanar waveguide microresonator and a dielectric resonator were implemented to generate a tunable circular polarization of a microwave field to control the spin of a Bismuth donor electron in silicon [107]. These show some of the variety in methods available for the generation of circularly polarized microwave fields for spin control.

As can be seen from these examples, there are multiple methods available to generate circularly polarized microwave fields. Indeed, outside of the context of spin transitions, circularly polarized microwaves are used widely in the communications field, and as a consequence, there are numerous well-studied antenna types designed to produce a radiated microwave field with circular polarization. An everyday example is seen with the global positioning system (GPS), which broadcasts a microwave-frequency signal with a right-handed circular polarization. For satellite communications, such as this GPS signal, a common antenna format is the axial-mode helical antenna. This antenna format, the helical antenna was used to produce the circularly polarized microwave field used in the experiments below.

3.2.2 Overview of Study

The aim of this study is to highlight the use of a simple helical antenna design to selectively drive hyperfine transitions while overcoming near degeneracies in a multi-level problem. The choice of the helical antenna allowed for a low-cost, but high performance solution built carefully by hand. The antenna designs were informed by simulations in Matlab Antenna Designer. An overview on the construction of the antenna design can be found in Chapter 2. A well-performing antenna was chosen and tested in the experiment using the magnetically sensitive hyperfine transitions of the ^{87}Rb atoms.

Use of this antenna for polarization-selective transitions necessitates control over the bias field direction relative to the direction of microwave propagation. This is a result of the decomposition of the microwave polarization into the coordinate basis set by the bias field seen by the atoms. The details of calibration and alignment of this bias field will be discussed. It will be seen that the structure of the hyperfine transitions provides a useful tool in this alignment procedure. Namely, a transition of orthogonal polarization is used as a metric in the alignment procedure. The cold atoms provide a highly precise measure of the microwave magnetic field. The atoms can be used to measure the full polarization ellipse of the microwave through measurements of Rabi oscillations in the hyperfine levels [108, 109]. However, for the experiments presented here, a measurement of the extremal points (of minimum and maximum Rabi rates) was sufficient.

With all these preliminary requirements satisfied—the antenna build, characterized, installed, and with the fields characterized and aligned—the hyperfine transitions in ^{87}Rb are studied. Known bias fields are applied in the correct fashion and the Rabi rates of the hyperfine transitions are measured. These measurements of Rabi frequencies can then be used to determine the strength of driving field for transitions corresponding to different polarization states. Thereby, the antenna is further characterized through measurements of these transition rates. In the special case of the circularly polarized antenna, it will be seen that hyperfine transitions can be either selected or blocked.

Centrally important to this study, the transition Rabi rates provide a measure of the discrimination provided by the circularly polarized field. It will be seen that a high level of discrimination ($> 45\times$) is achieved using the methods described herein. Although this study is within the hyperfine level structure ($F = 1, 2$) in rubidium-87, the requisite features exist in the hyperfine structure of many other atomic species as well; for example, sodium and cesium [110, 111], two other common elements used in cold atom experiments). The implementation of circularly polarized microwaves to selectively drive hyperfine transitions, in the presence of frequency-degenerate transitions, represents the first success in this study. With this newly-developed tool, it becomes possible to explore a couple of important applications.

First, this polarized field is used to couple only three levels (out of all eight levels in the $F = 1, 2$ hyperfine structure) to drive an otherwise degenerate “ Λ ” system. This is the structure of a Raman transition as discussed in Chapter 1, and has applications to more complicated all-microwave control schemes, such as non-adiabatic holonomic gates [67] or as the basis of a tripod transformation. The tripod transformation is discussed later in this thesis, where different methods were attempted to implement this four-level tripod control.

Second, the circularly polarized field is shown to selectively drive hyperfine transitions in low bias fields, where the Zeeman splitting of the magnetic sublevels is small and within the spectral linewidth of the driving microwave field. In such low fields, the states are scrambled without the polarization selection, as there are couplings between multiple levels in the hyperfine structure. This chapter will discuss the theory behind these ideas and the experiment itself (subject of the next chapter).

3.2.3 Preliminaries

It is useful to start with a discussion of the hyperfine structure of rubidium-87. The ground state ($5^2S_{1/2}$) level structure can be seen in Figure 3.1. There are two hyperfine levels as a result of the coupling between the electron angular momentum and the nuclear angular

momentum, where F is the total angular momentum $\mathbf{F} = \mathbf{J} + \mathbf{I}$. Here \mathbf{I} is the nuclear angular momentum and $\mathbf{J} = \mathbf{L} + \mathbf{S}$ is the total electron angular momentum, where \mathbf{L} is the orbital angular momentum and \mathbf{S} is the electronic spin angular momentum. For the electronic ground state, $J = 1/2$ ($L = 0$ and $S = 1/2$) and the nuclear spin $I = 3/2$. This gives two values for F , namely $F = |J - I|, (J + I) = 1, 2$. These hyperfine levels are further split into magnetic sublevels, with $2F + 1$ sublevels for each value of F ; the quantum number for these sublevels is m_F , the quantum number for the projection of the angular momentum. For $F = 1$, m_F has the possible values of $m_F = -1, 0, +1$. Similarly, for $F = 2$, m_F can take the values $m_F = -2, -1, 0, +1, +2$. The levels can be coupled via the application of an oscillating magnetic field at a frequency near the the splitting between the levels. These transitions between levels satisfy $\Delta F = 0, \pm 1$ and $\Delta m_F = 0, \pm 1$. The $\Delta F = 0$ transitions represent transitions in the radio frequency (rf) (typically $10^4 - 10^5$ Hz), whereas the $\Delta F = \pm 1$ transitions are of microwave frequencies (near 6.8 GHz).

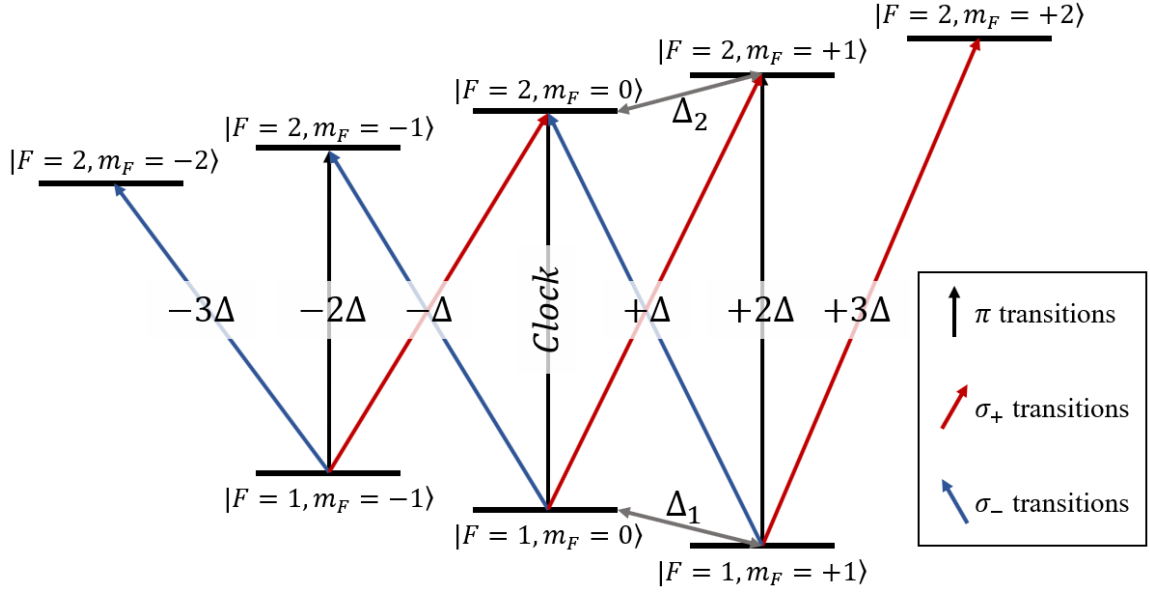


Figure 3.1: The ground state $5^2S_{1/2}$ hyperfine energy levels in rubidium-87. The approximate energy spacings are labeled in terms of $\Delta \approx 700$ Hz/mG, giving the shift due to the linear Zeeman effect of the transitions compared to the clock transition. The spacing between each of the m_F levels for $F = 1$ and $F = 2$ are $\Delta_1 = 702.4$ Hz/mG and $\Delta_2 = 699.6$ Hz/mG, respectively.

Hyperfine Hamiltonian

The hyperfine Hamiltonian resulting from the coupling between the total electron angular momentum and the nuclear angular momentum has the form at zero field [112]

$$H_{hfs} = A_{hfs} \mathbf{I} \cdot \mathbf{J} = A_{hfs} \mathbf{I} \cdot \mathbf{S} \quad (3.1)$$

where the second equality is true for the ground state since $L = 0$, and $A_{hfs} = \hbar \cdot 3.41734130545215(5)$ GHz is the hyperfine structure constant [113]. The hyperfine Hamiltonian H_{hfs} has eigenenergies of $\frac{1}{2}A_{hfs}(F(F+1) - I(I+1) - S(S+1))$, which for $F = 1$ and $F = 2$ which correspond to $-\frac{5}{4}A_{hfs}$ and $\frac{3}{4}A_{hfs}$, respectively. Therefore there is a total splitting of $2A_{hfs} = \hbar \cdot 6.8346826109043(1)$ GHz for the ground state hyperfine levels.

Zeeman Hamiltonian – Static Magnetic Field

In an external magnetic field, the hyperfine levels $F = 1, 2$ are each split into $2F + 1$ magnetic sublevels are separated in energy by the Zeeman effect. At zero field, these $2F + 1$ levels are degenerate but in non-zero fields this degeneracy is lifted. The Hamiltonian for the atom in a static magnetic field has the form

$$H_B = \mu_B \mathbf{B} \cdot (g_S \mathbf{S} + g_I \mathbf{I}) \quad (3.2)$$

with g_S , and g_I being the g -factors for the electron spin ($g_S = 2.0023193043737(80)$ [114]) and the nucleus ($g_I = -0.0009951414(10)$ [115]) describing the magnetic dipole moments, and μ_B is the Bohr magneton. If the magnetic field is taken to be in the z direction, Eqn. 3.2 can be written as

$$H_B = \mu_B B_z (g_S m_S + g_I m_I) \quad (3.3)$$

Here, m_S and m_I are the projection quantum numbers for the electron spin and nuclear angular momentum, respectively, and B_z is the z component of the magnetic field. In low fields, such that the Zeeman shift is small compared to the hyperfine splitting, F is a good quantum number. In this low field, linear-Zeeman regime, the zeeman splitting to first order is written in the linear form [116]

$$H_B = \mu_B g_F m_F B_z \quad (3.4)$$

where

$$g_F = g_S \frac{F(F+1) - I(I+1) + S(S+1)}{2F(F+1)} + g_I \frac{F(F+1) + I(I+1) - S(S+1)}{2F(F+1)} \quad (3.5)$$

From Eqn. 3.4, the linear Zeeman splitting between the m_F sublevels (see Figure 3.1) is $\Delta = \mu_B g_F B_z m_F \approx 700 \text{ Hz/mG}$ for the applied (static) bias field in the z direction.¹ At higher fields, the Zeeman shift of the ground state levels is no longer linear in the magnetic field strength and is given instead by the Breit-Rabi formula [112].

Zeeman Hamiltonian – Oscillating Magnetic Field

Similarly to the static field, an oscillating microwave field interacts via the Hamiltonian

$$H'_B = \mu_B g_s \mathbf{B}' \cdot \mathbf{S}, \quad (3.6)$$

where \mathbf{B}' is the applied oscillating magnetic field, $\mathbf{B}' = \mathbf{B}'_0 \cos(\omega_B t)$. Compared to Eqn. 3.2, the nuclear term $\mu_B g_I \mathbf{B}' \cdot \mathbf{I}$ has been neglected since this interaction is orders of magnitude smaller. Given that this oscillating field can be in any direction, we use the Pauli matrices to write $S_i = (\hbar/2)\sigma_i$ for each axis $i = (x, y, z)$ to compute the dot product of \mathbf{S} with the magnetic field vector \mathbf{B}' , having components with amplitudes B'_i . The Hamiltonian Eqn. 3.6 is written as a linear combination of these components

$$H'_{B,i} = \mu_B g_s B'_i (\hbar/2) \sigma_i \cos(\omega_B t) \quad (3.7)$$

Matrix elements

In describing the hyperfine structure via the Hamiltonian Eqn. 3.1, states are written in the coupled representation or $|F, m_F\rangle$ basis. However, the Zeeman Hamiltonian is not diagonal in this basis. Therefore, it is necessary to transform to the uncoupled basis $|m_I, m_S\rangle \equiv |I = 3/2, m_I\rangle \otimes |S = 1/2, m_S\rangle$. To understand the action of this Hamiltonian (Eqn. 3.6) on states in the coupled representation $|F, m_F\rangle$, the basis vectors in the coupled representation are decomposed into this uncoupled representation. This allows for the calculation of transition matrix elements $\mu_B g_s B'_i (\hbar/2) \cos(\omega_B t) \langle F, m_F | I_{nuc} \otimes \sigma_i | F', m'_F \rangle$, where Pauli operators σ_i

¹This applied field sets the quantization axis (z).

act on the spin of each state in the uncoupled basis $|S, m_S\rangle$, and I_{nuc} is the identity operator for the nuclear spin state $|I, m_I\rangle$. For notation, let $\Sigma_i = I_{nuc} \otimes \sigma_i$. This transformation from coupled to uncoupled basis states is made through the formalism of Clebsch-Gordan coefficients. Each state $|F, m_F\rangle$ is expressed as a sum of $\sum_{m_I, m_S} C_{m_I, m_S, m_F}^{I, S, F} |m_I, m_S\rangle$, where $C_{m_I, m_S, m_F}^{I, S, F} = \langle m_I, m_S | F, m_F \rangle$ is the Clebsch-Gordan coefficient.² The transition matrix elements are calculated as

$$\begin{aligned} \langle F, m_F | I_{nuc} \otimes \sigma_i | F', m'_F \rangle = \\ \sum_{m_I, m_S} \sum_{m'_I, m'_S} \langle F, m_F | m_I, m_S \rangle \langle m_I, m_S | \Sigma_i | m'_I, m'_S \rangle \langle m'_I, m'_S | F', m'_F \rangle \end{aligned} \quad (3.8)$$

where $\langle m_I, m_S | \Sigma_i | m'_I, m'_S \rangle = \delta_{m_I, m'_I} \langle m_S | \sigma_i | m'_S \rangle$, and δ_{m_I, m'_I} is the Kronecker delta. We define an ordered basis for the coupled representation vectors, $|F, m_F\rangle$. This ordering is shown in Eqn. 3.9 and will also be the ordering used for the rows and columns of the transition matrices below.

$$\Psi = \begin{bmatrix} |1, -1\rangle \\ |1, 0\rangle \\ |1, +1\rangle \\ |2, -2\rangle \\ |2, -1\rangle \\ |2, 0\rangle \\ |2, +1\rangle \\ |2, +2\rangle \end{bmatrix} \quad (3.9)$$

²Throughout this thesis, states in the $|F, m_F\rangle \equiv |ISFm_F\rangle$ basis will be represented concisely with just the corresponding values of F and m_F , as in $|F = 1, m_F = \pm 1\rangle = |1, \pm 1\rangle$

$$\langle F, m_F | \Sigma_z | F', m'_F \rangle = \begin{pmatrix} \frac{1}{2} & 0 & 0 & 0 & -\frac{\sqrt{3}}{2} & 0 & 0 & 0 \\ 0 & 0 & 0 & 0 & 0 & -1 & 0 & 0 \\ 0 & 0 & -\frac{1}{2} & 0 & 0 & 0 & -\frac{\sqrt{3}}{2} & 0 \\ 0 & 0 & 0 & -1 & 0 & 0 & 0 & 0 \\ -\frac{\sqrt{3}}{2} & 0 & 0 & 0 & -\frac{1}{2} & 0 & 0 & 0 \\ 0 & -1 & 0 & 0 & 0 & 0 & 0 & 0 \\ 0 & 0 & -\frac{\sqrt{3}}{2} & 0 & 0 & 0 & \frac{1}{2} & 0 \\ 0 & 0 & 0 & 0 & 0 & 0 & 0 & 1 \end{pmatrix} \quad (3.10)$$

The matrix Eqn. 3.10 gives the transition matrix elements for couplings due to the z component of the microwave magnetic field. The elements of this matrix are calculated via Eqn. 3.8, and the rows and columns ordered similarly to Eqn. 3.9. The transition matrices for all the microwave field components (x , y , and z) can be found in the appendices of this thesis.

Each of these matrices gives transition matrix elements for linearly polarized microwave fields along each corresponding axis, where the z -axis is the quantization axis defined by the direction of the bias magnetic field. To look at circularly polarized microwaves, a field circulating in the xy -plane is constructed through the sum of x and y fields. Following Eqn. 3.7, the Hamiltonian for a circularly polarized field will have the form

$$H'_{B,i} = \mu_B g_s (\hbar/2) B' (\cos(\omega_B t) \sigma_x \pm \sin(\omega_B t) \sigma_y) \quad (3.11)$$

Here, the handedness of circular polarization is determined by the sign difference between the x and y terms. Using the transition matrices for the x and y fields as described above, an interaction picture Hamiltonian (described below) is formed for each handedness of circular polarization from Eqn. 3.11. Taking the RWA and eliminating the high frequency

terms leaves different non-zero matrix elements between the two circular polarizations. The amplitudes of the remaining matrix elements for each of the circular polarizations are given in matrix form below with the same ordering as was used above such that rows and columns are ordered similarly to Eqn. 3.9. The transition strengths for the σ_+ transitions are given below in the matrix Eqn. 3.12.

$$\begin{pmatrix} 0 & -\frac{1}{2\sqrt{2}} & 0 & 0 & 0 & \frac{1}{2\sqrt{2}} & 0 & 0 \\ -\frac{1}{2\sqrt{2}} & 0 & -\frac{1}{2\sqrt{2}} & 0 & 0 & 0 & \frac{\sqrt{3}}{2} & 0 \\ 0 & -\frac{1}{2\sqrt{2}} & 0 & 0 & 0 & 0 & 0 & \frac{\sqrt{3}}{2} \\ 0 & 0 & 0 & 0 & \frac{1}{2} & 0 & 0 & 0 \\ 0 & 0 & 0 & \frac{1}{2} & 0 & \frac{\sqrt{3}}{2} & 0 & 0 \\ \frac{1}{2\sqrt{2}} & 0 & 0 & 0 & \frac{\sqrt{3}}{2} & 0 & \frac{\sqrt{3}}{2} & 0 \\ 0 & \frac{\sqrt{3}}{2} & 0 & 0 & 0 & \frac{\sqrt{3}}{2} & 0 & \frac{1}{2} \\ 0 & 0 & \frac{\sqrt{3}}{2} & 0 & 0 & 0 & \frac{1}{2} & 0 \end{pmatrix} \quad (3.12)$$

Similarly, the σ_- transitions are given below in the matrix Eqn. 3.13.

$$\begin{pmatrix} 0 & -\frac{1}{2\sqrt{2}} & 0 & -\frac{\sqrt{3}}{2} & 0 & 0 & 0 & 0 \\ -\frac{1}{2\sqrt{2}} & 0 & -\frac{1}{2\sqrt{2}} & 0 & -\frac{\sqrt{3}}{2} & 0 & 0 & 0 \\ 0 & -\frac{1}{2\sqrt{2}} & 0 & 0 & 0 & -\frac{1}{2\sqrt{2}} & 0 & 0 \\ -\frac{\sqrt{3}}{2} & 0 & 0 & 0 & \frac{1}{2} & 0 & 0 & 0 \\ 0 & -\frac{\sqrt{3}}{2} & 0 & \frac{1}{2} & 0 & \frac{\sqrt{3}}{2} & 0 & 0 \\ 0 & 0 & -\frac{1}{2\sqrt{2}} & 0 & \frac{\sqrt{3}}{2} & 0 & \frac{\sqrt{3}}{2} & 0 \\ 0 & 0 & 0 & 0 & 0 & \frac{\sqrt{3}}{2} & 0 & \frac{1}{2} \\ 0 & 0 & 0 & 0 & 0 & 0 & \frac{1}{2} & 0 \end{pmatrix} \quad (3.13)$$

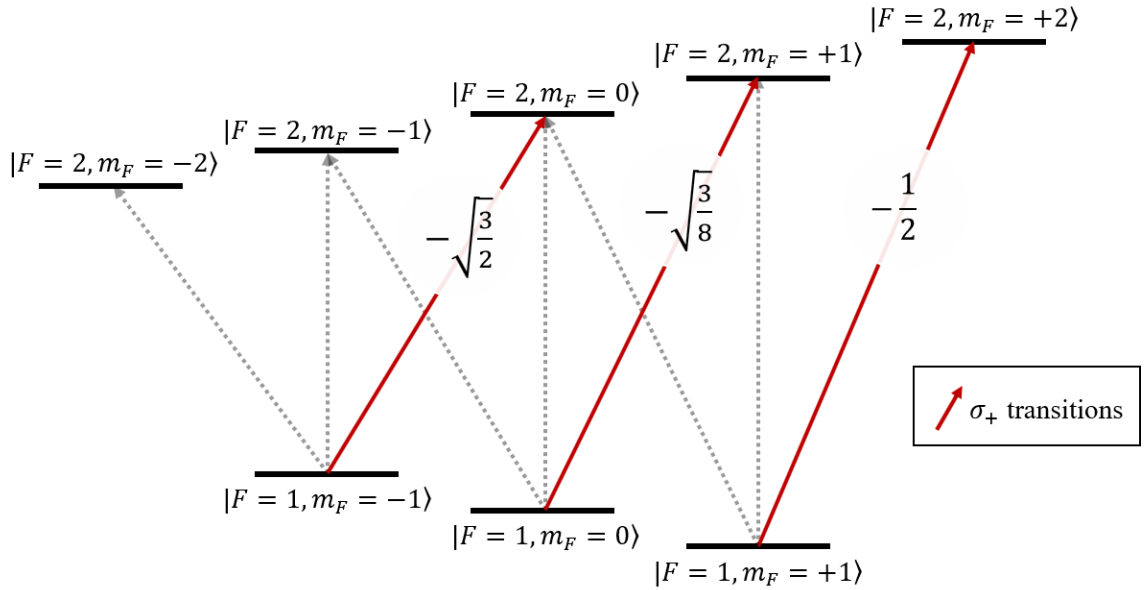


Figure 3.2: The ground state hyperfine structure. The matrix elements from matrix Eqn. 3.12 are shown with the corresponding σ_+ transitions, illustrating the selected transitions corresponding to the non-zero matrix elements for microwave transitions for a σ_+ polarized microwave field.

Selection rules

From these transition matrix elements (Eqns. 3.10, 3.12, and 3.13), some selection rules are apparent. For a purely σ_+ or σ_- polarized driving field, (see the circular polarization transition matrices), the non-zero transition elements feature $\Delta m_F = +1$ or -1 respectively. For the π polarized field, the matrix elements are $\langle F, m_F | \Sigma_z | F', m'_F \rangle$. From the matrix elements, it is clear that the π polarization couples levels through $\Delta m_F = 0$ transitions. Note that these selection rules describe the selectivity of the transitions based upon the polarization of the microwave field. The selection rules can similarly be understood from conservation of angular momentum between the hyperfine states and microwave photons. These selection rules based on polarization are an essential point for the work that follows—from

the Hamiltonian Eqn. 3.7, there are sets of transitions elements that couple exclusively to either right- or left-handed circular polarized microwave field. One can therefore use a circularly polarized microwave magnetic field to selectively drive transitions. This is desirable in cases where degeneracies exist with respect to transition frequencies, as is the case in the ^{87}Rb hyperfine structure!

Interaction Picture

The interaction picture is useful to solve such time-dependent problems as this oscillating field problem [56]. To transform to the interaction picture Hamiltonian, we write

$$H_{B,I} = e^{iH_0t/\hbar} H'_B e^{-iH_0t/\hbar} \quad (3.14)$$

The Hamiltonian H'_B is from Eqn. 3.6. For H_0 we will use $H_{hfs} + H_B$, with the low-field linear form of $H_B = \mu_B g_F m_F B_z$ (Eqn. 3.4). H_0 is written in matrix form: $H_0/\hbar =$

$$\begin{pmatrix} -\Delta + \frac{3\omega_0}{8} & 0 & 0 & 0 & 0 & 0 & 0 & 0 \\ 0 & \frac{3\omega_0}{8} & 0 & 0 & 0 & 0 & 0 & 0 \\ 0 & 0 & \Delta + \frac{3\omega_0}{8} & 0 & 0 & 0 & 0 & 0 \\ 0 & 0 & 0 & -2\Delta - \frac{5\omega_0}{8} & 0 & 0 & 0 & 0 \\ 0 & 0 & 0 & 0 & -\Delta - \frac{5\omega_0}{8} & 0 & 0 & 0 \\ 0 & 0 & 0 & 0 & 0 & -\frac{5\omega_0}{8} & 0 & 0 \\ 0 & 0 & 0 & 0 & 0 & 0 & \Delta - \frac{5\omega_0}{8} & 0 \\ 0 & 0 & 0 & 0 & 0 & 0 & 0 & 2\Delta - \frac{5\omega_0}{8} \end{pmatrix}$$

Where $\omega_0 = 2A_{hfs} \approx 6.834$ GHz and $\Delta = \mu_B g_F B_z m_F \approx 700$ Hz/mG is the linear Zeeman splitting for the applied (static) bias field in the z direction.

From this interaction picture Hamiltonian, the rotating wave approximation is typically made, where we eliminate the high frequency exponential terms of frequencies $\approx \omega_0 + \omega_B$, as these average in time to 0, with the assumption that $\delta = \omega_B - \omega_0 \ll \omega_0 + \omega_B$. Here, δ is the detuning of the applied oscillating field (at ω_B) from the natural transition frequency

(ω_0). Once the RWA is applied, many of the matrix elements of the $H_{B,I}$ matrix are set to 0, except for those corresponding to transitions with separations near the driving field frequency, simplifying the problem.

As an example, the Hamiltonian matrices related to the clock transition ($|1, 0\rangle \rightarrow |2, 0\rangle$) are shown below. These matrices are given assuming the RWA and assuming that the driving microwave field is near resonance with the clock transition but far detuned from other transitions. In this case, only the matrix elements corresponding to the the states in the clock transition are retained as all other elements are set to 0 using the RWA. This transition is due to the interaction with the B_z component of the microwave field, and the corresponding matrix elements are obtained from the matrix Eqn. 3.10.

$$H_0 = \hbar\omega_0 \begin{pmatrix} \frac{3}{8} & 0 \\ 0 & -\frac{5}{8} \end{pmatrix} \quad (3.15)$$

$$H'_B = \hbar\Omega_z \cos(\omega_B t) \begin{pmatrix} 0 & -1 \\ -1 & 0 \end{pmatrix} \quad (3.16)$$

The interaction picture Hamiltonian, Eqn. 3.17, is obtained from Eqn. 3.14 using the Hamiltonian matrices H_0 (Eqn. 3.15) and H'_B (Eqn. 3.16). The cosine function for the oscillating field from Eqn. 3.16 is expanded into exponential terms, and the high frequency exponential terms are eliminated with the RWA resulting in the simplified interaction picture Hamiltonian within the RWA, Eqn. 3.17.

$$H_{B,I} = -\frac{\hbar\Omega_z}{2} \begin{pmatrix} 0 & e^{-i\delta t} \\ e^{i\delta t} & 0 \end{pmatrix} \quad (3.17)$$

8 Level Simulation

The full 8×8 transition matrices can be used to simulate the evolution of a state consisting of a combination of all 8 hyperfine levels interacting with microwave fields. To do so, the interaction picture Hamiltonian is written as below (Eqn. 3.18) with each component (x , y , and z) of the microwave magnetic field ($B_x(t)$, $B_y(t)$, and $B_z(t)$) added in. Each component can be the sum of multiple oscillating terms to simulate the application of multiple microwave fields. For example, $B_z(t) = B_1 \cos(\omega_1 t) + B_2 \cos(\omega_2 t)$ would represent two oscillating magnetic fields in the z direction with amplitudes B_1 , B_2 and frequencies ω_1 , ω_2 .

$$\begin{aligned}
 H_{B,I} = e^{iH_0 t/\hbar} & \left(\frac{\mu_B g_s \hbar}{2} \right) (B_x(t) \langle F, m_F | \Sigma_x | F', m'_F \rangle \\
 & + B_y(t) \langle F, m_F | \Sigma_y | F', m'_F \rangle \\
 & + B_z(t) \langle F, m_F | \Sigma_z | F', m'_F \rangle) e^{-iH_0 t/\hbar}
 \end{aligned} \tag{3.18}$$

The evolution of the state is then calculated through the Schrödinger equation where Ψ is an 8-dimensional vector containing the 8 hyperfine basis states as in Eqn. 3.9.

$$i\hbar \frac{d\Psi}{dt} = H_{B,I} \Psi \tag{3.19}$$

3.2.4 Bias Field Direction vs Transition Strength

An important aspect in the use of circularly polarized microwaves is related to the decomposition of the circular polarization into two linearly polarized components. Through this decomposition, a circularly polarized microwave field can be expressed as a combination of projections of the microwave field into other polarization unit vectors in a different coordinate system. The coordinate system with the z -axis set by the bias field, which we also use as the quantization axis for the atoms, is of particular interest here. If the bias field is not aligned with the microwave k -vector, that is, normal to the plane of a circulating mag-

netic field in the circularly-polarized case, projections into the other components as seen by the atoms are able to drive the undesired transitions. It is therefore useful to understand the polarization basis, and work through some of calculations for the expected Rabi rates for various field orientations compared to the plane of circulating magnetic field for the microwave.

Let us start by defining some basis vectors

$$\mathbf{e}_x = \begin{pmatrix} 1 \\ 0 \\ 0 \end{pmatrix}, \mathbf{e}_y = \begin{pmatrix} 0 \\ 1 \\ 0 \end{pmatrix}, \mathbf{e}_z = \begin{pmatrix} 0 \\ 0 \\ 1 \end{pmatrix}$$

Additionally, we need the linear combinations of these basis vectors which will define the orthogonal, circular unit vectors in the xy -plane. These are

$$\mathbf{e}_{\pm} = \frac{\mp 1}{\sqrt{2}} (\mathbf{e}_x \pm i\mathbf{e}_y) = \frac{1}{\sqrt{2}} \begin{pmatrix} \mp 1 \\ -i \\ 0 \end{pmatrix}$$

The magnetic field of the microwave is expressed as components along each of these unit vectors. From our procedure of nulling the clock transition, described below, the circular polarized microwave field should have a zero-valued projection in \mathbf{e}_z aligned with the bias field once the field is aligned to selectively drive σ_{\pm} transitions. With the helical antenna, assuming perfect circular polarization of one handedness, the polarization is simply one of the states \mathbf{e}_{\pm} . As an example, let's choose \mathbf{e}_+ .

As we rotate the bias field, without loss of generality we can say we rotate about \mathbf{e}_x , the projection of \mathbf{e}_x remains the same. However, the projection of \mathbf{e}_y shrinks and \mathbf{e}_z grows. At a 90° rotation of the bias compared to the microwave \mathbf{k} -vector, the projection on \mathbf{e}_y is zero. Instead this amplitude is now projected into \mathbf{e}_z .

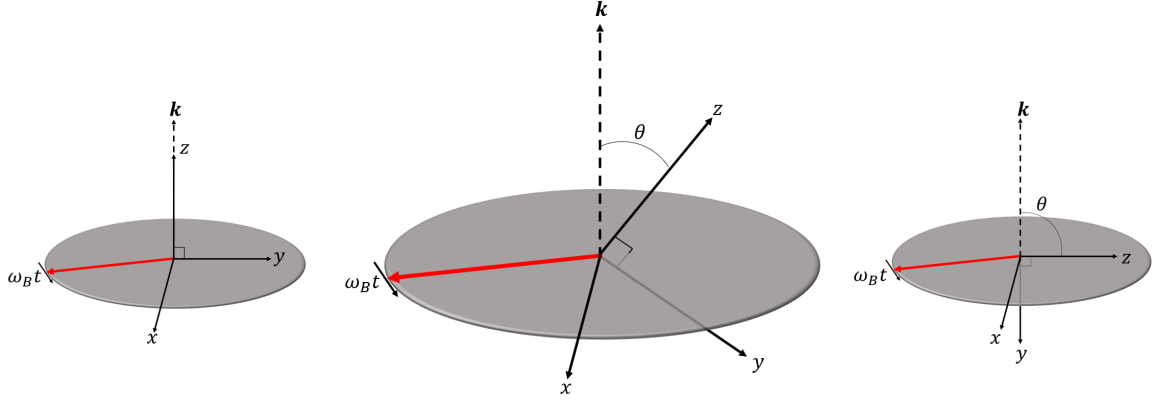


Figure 3.3: An illustration showing the plane of circulating microwave magnetic field (Gray plane with red field vector) and the coordinate system as seen by the atoms rotated about the x -axis by the angle θ . The z -axis represents the bias field direction and the quantization axis for the atoms.

The polarization state as seen by the atoms is $\mathbf{f}(\theta) = \frac{-1}{\sqrt{2}} (\mathbf{e}_x + i\cos(\theta)\mathbf{e}_y + \sin(\theta)\mathbf{e}_z)$ where θ is the angle of the bias field relative to the normal vector to the plane containing the circulating microwave field.

The inverse linear combinations for σ_{\pm} are now useful. We can write

$$\mathbf{e}_x = \frac{\mathbf{e}_- - \mathbf{e}_+}{\sqrt{2}}$$

$$\mathbf{e}_y = i \frac{\mathbf{e}_+ + \mathbf{e}_-}{\sqrt{2}}$$

Using these combinations, we can write the polarization vector as

$$\mathbf{f}(\theta) = -\frac{1}{\sqrt{2}} \left(\frac{\mathbf{e}_- - \mathbf{e}_+}{\sqrt{2}} + (i)^2 \cos(\theta) \frac{\mathbf{e}_+ + \mathbf{e}_-}{\sqrt{2}} + \sin(\theta)\mathbf{e}_z \right)$$

Which simplifies to:

$$\mathbf{f}(\theta) = \frac{1}{2}\mathbf{e}_+ (1 + \cos(\theta)) + \frac{1}{2}\mathbf{e}_- (1 - \cos(\theta)) - \frac{1}{\sqrt{2}}\mathbf{e}_z (\sin(\theta))$$

With this expression for the polarization vector, we take the dot-product with each of the basis vectors, to obtain the amplitude for each polarization component:

$$\mathbf{f}(\theta) \cdot \mathbf{e}_+ = \frac{1}{2}(1 + \cos(\theta))$$

$$\mathbf{f}(\theta) \cdot \mathbf{e}_- = \frac{1}{2}(1 - \cos(\theta))$$

$$\mathbf{f}(\theta) \cdot \mathbf{e}_z = \frac{1}{\sqrt{2}}(\sin(\theta))$$

Each of these components gives the relative strength of coupling to each of the transition polarizations (σ_z , σ_+ , σ_-) as the angle between the k -vector of the \mathbf{e}_+ microwave field and the bias field is varied. These relative strengths are shown graphically in Figure 3.4.

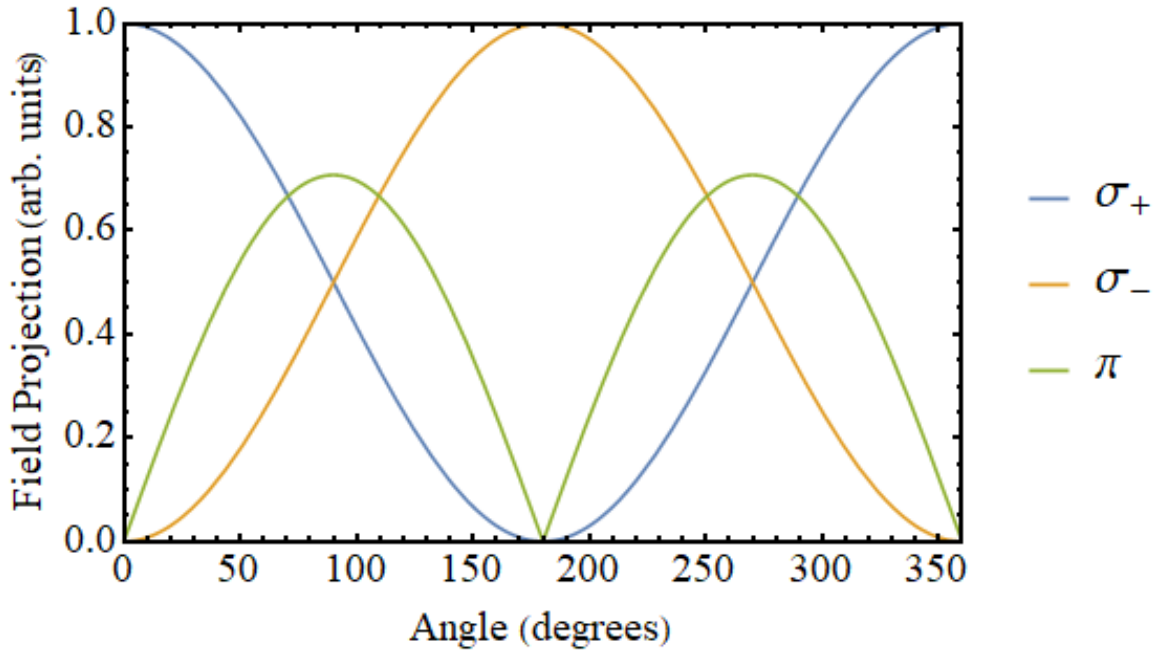


Figure 3.4: The angular dependence of the σ_{\pm} and π transitions compared to the field direction. The curves show the amplitude of the \mathbf{e}_+ microwave field projected into the atomic basis as the field is rotated about the x -axis.

Concluding preliminaries

From the above discussion, it is clear that the polarization of the driving field will dictate the strengths of couplings to different states according to the corresponding transition matrix elements. We were able to look at the projection of a circularly polarized field into a coordinate system (i.e. one defined by the bias field direction) that rotated about the plane of circulation of the microwave magnetic field. This shows the necessity of alignment of the oscillating field normal to the bias field axis for the atoms in order to selectively couple levels through the polarization selection.

CHAPTER 4

CIRCULARLY POLARIZED MICROWAVES – EXPERIMENTAL MEASUREMENTS

This chapter will describe the experiments performed using circularly polarized microwave fields applied to the cold cloud of ^{87}Rb to select hyperfine transitions. This chapter will detail the preliminary experimental procedures related to calibrating and aligning the applied magnetic field which are essential steps in order use the circularly polarized microwave field in the ways described. Following these prerequisites, experiments using this polarized field will be described. Selective two-level Rabi transitions are measured and indeed show the selection and blocking of hyperfine transitions of differing σ_{\pm} . Following the success of this selection, three-level Λ transitions are demonstrated, connecting two $F = 1, m_F$ levels via one of the $F = 2$ states. Additionally, the selection of hyperfine transitions is investigated in low magnetic fields, where the transitions become multiply degenerate, yet can be resolved via the microwave polarization selection.

4.1 Experimental Procedure

The starting point, with a working cold atom apparatus already implemented, was the installation of the new microwave antenna to transmit circularly polarized microwave fields into the chamber. A helical antenna was mounted above the vacuum chamber and its axis was directed towards the trap location (in the xy -plane of the chamber). There was a clear line of sight from the antenna through large borosilicate glass viewports on the top and bottom of vacuum chamber, passing through the trap location, and bench top tests showed no measurable attenuation through a similar pryex viewport. The bias field had to be orientated relative to the direction of the magnetic field applied by this antenna. Therefore, the magnetic field had to be calibrated (“zeroed”) and orientated to point in the correct

direction for the given antenna alignment. These two procedures—field calibration and orientation—are detailed in the next sections.

4.1.1 Zeroing the Field

The BEC apparatus features three orthogonal pairs of bias coils used to both cancel the ambient magnetic field around the experiment and to apply desired bias fields. The amplitude of the field at the location of the atoms is determined by measuring the resonance frequency of a magnetically sensitive transition, e.g. $|1, 0\rangle \rightarrow |2, 1\rangle$. In this case, the offset in the measured frequency compared to the frequency of the hyperfine splitting (i.e. the clock frequency) gives a value for the level spacing Δ , which at low fields is well approximated with a simple linear dependence ($\Delta = B_z \cdot 700 \text{ Hz/mG}$). We apply several bias field amplitudes along the direction of each axis and measure the resulting resonance frequency seen by the atoms, each resonance frequency giving a value for the amplitude $|B_{meas}|$ as measured by the atoms. We use these results to calculate a least-squares fit to

$$B_{meas} = \frac{1}{700 \text{ Hz/mG}} \Delta_{meas}$$

$$= \sqrt{\left(B_x + \frac{dB_x}{dV_x} V_x\right)^2 + \left(B_y + \frac{dB_y}{dV_y} V_y\right)^2 + \left(B_z + \frac{dB_z}{dV_z} V_z\right)^2}$$

where Δ_{meas} is the measured resonance frequency, and B_{meas} is the corresponding magnetic field amplitude, B_i ($i = x, y, z$) is the offset field in each axis to be canceled out, $\frac{dB_i}{dV_i}$ is the response in magnetic field to the control voltage V_i ($i = x, y, z$) for each bias coil current supply. The fit parameters determine the correct bias field to cancel the ambient field along each direction and also provide a calibration for the applied bias field compared to the control voltage (dB/dV) for each axis. This calibration allows for an accuracy of $\approx 1^\circ$ for the bias field direction at an applied bias of 200 mG, and gives a zero-field ($\pm 1 \text{ mG}$) starting point.

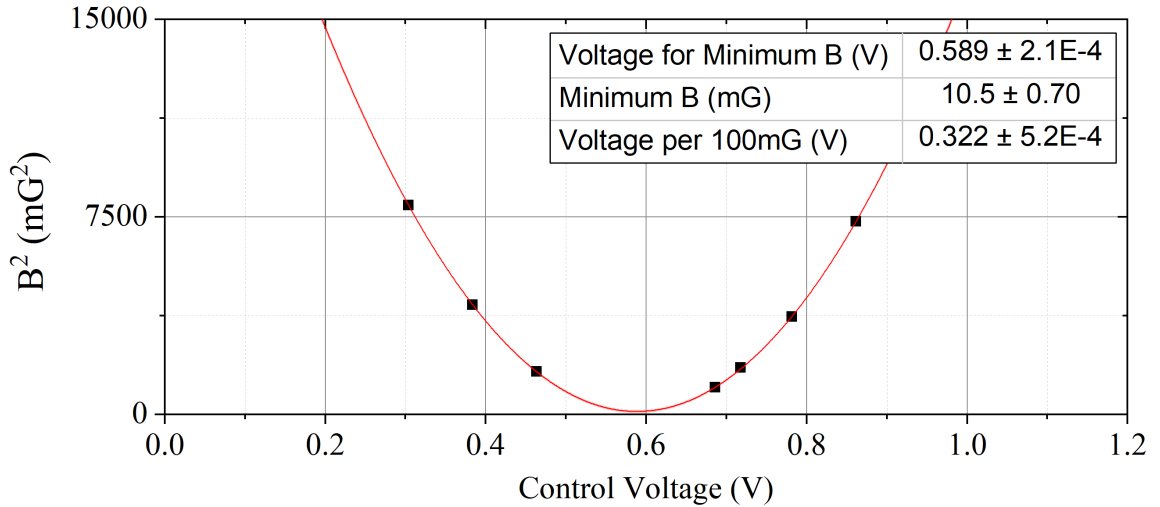


Figure 4.1: Measurement of the magnetic field squared as the trim field was scanned along the trim- y axis. The least squares fit (curve shown in red) gives the magnetic field parameters listed in the table.

4.1.2 Atoms as a Microwave Field Measure

The first verification of the microwave system involved a measurement of the quality of polarization transmitted into the chamber, at the location of the cold atom cloud. The atoms can be used to make a measurement analogous to Malus's law as a function of the angle between the microwave magnetic field direction (linear polarization in this case) compared to the bias field. These measurements are based on the ability to control the bias field direction to within 1° of arbitrary rotation for a bias field of 200 mG provided by the field calibration (above). A microwave transition is measured to determine a Rabi frequency by applying the resonant microwave field for incremental durations and measuring the state population transferred as a function of this time. The measured Rabi frequency of the π polarization clock transition is a function of the amplitude of the dot product between the bias field unit vector and the microwave field B vector, giving a $\propto |\sin(\theta)|$ dependence.

A measurement of this Malus's law angular dependence can be seen in Figure 4.2. This data was taken with a circular waveguide antenna (linearly polarized) positioned down the

imaging axis (x -axis) of the chamber. The field orientation ($|\mathbf{B}| = 200$ mG) was scanned until the bias vector directions corresponding to the minimum and maximum Rabi rates were determined to within 0.5° . Scanning the bias field in the plane containing these vectors traces out the highest contrast Malus's law curve. The cross product of these extremal vector field directions gives a vector $\hat{\mathbf{v}}$ about which to rotate the field

$$\hat{\mathbf{B}}_{min} \times \hat{\mathbf{B}}_{max} = \hat{\mathbf{v}}$$

where $\hat{\mathbf{B}}_{min}$ and $\hat{\mathbf{B}}_{max}$ are the unit vectors describing the directions of bias field for the minimum and maximum Rabi rates, respectively. Using this vector (normalized by $\hat{\mathbf{v}}' = \hat{\mathbf{v}}/|\hat{\mathbf{v}}|$), Rodrigues' rotation formula is applied to give a rotated bias field direction about this vector, $\hat{\mathbf{v}}'$, in the plane of highest contrast. Starting at $\hat{\mathbf{B}}_{min}$, the bias field is applied at an angle rotated about $\hat{\mathbf{v}}'$, and the Rabi rate is measured at each orientation. The reported data agrees very well with the expected form $\Omega_{max}|\sin(\theta)|$, where Ω_{max} is the maximum measured Rabi rate; see Figure 4.2.

The limitation of this measurement is related to the minimum Rabi rate measured. If the projection of π polarization is sufficiently small, the clock Rabi rate will be sufficiently slow that the measured data cannot be fit to determine a Rabi rate, and thereby it is difficult to determine the minimum Rabi rate. In this case, the contrast could be improved by applying higher microwave powers such that the maximum Rabi rate Ω_{max} would increase, but the minimum Rabi rate which could be determined would remain the same. The axial ratio of the microwave field can be determined from the measurement of the minimum and maximum Rabi rates since the Rabi rate is proportional to the microwave field projection along B_z .

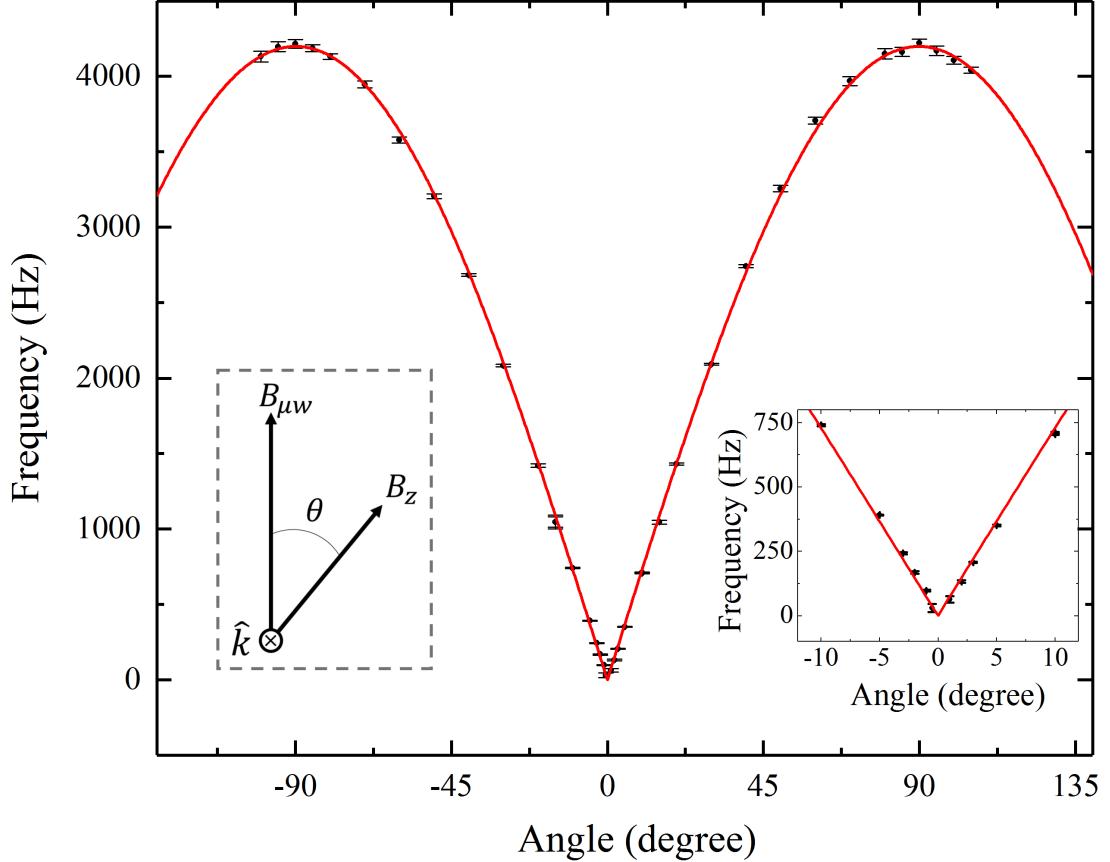


Figure 4.2: Malus’s law data measured using a linearly polarized, circular waveguide antenna, measured at angles between the field orientations of the minimum (0°) and maximum ($\pm 90^\circ$) Rabi rates. The inset on left indicates the angle θ between the microwave magnetic field direction ($B_{\mu w}$) and the bias field direction (B_z). The inset on right shows an expanded view around the minimum frequency. The smallest frequency which could be determined was 30 ± 20 Hz. The maximum frequency measured was 4220 ± 30 Hz.

4.1.3 Nulling the Field – Clock Transition

In order to use the circularly polarized field to select transitions, the microwave field and bias field need to be correctly aligned. It is necessary that the B_z projection of the circularly polarized microwaves be minimized along the bias field direction, otherwise the circularly polarized field will have a projection which can drive the transition of opposite handedness. We have developed a procedure to accomplish this by taking advantage of the orthogonal transition, the π -polarized clock transition, which acts through the microwave field projec-

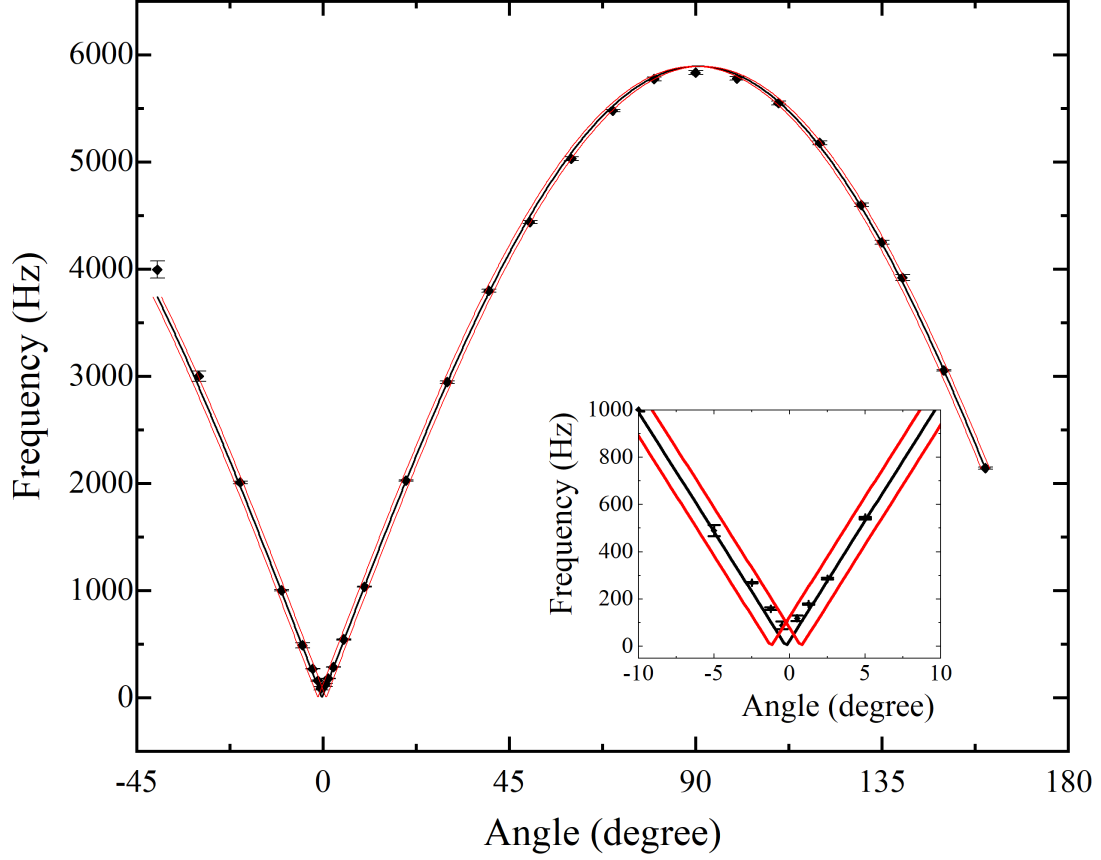


Figure 4.3: Data showing the dependence of the clock transition frequency vs the bias field offset angle. The 0° angle is set to be the minimum frequency. This data was taken with a 200 mG bias field. The black curve shows the best fit to the theory. The red curves show offsets of $\pm 1^\circ$ for comparison. The minimum reported Rabi rate was 90 ± 20 Hz.

tion onto the quantization axis (the bias field axis). When the bias field is oriented such that the atoms see the magnetic field circulating in the plane normal to this bias field direction, the π -polarized clock transition will not be excited. This can be seen from the discussion on the polarization basis vectors above, by examining Figure 3.4 at 0° . The Rabi rate for this transition is

$$\Omega_{clock} = \frac{\mu_B g_s B'}{2\hbar} |\sin(\theta)|$$

where θ is the angle between the plane containing the circulating microwave magnetic field and the bias field direction.

With the bias fields calibrated, a bias (e.g. 200 mG) is applied and the Rabi frequency

of the clock transition ($|1, 0\rangle \rightarrow |2, 0\rangle$) is measured. This measurement is a function of field direction and is simply repeated as the bias field direction is rotated until a minimum Rabi frequency is measured, with nearly no excitation to the $|2, 0\rangle$ state (1-2% of population after 3 ms of applied driving field). When the bias field is within a degree or so from the minimum, the Rabi frequency cannot easily be determined. At this point, the number of atoms excited to the $|2, 0\rangle$ state within the first several time steps of a Rabi cycle (up to about 1 ms) is used to compare nearby bias directions. The direction with the smallest excitation is selected. This procedure gives the correct alignment of the bias field for the circularly polarized microwave studies. Note, this procedure is referred to as “field nulling” throughout the text.

A measurement of this field nulling is shown in Figure 4.3. This figure again shows a Malus’ law curve similar to that in Figure 4.2. Here, Figure 4.3 shows a scan in only one angular coordinate, whereas the field nulling procedure should scan the full 4π angle of two angular coordinates (or half as each half contains one nulled-clock orientation). Indeed, the data taken in this figure required a prior measurement of the bias field orientations for the minimum and maximum Rabi rates, in order to determine the vector to rotate about to trace out the curve through the orientations of extremal Rabi rates (similarly as was done previously to measure Figure 4.2). In this measurement, the microwave field was produced by the circularly polarized helical antenna, compared to the linearly polarized circular waveguide antenna used in Figure 4.2. This has a similar form since the π transition is driven by a linear projection of the circularly polarized field. In this way, the π transition of the atoms acts like a linear analyzer.

After performing this procedure with the circularly polarized antenna, the bias field is set up for the circular polarization selective transitions. This means the bias field is oriented to be parallel with the k -vector of the microwave radiation, and with the bias field and antenna in this orientation, zero projection of the microwave field along the bias field means the clock transition will not be driven. The σ_{\pm} transitions will be driven purely by

the corresponding circular components of the driving field. Comparing this statement with Figure 3.4, the minimum π transition rate occurs at the maximum of one of the σ_{\pm} transitions. This is indeed the field alignment needed for the application of selective circularly polarized transition couplings! Any misalignment from this nulled-clock direction means the e_{\pm} fields will have a projection which drives the incorrect σ transition, as well as the π transition (see Figure 3.4 at intermediate angles, e.g. 20°).

It is interesting to note that an angular deviation was measured between the axis of the helical antenna and the direction of the nulled bias field, despite a high purity of circular polarization (quantified below). The helical antenna was aligned pointing towards that atoms with the antenna helix axis in the xy -plane (see Figure 2.4 for axis labeling convention in the experiment). Following this nulling procedure, the bias field was aligned with approximately a 50° deviation towards the z -axis. This unexpected field direction was potentially due to reflection or diffraction of the microwave radiation from nearby metal surfaces in the chamber. Nevertheless, the resulting field remained highly circularly polarized. Had this not been the case, that is, if the reflected or diffracted radiation had ruined the polarization, a couple options could be considered to mitigate this effect. Software such as COMSOL could be used to calculate the microwave field for the known antenna and chamber geometries. To narrow the microwave radiation pattern, a helical antenna with a greater number of turns would provide higher directivity of the microwave field. Otherwise, microwave absorbing materials (e.g. carbon-laden foam) could be used to absorb radiation that would otherwise be incident on nearby metal surfaces. In the case explored here, these measures were unnecessary.

4.2 Polarization Selection of σ -Transitions

Using the tools discussed up to now, a circularly polarized field is applied to the atoms. With the correct alignment of the bias field direction, this will selectively drive hyperfine transitions, while blocking the nearly degenerate transitions, of opposite σ_{\pm} polarization.

Therefore, the starting point for this experiment is the nulled-clock field alignment discussed above. At this point, the coupling strengths of magnetically sensitive transitions of different Δm_F are measured as Rabi rates. These Rabi rates are measured for both the σ_+ and the σ_- transitions. These rates are seen below in Figures 4.4 and 4.5. This process was then repeated with the direction of the bias field flipped. The rates for this case are seen below in Figures 4.6 and 4.7. The measured Rabi rates provide a measure of the coupling strength for each transition, where all of the transitions in these figures feature transition matrix elements of the same amplitude.

4.2.1 Larmor Decoherence – Fitting Slow Rabi Rates for Blocked Transitions

It is important to note that these σ_{\pm} transitions show significant decoherence after approximately 1 ms. This decoherence is a result of the inherent sensitivity of these transitions to the magnetic field. This Larmor decoherence is a limitation in determining the field ratio for sufficiently high degree of circular polarization (for sufficiently low axial ratios). This decoherence comes from variations in the accumulated Larmor phase, either from temporal fluctuations in bias field, or due to spatial inhomogeneity in the magnetic field or microwave field across the atoms. The polarization-blocked transitions show slow Rabi rates, which are measured for 1 ms or longer. The Rabi rates of the blocked transitions (e.g. Figures 4.5, 4.7) show the effect of this decoherence after 500 μs . In order to quantify the coupling strength of the blocked transitions, it was desirable to still determine a Rabi frequency, but using only measurements taken within the first 500 μs , before excess noise was accumulated from this Larmor decoherence. The Rabi rates for these slow transitions were therefore determined by fitting data within the first 500 μs and constraining the fit parameters to the expected values— a fixed amplitude of 1 and offset of 0 in fractional state population.

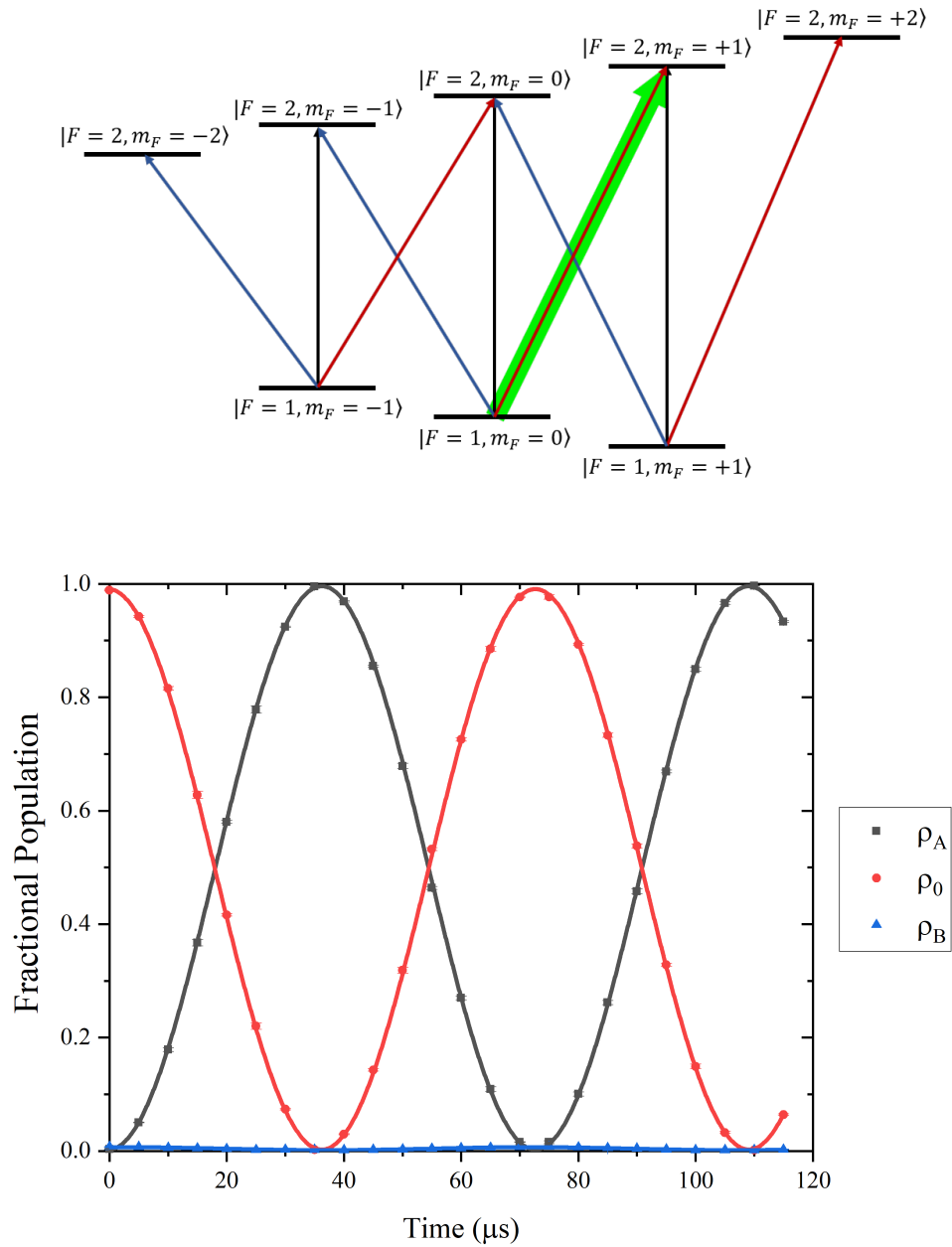


Figure 4.4: Fast, polarization selected σ_+ , Δ_+ transition: $|1, 0\rangle \rightarrow |2, +1\rangle$. (Top) The transition is highlighted in green. (Bottom) The measured Rabi cycle. The point markers show measured values (error bars show one standard deviation). The curve shows the least-squares fit. The best fit Rabi frequency in ρ_0 was 13717 ± 19 Hz

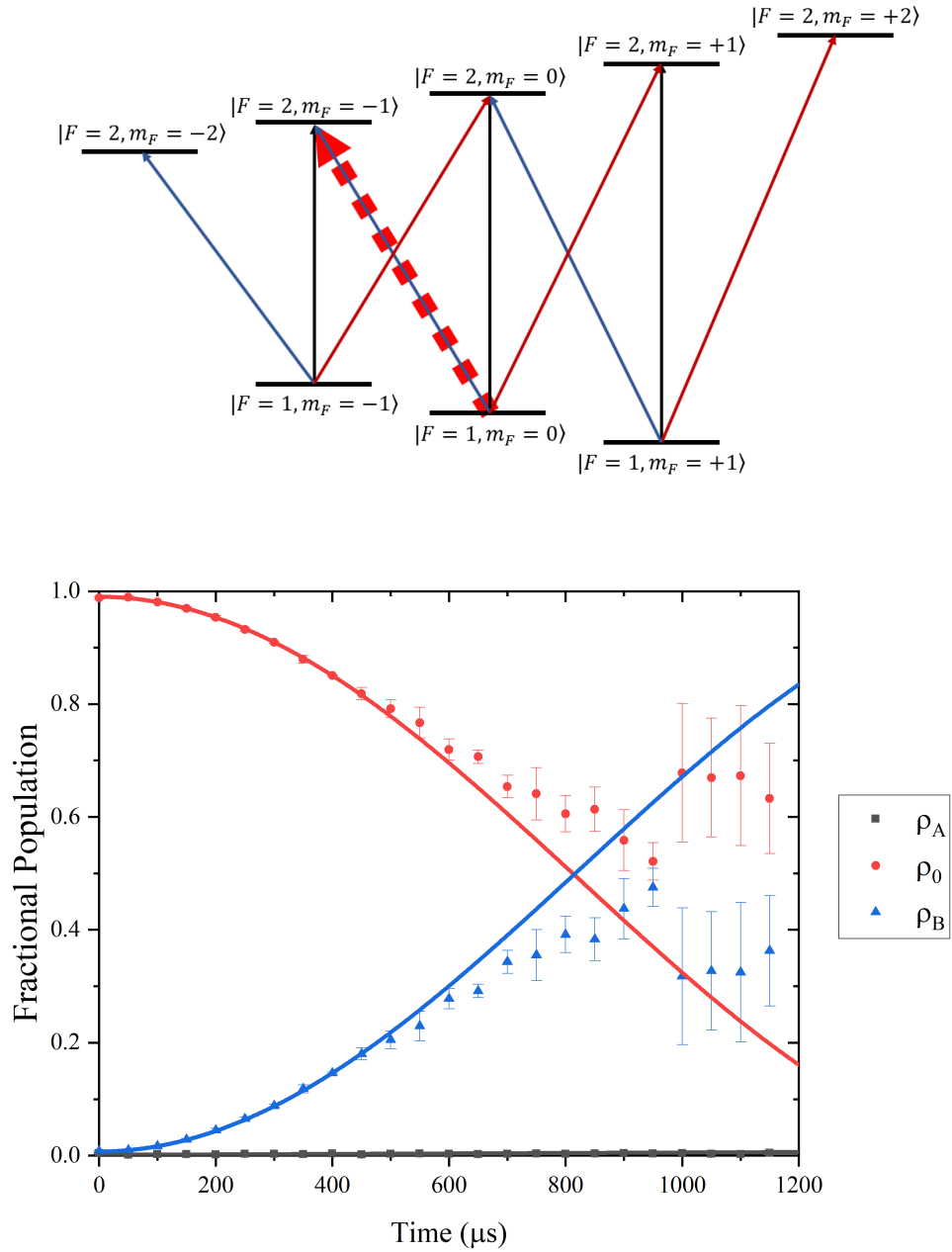


Figure 4.5: Slow, polarization blocked σ_- , Δ_- transition: $|1, 0\rangle \rightarrow |2, -1\rangle$. (Top) The transition is highlighted in dashed red. (Bottom) The point markers show measured values (error bars show one standard deviation). The curve shows the least-squares fit for the interval from 0 μs to 500 μs . The best fit Rabi frequency in ρ_0 was 303 ± 4 Hz

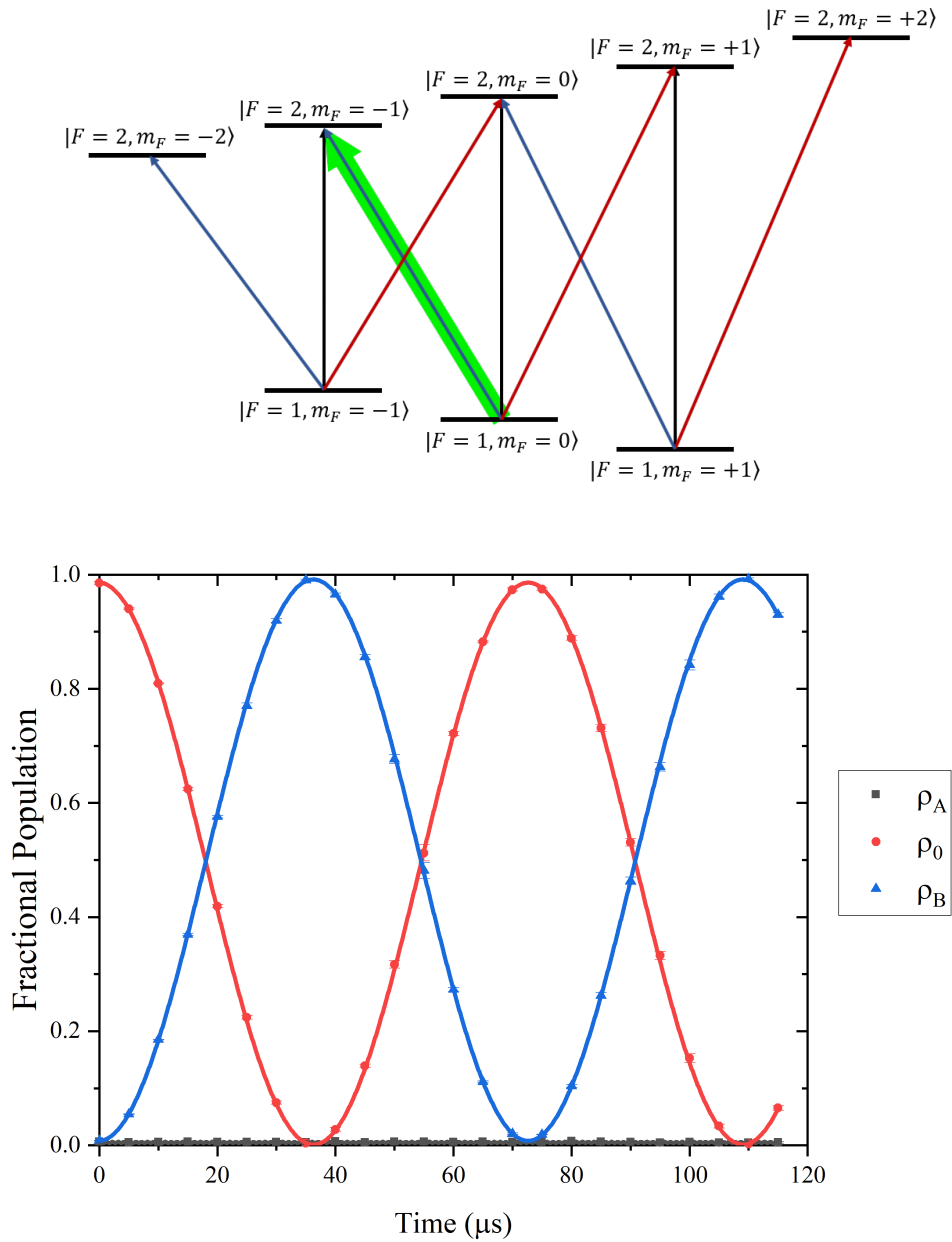


Figure 4.6: Fast, polarization selected σ_- , Δ_- transition: $|1, 0\rangle \rightarrow |2, -1\rangle$. (Top) The transition is highlighted in green. (Bottom) The point markers show measured values (error bars show one standard deviation). The best fit Rabi frequency in ρ_0 was 13717 ± 38 Hz

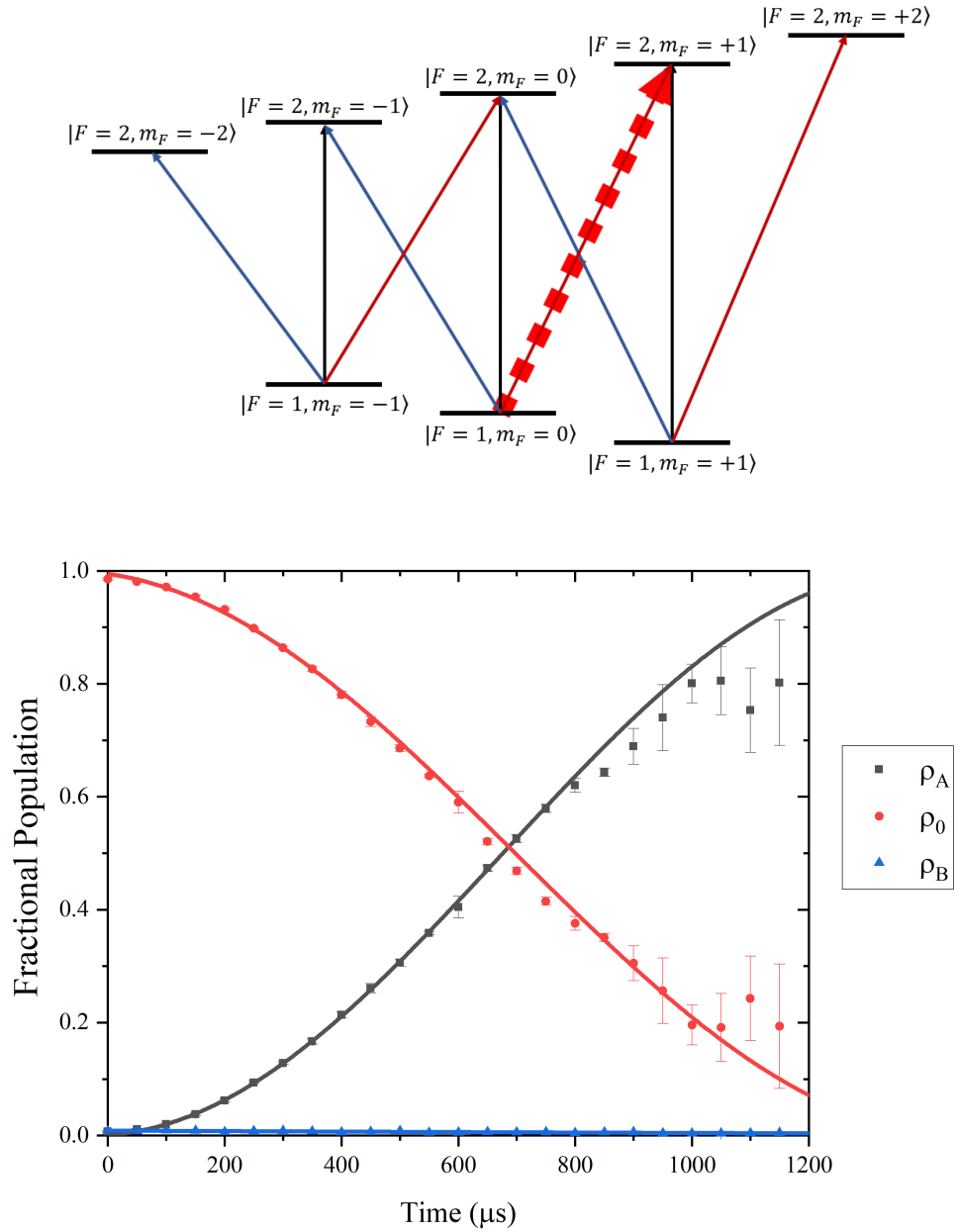


Figure 4.7: Slow, polarization blocked σ_+ , Δ_+ transition: $|1, 0\rangle \rightarrow |2, +1\rangle$. (Top) The transition is highlighted in dashed red. (Bottom) The point markers show measured values (error bars show one standard deviation). The curve shows the least-squares fit for the interval from 0 μs to 500 μs . The curve shows the least-squares fit. The best fit Rabi frequency in ρ_0 was 339 ± 6 Hz

Table 4.1: A tabulation of the Rabi frequencies measurements seen in Figures 4.4—4.7.

Frequencies for selective Rabi transitions:	
Polarization Selected σ_+ transition	13717 ± 19 Hz
Polarization Blocked σ_- transition	303 ± 4 Hz
Polarization Selected σ_- transition	13717 ± 38 Hz
Polarization Blocked σ_+ transition	339 ± 6 Hz

The measure of merit is the ratio of the microwave field amplitudes in each handedness of circular polarization determined through comparison of the Rabi rates for σ_+ and σ_- transitions, each scaled by the appropriate transition matrix element. We will call this ratio the *selectivity* provided by the microwave polarization. For the σ_{\pm} transitions starting in the $|1, 0\rangle$ state, as in Figures 4.4–4.7, the amplitudes of the matrix elements for the σ_+ and the σ_- transitions are equal. In this case, the selectivity is simply the ratio of the Rabi rates. In the general case, the Rabi rate for the transition between the between the $|i\rangle \rightarrow |f\rangle$ states is

$$\Omega_{i,f} = (1/2\hbar)\mu_B g_S B_p M_{IF,\{i,f\}} \quad (4.1)$$

where $M_{IF,\{i,f\}}$ is the transition matrix element corresponding to this transition, and B_p is the microwave field component of the associated polarization ($p = \sigma_+, \sigma_-, \pi$). Using measured values of $\Omega_{i,f}$ to determine B_p via Eqn. 4.1 for transitions of both σ_{\pm} , the ratio of B_{σ_+} and B_{σ_-} can be determined, i.e. the selectivity provided by the polarization of the microwave field is determined. With the antenna setup used in this work, we were able to demonstrate a selectivity of $(45.3 \pm 0.6)^{-1}$, calculated from the Rabi rates listed in Table 4.1 for polarization selected σ_+ and polarization blocked σ_- transitions. Similarly, a selectivity of $(40.5 \pm 0.7)^{-1}$ is calculated for polarization blocked σ_+ and polarization selected σ_- transitions. The slight difference in the slow Rabi rates could be a result of a difference in bias field stability at the opposite field orientations. Given this measured

selectivity, it is useful to estimate the populations transferred with a microwave π -pulse, i.e. the time require to transfer the maximum population via the polarization selected transition (e.g. $|1, 0\rangle$ to $|2, 1\rangle$ for the σ_+ selected transition). Let t_π be the π -pulse length for this selected transition. The maximum expected population transfer for the blocked transition can be inferred for the selectivity of $(45.3 \pm 0.6)^{-1}$, with the field on resonance with the blocked transition, as this gives the strength of the transition. At this time, the excited state population from the blocked transition is $|c_e(t_\pi)|^2 = 0.00120(3)$ for the maximum selectivity measured here.

Additionally, the ratio of these field amplitudes provides a measure of the axial ratio of the microwave field. The axial ratio in terms of the field amplitudes is given as [117]

$$r = \frac{B_{\sigma_+} + B_{\sigma_-}}{B_{\sigma_+} - B_{\sigma_-}} \quad (4.2)$$

The axial ratio is commonly stated in decibels, which is calculated by

$$r_{[dB]} = 20 \text{Log}_{10} \left| \frac{B_{\sigma_+} + B_{\sigma_-}}{B_{\sigma_+} - B_{\sigma_-}} \right| \quad (4.3)$$

The measured selectivity of $(45.3 \pm 0.6)^{-1}$ gives an axial ratio of the circularly polarized microwave field to be 1.045, or equivalently 0.38 dB. This axial ratio represents the primary limitation in selecting one transition compared to another degenerate in frequency using circularly polarized microwaves.

4.2.2 Angular Dependence of Bias Field

The angular dependence of the σ_\pm and π transition coupling strengths for a circularly polarized microwave field was derived in Chapter 3, and the result is repeated here in Figure 4.8. To characterize this dependence in the experiment with the circularly polarized microwave field, the bias field direction was intentionally varied through a range of angles, and the Rabi rates of both the σ_+ and σ_- transitions were measured. These Rabi rate measure-

ments vs the angles of deviation in bias field are displayed in Figure 4.9, to be compared Figure 4.8. This data and the theory are seen to agree remarkably well. However, the σ_+ transition saturates at low Rabi frequencies near 0° . This is a combination of limitations from the least-squares fits to the slow Rabi cycle data and residual coupling via the opposite field handedness from the ellipticity of the polarization. The ratio of the Rabi rates at 0° has a value of $1/43$ and is consistent with the measured selectivity for the microwave polarization, implying the saturation is primarily due to the latter.

There are several insights to be gained from these figures. Firstly, inspecting the sensitivity around 0° in Figure 4.8: there is a first order (linear) dependence on the angle for the π transition, but the σ_\pm transitions are only second-order (quadratically) sensitive to the angle. The form of these two sensitivities to field angle make the clock transition (the π transition) an excellent tool for the field nulling procedure, since near the null-point of the clock transition, the clock transition Rabi frequency is approaching zero linearly with the angle. Similarly, once the angle is near the null-point, the σ_\pm transitions are more robust to the field deviations, as their small-angle response is quadratic. Secondly, as can be seen in Figure 4.8, the selected σ_\pm transition flips each π rotation, or each 180° flip of the bias field. This must be true since this represents a reversal of the direction of magnetic field circulation relative to the bias field direction at the atoms. This field reversal was used to study both the cases where σ_+ and σ_- transitions are selected.

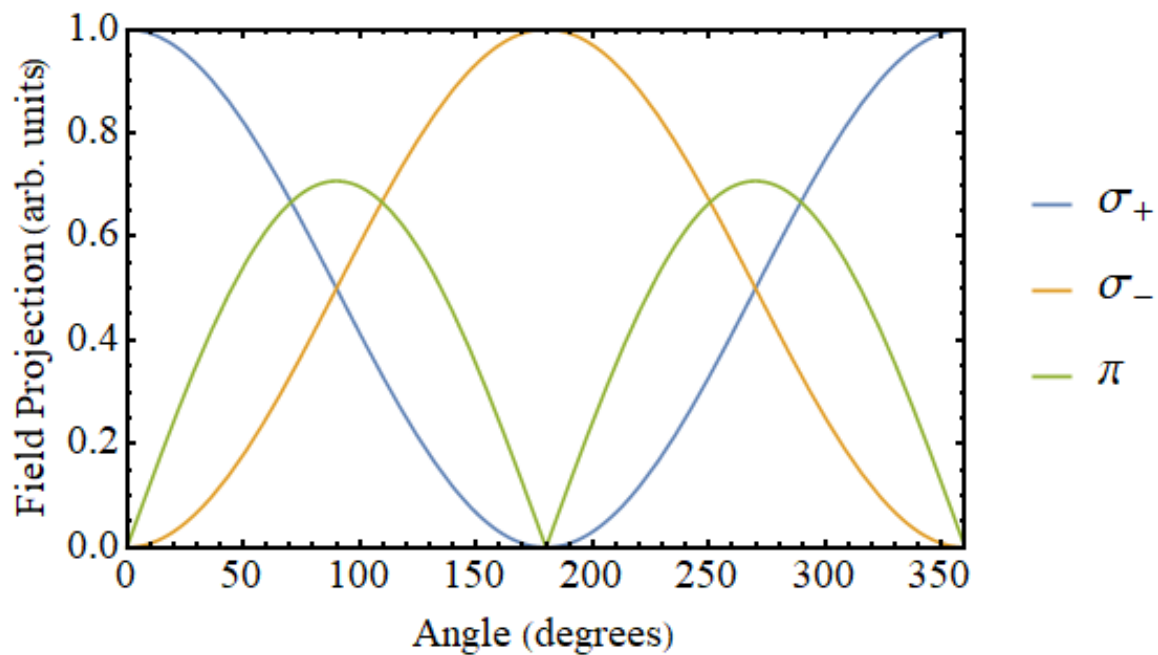


Figure 4.8: (*duplicate*) The angular dependence of the σ_{\pm} and π transitions compared to the field direction. The curves show the amplitude of the e_+ microwave field projected into the atomic basis as the field is rotated about the x -axis.

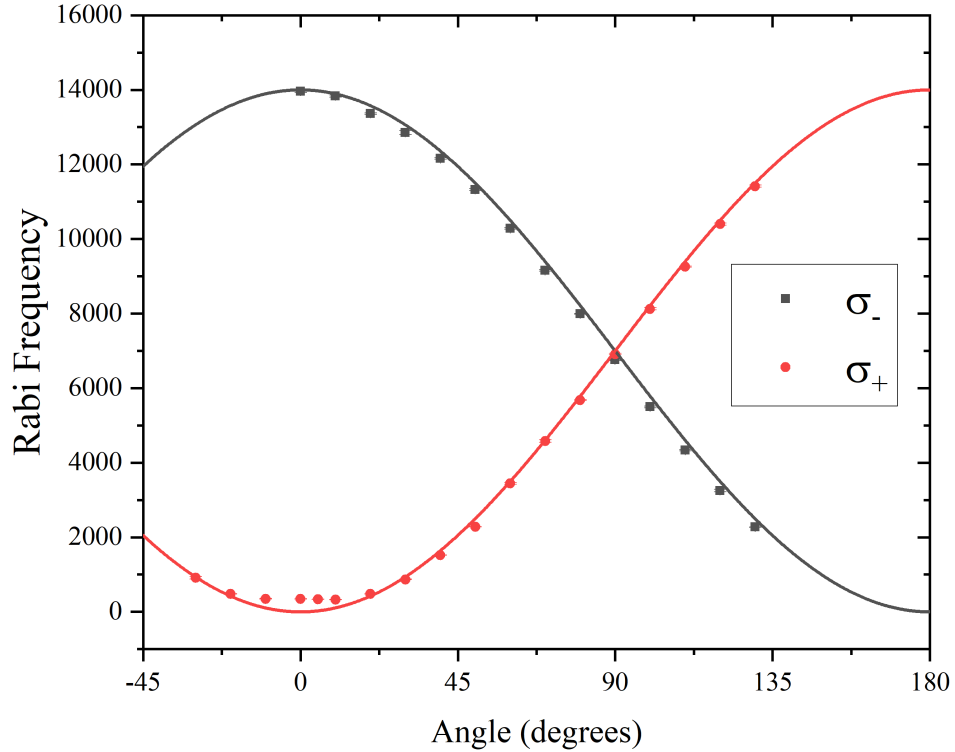


Figure 4.9: The angular dependence of the σ_{\pm} transition on the field direction (c.f Figure 4.8). The markers show the measured Rabi rates with error bars of one standard deviation (error bars smaller than the point markers). At 0° , ratio of Rabi rates is $1/43$. The curves show the theory with the amplitude set by the maximum measured Rabi frequency and 0° set by the bias field alignment from the field-nulling procedure.

4.3 All-Microwave Λ Transitions

This section describes an application of the circularly polarized field for a three-level Λ transition. This Λ transition is driven in the presence of a degenerate transition with a different sign of σ_{\pm} , where the circular polarization of the microwave blocks the unwanted transition, allowing for a successful transition. The Λ transition is a two-photon process which can be used to couple two base states via a third excited state. In the ^{87}Rb ground

state hyperfine levels, this allows transitions between two adjacent $|1, m_F\rangle$ states, where the degeneracy in the m_F level spacings (Δ) prevents closed two-level couplings within $F = 1$ via a one-photon transition. The Λ configuration is highlighted within the ^{87}Rb hyperfine levels in Figure 4.10.

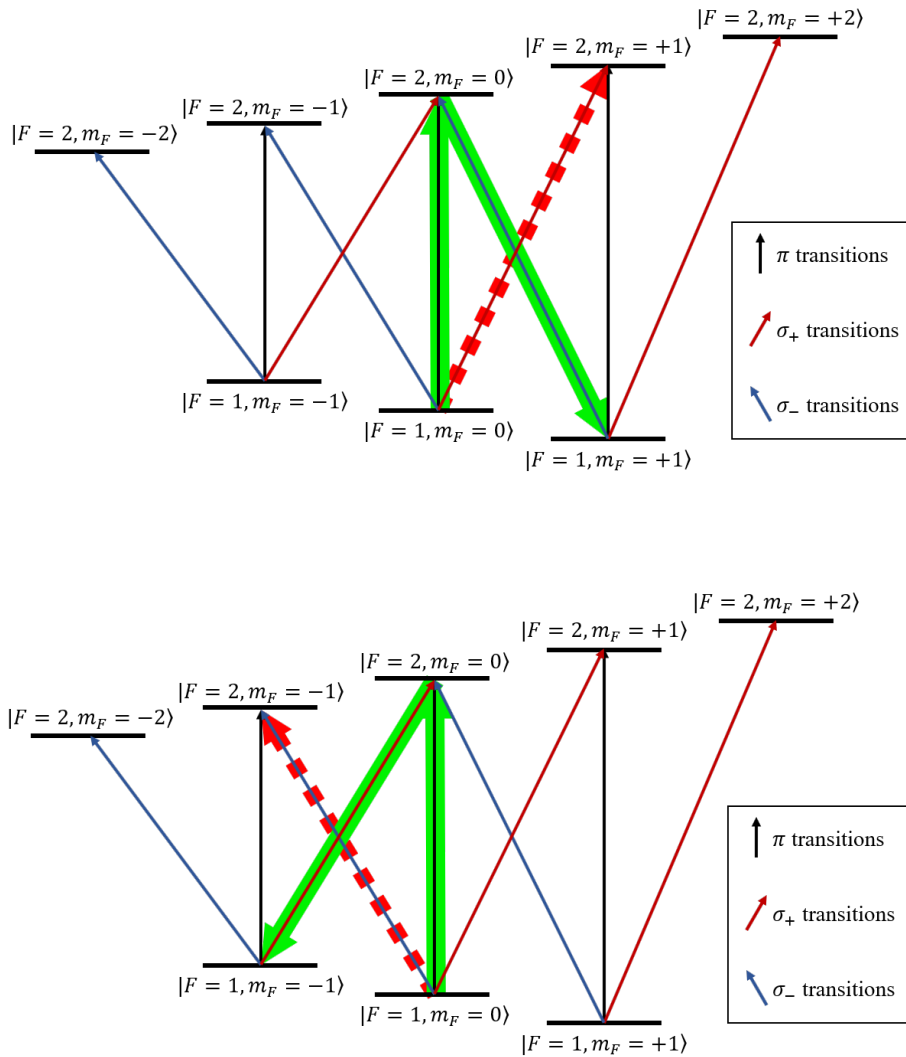


Figure 4.10: Energy level diagram highlighting (in green) the couplings for a $\Delta m_F = +1$ (top) and a $\Delta m_F = -1$ (bottom) Λ transition. The frequency degenerate (unwanted) transition is highlighted in thick, dashed red.

4.3.1 Λ Transition – Simulations

Simulations were computed to demonstrate the state evolution due to Λ transformation. These simulations are numerical integrations of the time evolution under the interaction picture Hamiltonian, Eqn. 3.14, with the Λ fields. Simulations were run and are presented below for cases with selective microwave transitions (circularly polarized) and non-selective transitions (linear polarization or mis-aligned circular polarization cases) with a couple cases for the undesired coupling strength. The small coupling is introduced by scaling the field amplitude for the corresponding (unwanted) polarization state. ¹

¹These simulations show the populations as we measure them in the experiment. That is, the top figure is analogous to a measurement with the repump light on where the $F = 1$ and $F = 2$ levels are measured together. The bottom figure shows only the population in $F = 2$. This measurement is described in Chapter 2.

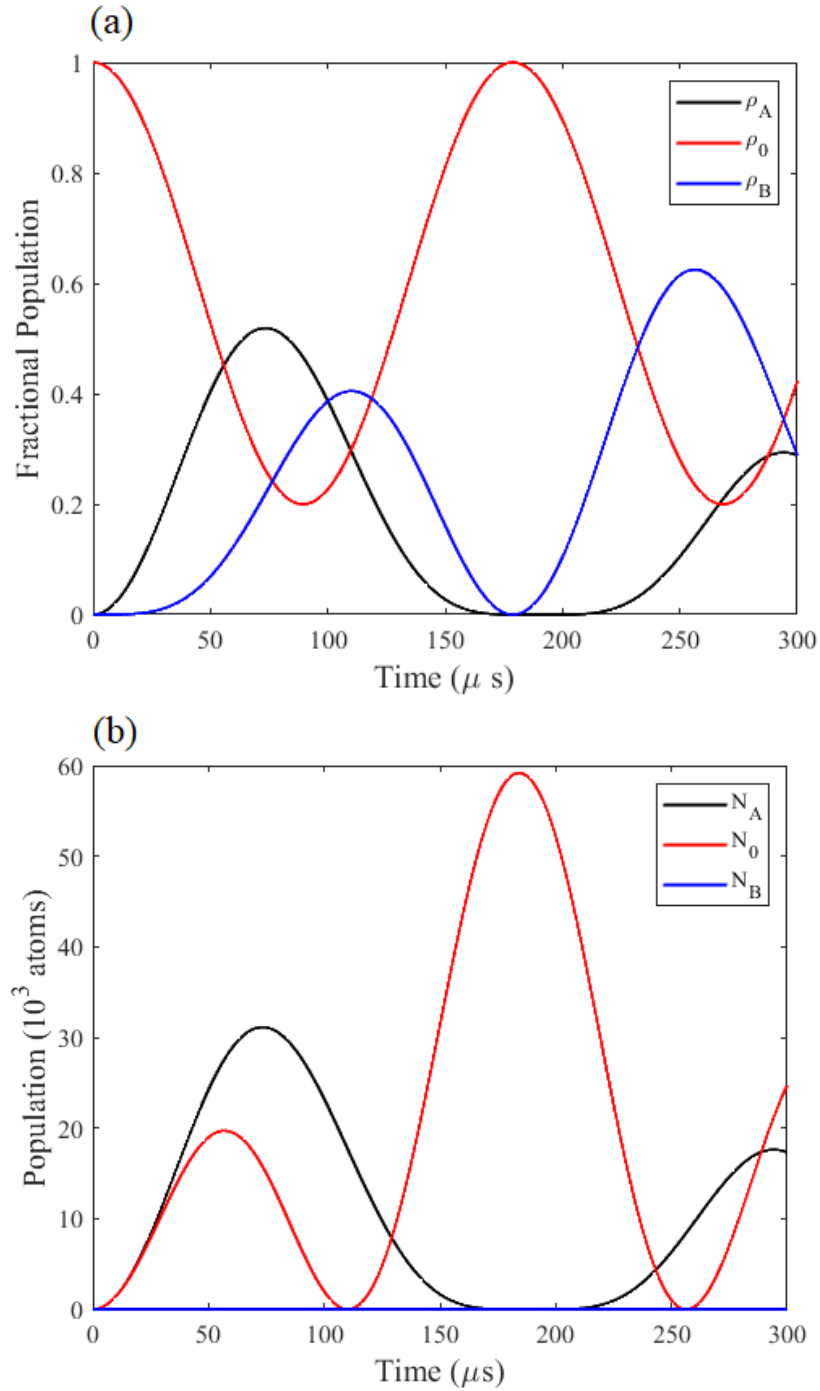


Figure 4.11: A simulation of the populations when the Λ transition is driven without the polarization selectivity. (a) shows the measure of all the populations, the $F = 1$ and the $F = 2$ states, as fractions of the total number of atoms. (b) shows only the number of atoms in the $F = 2$ states.

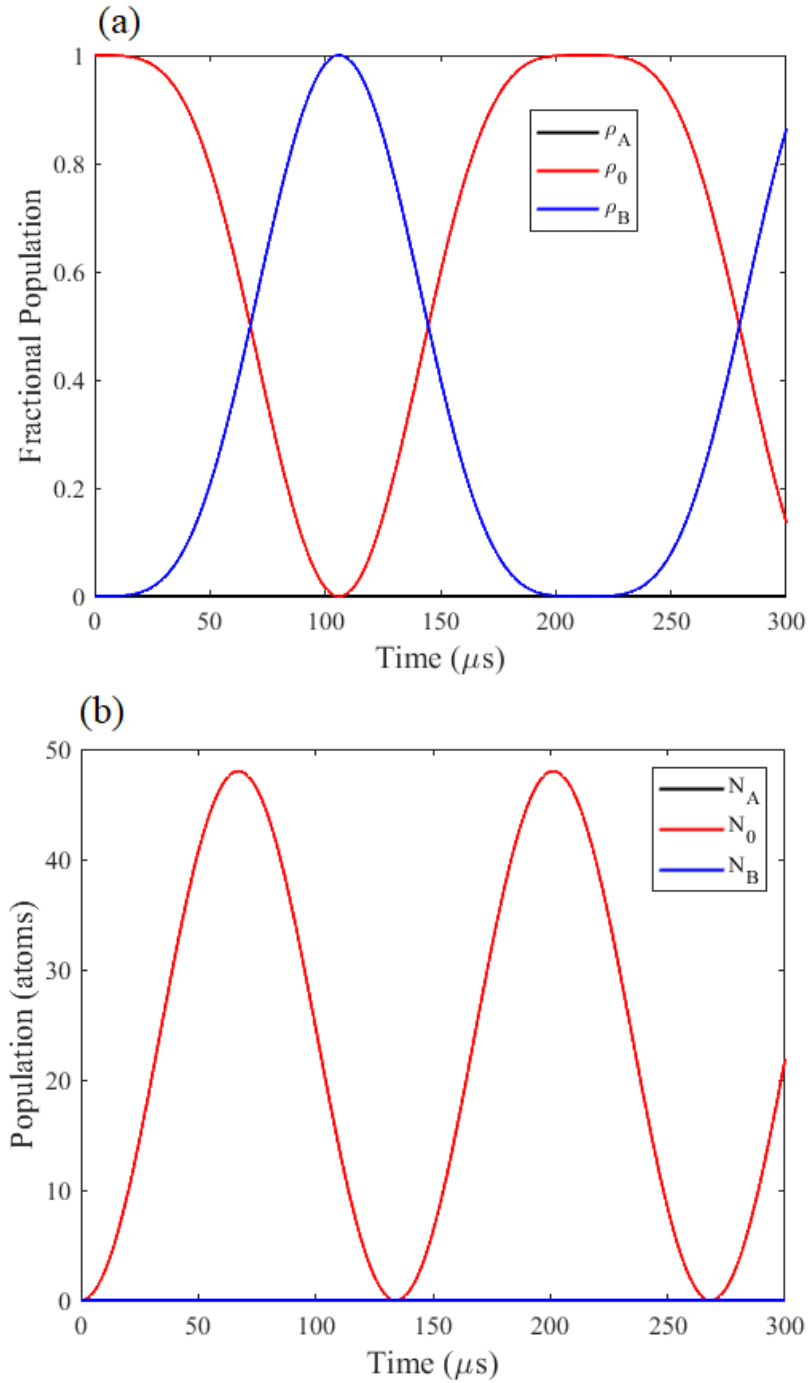


Figure 4.12: A simulation of the polarization-selective Λ transition. (a) shows the measure of all the populations, the $F = 1$ and the $F = 2$ states, as fractions of the total number of atoms. (b) shows only the number of atoms in the $F = 2$ states.

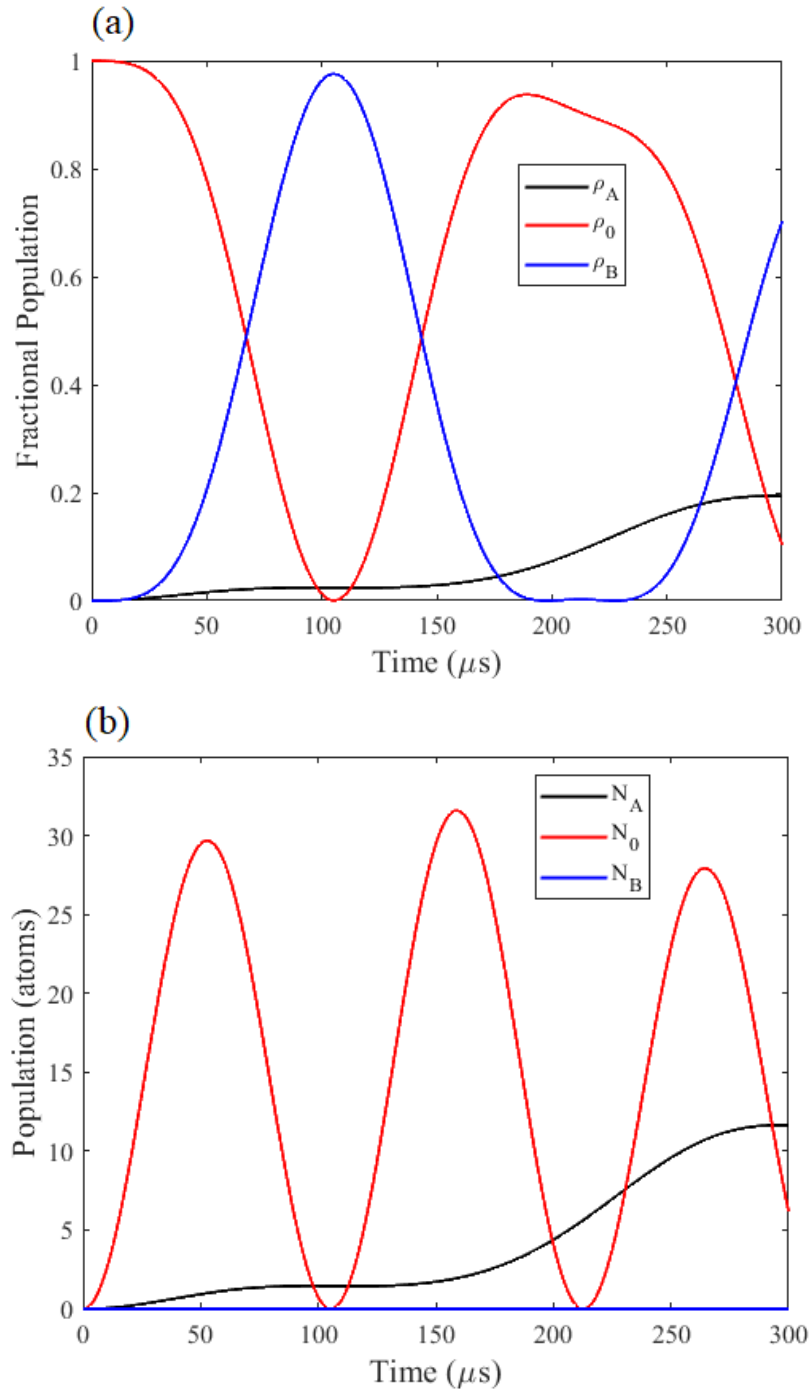


Figure 4.13: A simulation of the polarization-selective Λ transition, in the case of an elliptical polarization showing a small coupling to $|2, 1\rangle$, an undesired level for the Λ transition. The undesired coupling is set for a selectivity of $1/7$. (a) shows the measure of all the populations, the $F = 1$ and the $F = 2$ states, as fractions of the total number of atoms. (b) shows only the number of atoms in the $F = 2$ states.

For the case without the polarization selection, Figure 4.11, there is undesirable excitation to a state outside of the Λ manifold, which is due to the degeneracy in frequency of this transition—the population in $|2, +1\rangle$ represents the undesired population transfer (see Figure 4.10, red dashed transition). At approximately $80 \mu\text{s}$ (see Figure 4.11), the population is in a superposition of four states ($|1, 0\rangle$, $|2, 0\rangle$, $|1, +1\rangle$, and $|2, +1\rangle$). In this case, the simulated microwave parameters were set to match the experimental data for a non-selective Λ transition (discussed below, Figure 4.16). In contrast, the polarization selective case, Figure 4.12, demonstrates a successful total population transfer to the $|1, +1\rangle$ state through the mediating state $|2, 0\rangle$. Then, a short while later, the population returns to the initial state $|2, 0\rangle$. This shows a successful Λ transition with coherent two-photon Rabi flopping. For the intermediate case, the microwave has a small component driving the σ_+ transition along with the selected σ_- transition of the Λ transition, here with a selectivity of $1/7$. This simulation is seen in Figure 4.13. It is observed that the population in the undesired state slowly increases as a result of the undesired driving. In the experiment, this situation can occur if the microwave is elliptically polarized, or if the direction of propagation of the microwave is misaligned with the bias field. Nevertheless, from these simulations it is clear to see the difference between a successful Λ transformation and one that fails due to degeneracies. The metric for success is the transfer of the population back-and-forth between the states $|1, 0\rangle$ and $|1, \pm 1\rangle$. The percentage of population transferred will be the reported fidelity in the experimental results which follow.

4.4 Λ Transition – Experiment

To implement the Λ transition in the experiment, an additional antenna is used to drive the second leg of the Λ transition. Starting in the $|1, 0\rangle$ state, a π polarized field is needed for one of the legs of the Λ (see Figure 4.10), and this is the transition that is nulled in the alignment of the circularly polarized antenna. This second antenna (linearly polarized) is introduced at an angle to the bias field direction to drive the π polarized clock transition;

the exact alignment of the polarization is not critical in this case. A log-periodic antenna was used since the quality of the linear polarization is not a concern in this case and this antenna has a convenient small form factor. Each antenna (the circularly polarized, helical antenna and the linearly polarized log-periodic antenna) is controlled with an independent microwave circuit and amplifier. The Λ transition is driven by simultaneously applying fields from both antennas, each at the correct frequency for each to drive one leg of the Λ . The synchronization is achieved by simultaneously triggering on (and later off) the TTL-controlled rf switch in each microwave circuit.

Rabi Rates for Λ Transition

In order to fully transfer the population from the $|1, 0\rangle$ state to the $|1, -1\rangle$ state, the Rabi rates of both legs of the Λ transition need to match (the same is true for the $|1, 0\rangle$ and $|1, +1\rangle$ states). Consequently, the Rabi rates of both sides of the Λ transition need to be determined, and adjusted accordingly. Determining the clock transition Rabi rate is a standard practice—it is measured by turning off the repump light and measuring the number of atoms in the $F = 2$ state as a function of time. The Rabi rate of the σ_{\pm} leg of the Λ is measured in two ways, via a direct or an indirect measurement. For the direct measurement, a resonant π -pulse of the clock transition is applied which transfers the population to the $|2, 0\rangle$ state. Immediately following this π -pulse, the σ_+ (Δ_-) field is applied in incremental pulse lengths and the Rabi cycle between $|2, 0\rangle \rightarrow |1, -1\rangle$ is measured. The indirect measurement is performed via the measurement of the σ_+ transition from the $|1, 0\rangle \rightarrow |2, +1\rangle$ state (Δ_+). The Rabi rate for this transition is measured as usual for a two-level microwave transition as both populations can be measured separately via Stern-Gerlach separation with the relative population measured as a function of pulse length. Then by comparison of the microwave matrix elements for these two σ_+ transitions, it is seen that the σ_+ (Δ_-) transition for the Λ has a Rabi frequency of $(\sqrt{1/8})/(\sqrt{3/8}) = 1/\sqrt{3}$ times the value measured for the σ_+ (Δ_+) transition. The Rabi rate for the σ_+ (Δ_-) transition is this factor

times the Rabi rate for the σ_+ (Δ_+) transition. Measurements of the relevant Rabi rates are shown in Figure 4.14. Using these measurements, the Rabi rates for the two Λ legs are compared while iteratively adjusting the microwave power of either antenna circuit until the rates match.

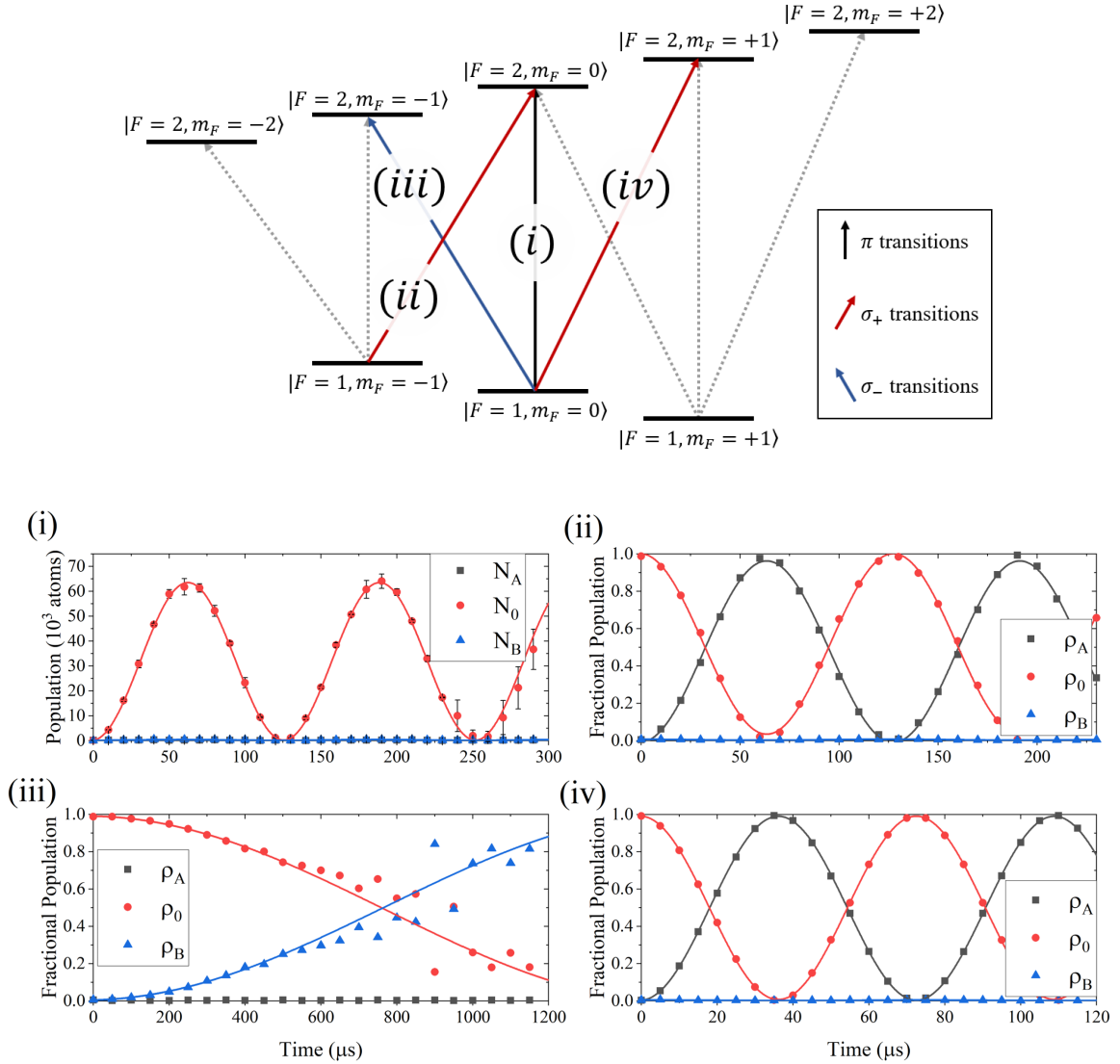


Figure 4.14: The Rabi rates related to the Λ transition. (a) The level structure, indicating which transition corresponds to which Rabi rate below. (i) One of the two Λ legs—the clock Rabi rate. This is a π transition. The measured Rabi frequency was 7923 ± 13 Hz (ii) One of the two Λ legs—the σ_+ , Δ_- transition. The measured Rabi frequency was 7824 ± 24 Hz. (iii) This transition would be degenerate to the Λ transitions. This transition is only weakly driven as seen by the very slow Rabi rate. This is a consequence of the circular polarization of the microwave field, allowing a successful Λ transition. The measured Rabi frequency was 316 ± 13 Hz. (iv) Another selected σ_+ transition (Δ_+). This transition can be measured to determine the Rabi rate for (ii), using a ratio of the transition matrix elements. The measured Rabi frequency was 13736 ± 38 Hz.

Driving the Λ Transition

To transfer the population from the $|1, 0\rangle$ state to the $|1, -1\rangle$ state, we apply the two microwave fields for the Λ transition, both the π polarized clock microwave ($\delta = 0$) and the σ_+ polarized ($\delta = \Delta_-$) transition. Since the Λ transition requires the selectivity of the σ_+ polarized microwave, the field nulling procedure for the helical antenna is again the starting point followed by the Rabi rate balancing. Then, the Λ transition with matching Rabi rates is measured as a single-photon Rabi rate would be, only with two microwave fields instead of one. A measurement of such a Λ transition can be seen in Figure 4.15. The data measured agrees quite well with the theory, Figure 4.12. With the σ polarization selectivity, the three-level Λ system is well resolved and the $|1, -1\rangle$ state is successfully populated. The population oscillates between the $|1, 0\rangle$ and $|1, -1\rangle$ states, with only a small percentage of leakage to the $|2, -1\rangle$ state. This leakage is due to the ellipticity of the microwave radiation.

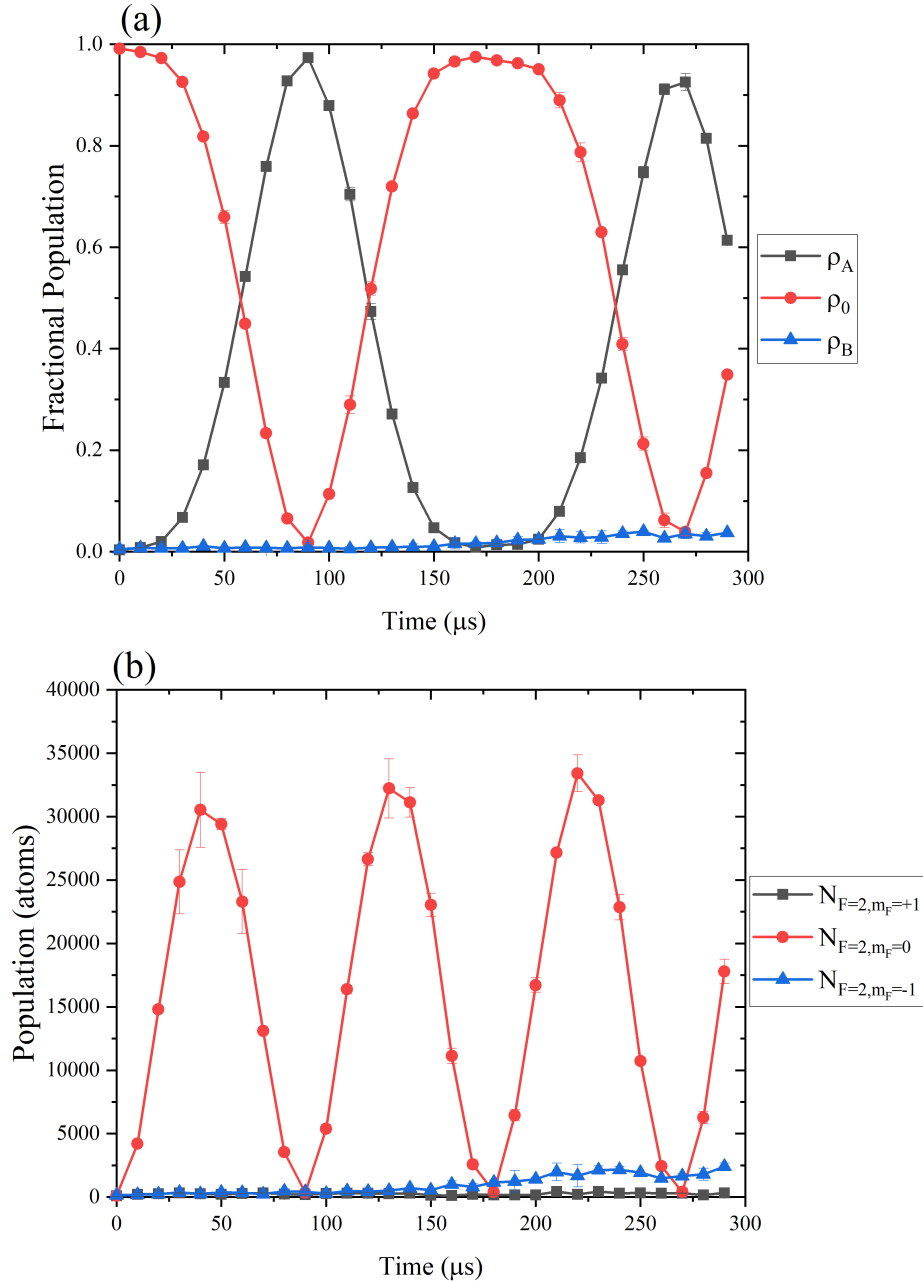


Figure 4.15: A Λ transition using the circular polarized microwave field to select only the desired level couplings. (a) shows the measure of all the populations, the $F = 1$ and the $F = 2$ states, as fractions of the total number of atoms. (b) shows only the number of atoms in the $F = 2$ states.

This successful Λ transition is to be contrasted with the case where the Δ transitions are not selected via the polarization of the microwave, see Figure 4.16. In this non-selective

case, state is unsuccessfully transferred to the $|1, -1\rangle$ state. This measurement was made by rotating the bias field to prevent the polarization selection. The non-selective result is also seen to agree well with the theory prediction, Figure 4.11. Clearly, the selectivity provided by the methods described herein are effective in realizing in such an all-microwave Λ transition.

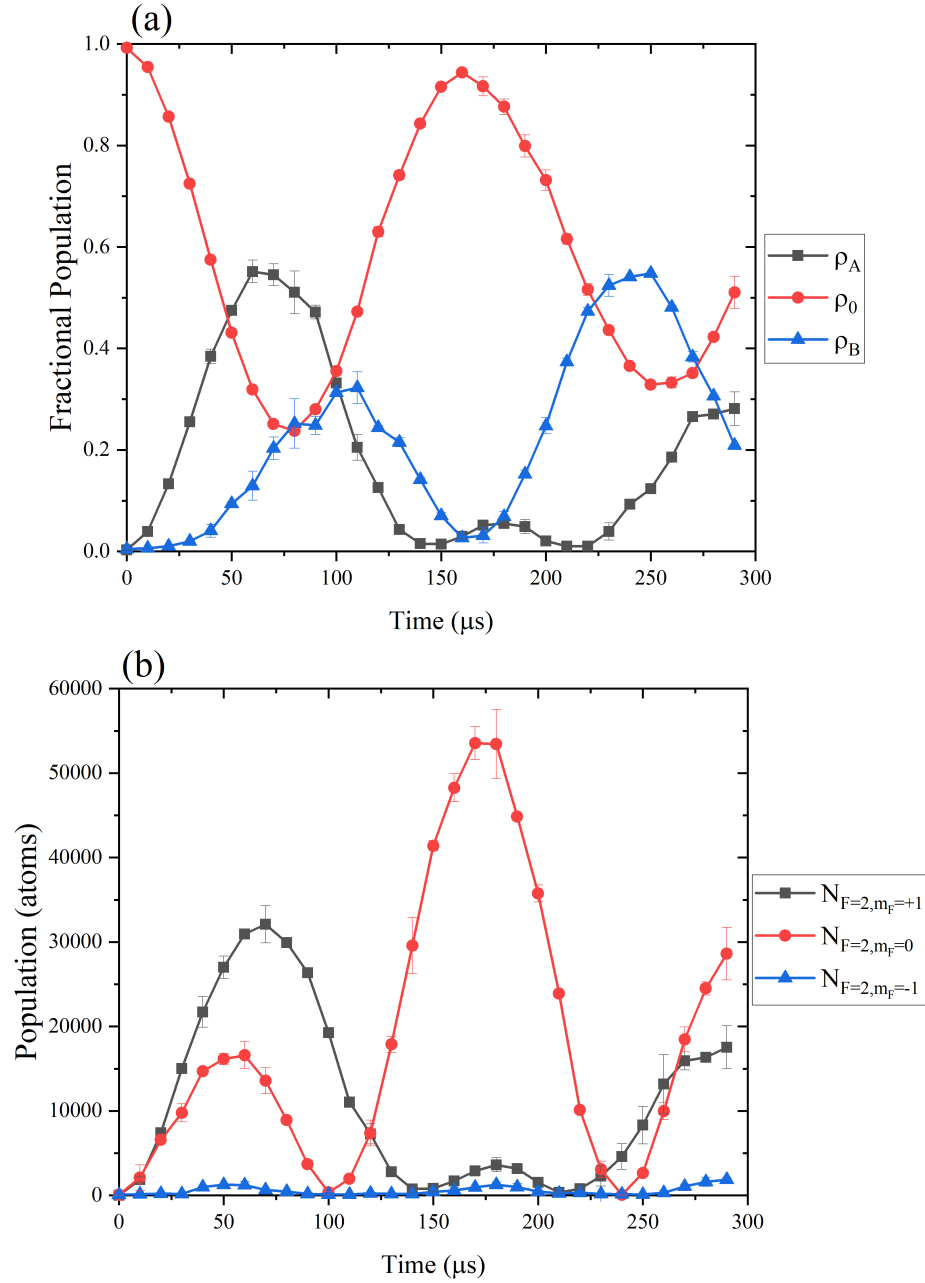


Figure 4.16: An attempted Λ transition without the selectivity of the circularly polarized microwave field. (a) shows the measure of all the populations, the $F = 1$ and the $F = 2$ states, as fractions of the total number of atoms. (b) shows only the number of atoms in the $F = 2$ states.

Benchmarking the Λ Transition

As seen above, the all-microwave Λ transition was qualitatively successful using the circular polarization selection; this section quantifies the fidelity of this transition. For a quantitative comparison, a two-level σ_+ , Δ_+ transition ($|1, 0\rangle \rightarrow |2, +1\rangle$) was measured with fine time steps around the π -pulse and 2π -pulse times. This data can be seen in Figure 4.17. The result was a maximum measured population transfer of 99.5% at the π -pulse time ($\approx 102 \mu\text{s}$), and 99.1% at the 2π -pulse time ($\approx 205 \mu\text{s}$).

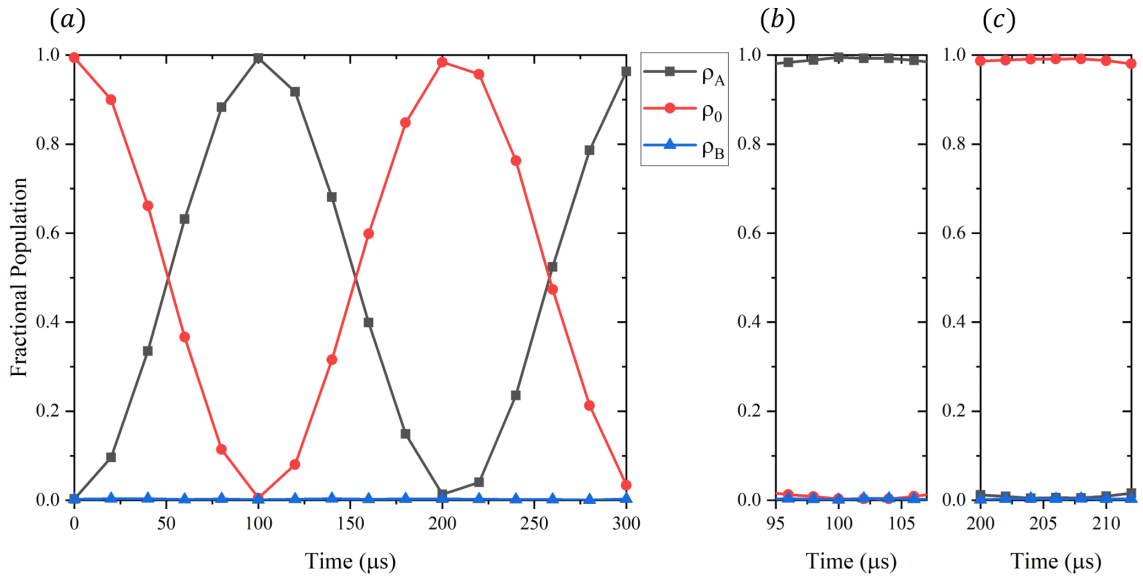


Figure 4.17: A two-level Δ_+ transition measured to show the fidelity and level of noise in such a measurement; to compare with the optimized Λ transition (Figure 4.18). (a) shows the full Rabi cycle (b) shows a finer scan around the π -pulse time of maximum transfer to the $|2, +1\rangle$ state. There was a transfer of 99.5% of the population to this state. (c) shows the 2π -pulse time when population returned to the $|1, 0\rangle$ state, where 99.1% of the population returns to this state.

Following this, a the Λ transition was measured with fine time steps around the time of maximum population transfer to the $|1, -1\rangle$ state and also the time of its return to the $|1, 0\rangle$ state. With the Λ transition functional, the parameters of the driving fields were

finely scanned around the expected values for the Λ transition; tuning the frequency of the Δ_- transition and the Rabi rate, via the microwave power, for each leg of the Λ . The optimized Λ transition is shown in Figure 4.18. As seen in this figure, the Λ fidelity reaches 99.5% population transfer to the $|1, -1\rangle$ state (at $\approx 88 \mu\text{s}$). This is equivalent to the limit measured in the two-level Rabi transition, implying this population transfer is not limited by the quality of the circular polarization. The resulting error is quite small, 0.5%. Further, there was $< 0.1\%$ population measured in the blocked σ_- transition at this time. By these measures, the Λ transition was highly successful. The population return to the $|1, 0\rangle$ state (98.8%) is slightly worse than that of the two-level transition. This is a result of slow population transfer via the blocked σ transition. This leakage is due to the slight ellipticity of the microwave field (measured as a selectivity of $(45.3 \pm 0.6)^{-1}$), resulting in 0.7% population transferred to the $|2, -1\rangle$ state (at $\approx 167 \mu\text{s}$).

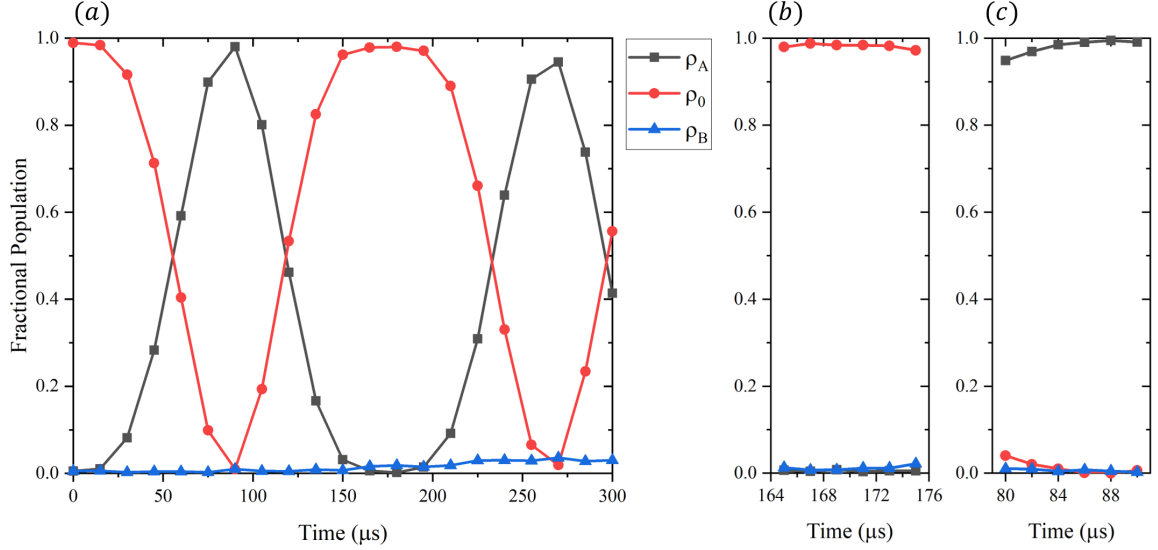


Figure 4.18: An optimized Λ transition using the circularly polarized field. This transition is a measure of the fidelity of the all-microwave Λ transformation. Here, the angle of the bias field, and the powers and frequencies of the microwave fields were scanned around the expected values. The result was a Λ transition with 99.5% fidelity. (a) shows the full Λ transition Rabi cycle. (b) shows a finer scan around the time of maximum transfer to the $|1, -1\rangle$ state. There was a transfer of 99.5% of the population to this state. (c) shows the population revival in the $|2, 0\rangle$ state, where 98.8% of the population returns to this state.

4.4.1 Holonomic, Non-Adiabatic Gate

A Λ transition of this type is the basis of a holonomic, non-adiabatic gate [67, 68], of interest in holonomic quantum computing [69]. Holonomic refers to the accumulation of a geometric phase from the transformation, rather than a dynamical phase. This transition is non-adiabatic since there is excitation to the excited state. Adiabatic gates have been demonstrated using optical transitions [75], where the state must be made to evolve in a dark state of the driving fields. A non-adiabatic gate has not been demonstrated in the hyperfine levels up to this point. The non-adiabatic nature of this microwave-based Λ transition can be used as an advantage for measurement of non-standard expectation values, since the population in the upper hyperfine state ($F = 2$) can be measured.

4.5 Low Field Microwave Transitions

4.5.1 Low Field Simulations

The circularly polarized microwave can be used to successfully drive individual σ transitions at low fields. Simulations with these low fields show the comparison between the circular-polarization selective transition Figure 4.19(a), and the non-selective transition Figure 4.19(b). These simulations are for the parameters measured in the experiment (Rabi rates and number of atoms), to be compared with measured data below. It is clear that the polarization selective case successfully drives a single hyperfine transition (here $|1, 0\rangle \rightarrow |2, -1\rangle$), whereas the non-selective case couples the $|1, 0\rangle$ state to three $F = 2, m_F = -1, 0, +1$ states. The difference in the hyperfine couplings between the polarization-selective case and non-selective case demonstrates the utility of the circularly polarized microwaves at low fields. Additionally, these simulations show that the circularly polarized microwaves could be used to selectively drive individual transitions more rapidly than otherwise possible, such that the Fourier linewidth of the microwave is as large as the level spacings—the simulations shown here are exactly this case for a 15 mG bias field. Typically at such low fields, a very slow Rabi rate (low microwave power) is used in order to narrow the microwave linewidth and resolve the transitions, whereas this is not necessary in the circular polarization selective case.

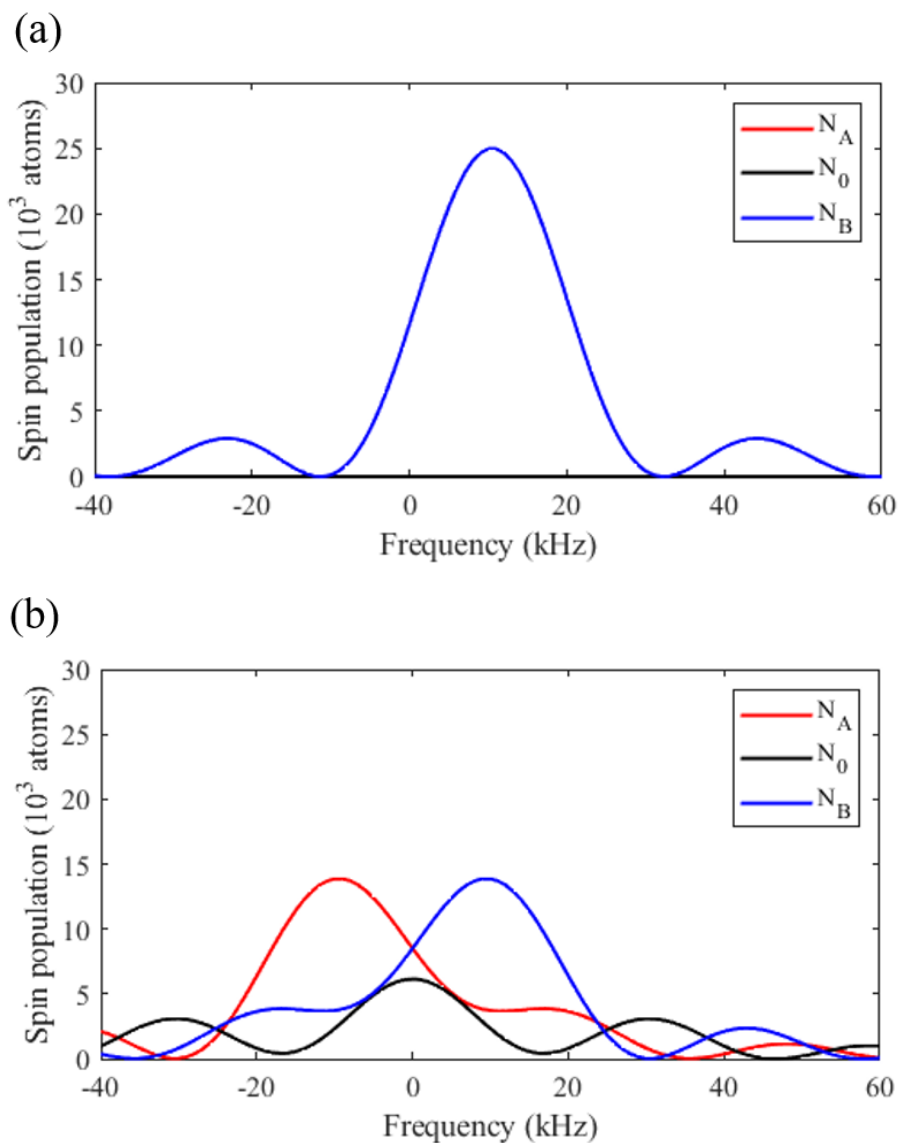


Figure 4.19: This is a simulation showcasing the selection of a single transition via polarization selectivity, with level spacings defined by the Zeeman splitting at 15 mG. These are simulated microwave spectra using parameters to match the experiment. (a) shows the polarization-selective case. (b) shows the non-selective case.

4.5.2 Low Field Selectivity

In the experiment, the circularly polarized microwave field was applied to select two-level σ transitions at low magnetic fields, where the hyperfine transitions can begin to overlap. In this low field case, an application of a single oscillating field can drive multiple transitions

due to the small spacing (Δ) between the levels. As has already been seen, the polarization can be used to select a desired transition, and block others. To show another application of this, the bias field in the experiment was set to 15 mG, corresponding to a Zeeman splitting of $\Delta = 10.5$ kHz, and the hyperfine transitions were measured. A measurement of the microwave spectrum Figure 4.20 shows the selective and non-selective cases in sub-figures (a) and (b), respectively. This measured data can be compared with the simulated result, Figure 4.19, showing clear similarity. At this low field, the two-level microwave transitions without selectivity are foiled by the presence of the other nearby transitions (Figure 4.21(b)). With the tool developed in this thesis, the two-level transition is cleanly driven (Figure 4.21(a)).

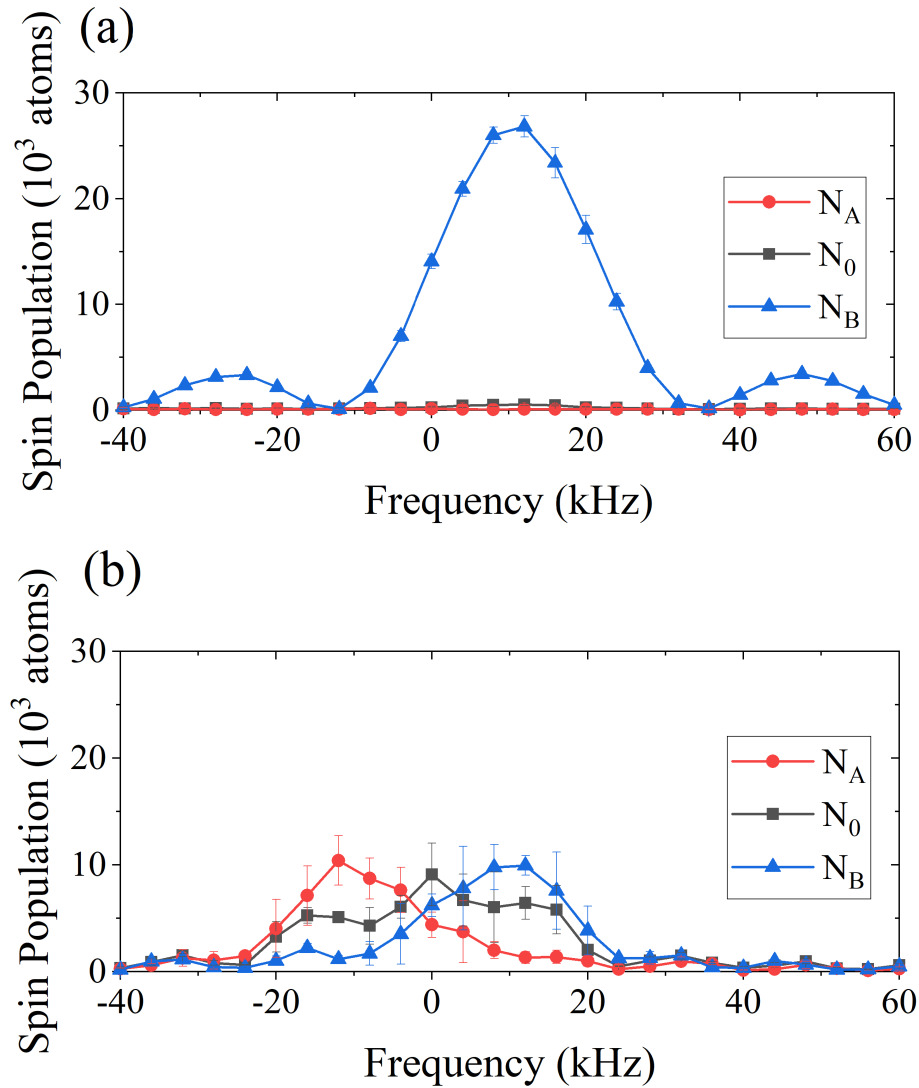


Figure 4.20: Microwave spectra taken at a low 15 mG bias field. (a) A microwave spectrum is measured with polarization selection. The microwave drives only the $|1, 0\rangle \rightarrow |2, +1\rangle$ transition. (b) A spectrum is measured without the polarization selection. Several states are populated.

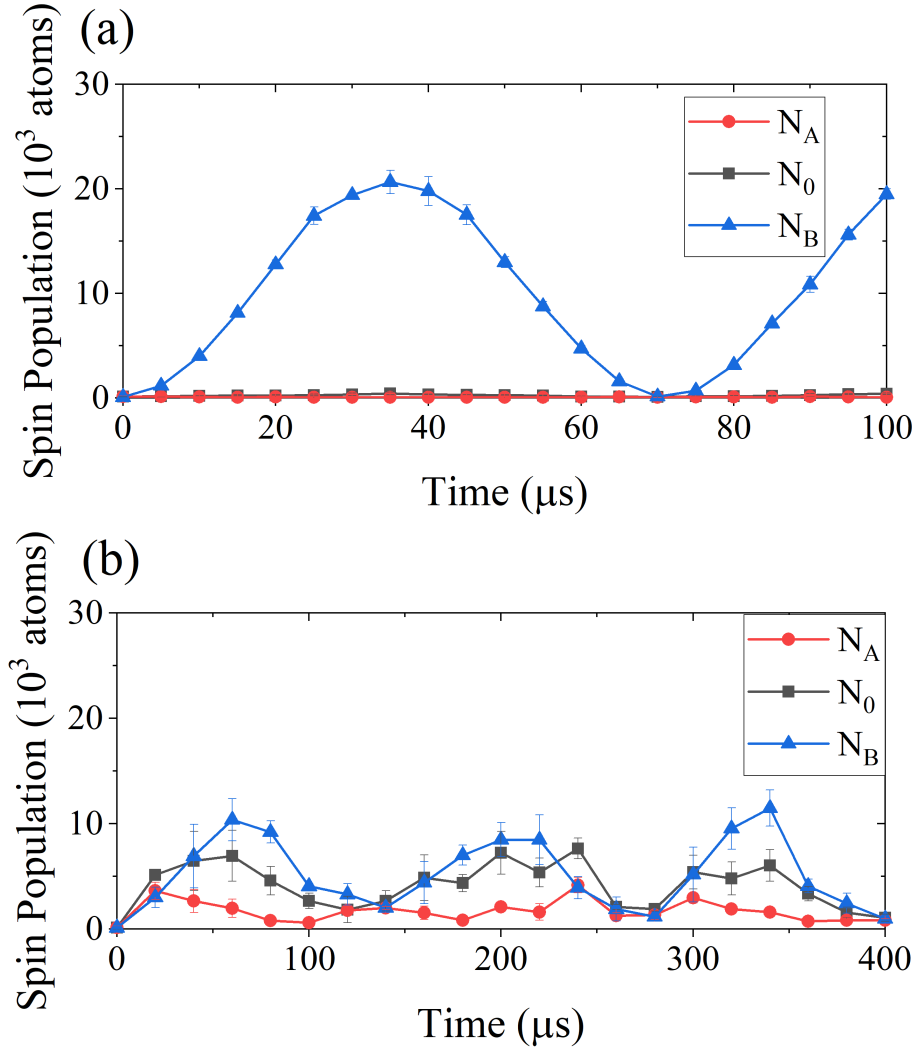


Figure 4.21: Microwave Rabi taken at a low 15 mG bias field showing the difference between the polarization selected and non-selected transitions. (a) Rabi rate in polarization selective case. (b) Rabi rate in non-selective case.

Faster Transitions

This selection of polarization alleviates the issues of broad microwave linewidths associated with faster, higher-power microwave pulses, by reducing off-resonant driving. For the two-level Rabi problem, the population in the excited state for the field turned on at $t = 0$ has the following form:

$$|c_e(t)|^2 = \left| \frac{\Omega}{\Omega'} \sin\left(\frac{\Omega't}{2}\right) \right|^2 \quad (4.4)$$

where $\Omega' = \sqrt{\Omega^2 + \delta^2}$, and Ω and δ are the Rabi rate and detuning. Equation 4.4 defines the microwave linewidth, where the amplitude has a full-width at half maximum of $\delta = 2\Omega$. If other transitions would have a significant non-zero value of $|c_e(t)|^2$ given their detuning from the microwave frequency, these transitions can also couple via the microwave field. This again is solved for the σ transitions by the polarization selection rules. As we have seen, the Rabi rate Ω is proportional to the amplitude of the microwave magnetic field, whereas the microwave power is proportional to the square of the microwave field ($B_{\mu w}^2$) and thereby the square of the Rabi rate (Ω^2). Again taking advantage of the circular polarization selection rules, high power, fast microwave transitions can be driven with large microwave linewidth avoiding the coupling of blocked transitions. This is a pathway to faster all-microwave state manipulation.

4.6 Concluding Remarks

Using a circularly polarized helical antenna, we were able to achieve a considerable discrimination between the transitions of different polarization within the hyperfine levels in our experiment. Experiments (performed at 200 mG) showed a selectivity of $(45.3 \pm 0.6)^{-1}$ — which is a $45.3\times$ difference in transition coupling strength (Rabi rate) between polarization selected and blocked transitions. Using this tool, a three-level Λ transition was measured with a maximum transfer fidelity of 99.5% for a π -pulse. This transition type has applications to state control schemes, and the tools demonstrated herein would allow for all-microwave implementations of these control schemes, such as a non-adiabatic holonomic gate. Additionally, another extension of this Λ transition would be the implementation an all-microwave tripod transition (the subject of next chapter). Further, the polarization selection was shown to allow rapid hyperfine transitions at low fields where the frequencies of many transitions are within the linewidth of the driving microwave field. This shows the utility of the polarization selection for increasing transition speeds, for more rapid state manipulations. Altogether, this work has demonstrated the successful application and utility of

a circularly polarized microwave source for selecting (and blocking) hyperfine transitions.

CHAPTER 5

TRIPOD TRANSITION

This chapter explores an extension from the Λ transition designed to allow arbitrary control of the ground state $F = 1$ hyperfine levels of rubidium-87. The so-called *tripod* transition will, similar to the Λ transition, apply a control operation on the $F = 1$ levels by coupling each magnetic sublevel (m_F state) to a single mediating state in the $F = 2$ level. Whereas the Λ transition performs an $SU(2)$ transformation on two base states, the tripod transition produces an $SU(3)$ transformation upon three base states. Two such tripod pulses capable of producing any arbitrary $SU(3)$ operator.

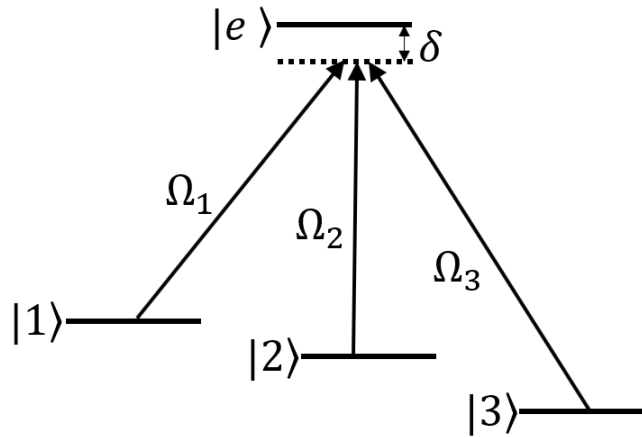


Figure 5.1: The tripod transition, called so because of the shape of the three level couplings. The quantities Ω_1 , Ω_2 , and Ω_3 are the single-photon Rabi rates. A detuning in frequency, δ , is shared by all the driving fields.

This chapter will discuss our attempts at implementing this tripod transition in our

experiment. A brief motivation of the tripod transition following theory from ref. [53] will be presented, followed by results of calculations and simulations. Then, details will be discussed for the experimental attempts at implementing such a tripod transition in our experiment. Finally, the use of circularly polarized microwaves is proposed as a future avenue for realizing such a tripod scheme. This four-level system is directly applicable to large number of projects working with spinor condensates in the $F = 1$ hyperfine manifold, including spinor BEC projects working with ^{23}Na and ^{87}Rb .

Recently, a related tripod scheme has been implemented in cold strontium atoms [75]. In this work, polarized optical fields were used to couple three base states to an optically excited state and generate arbitrary transformations on the base states via an adiabatic transformation. The microwave-based scheme presented here will produce non-adiabatic transformations of the state. This distinction, and the associated advantages, will be discussed within the chapter.

5.1 Tripod Transition– Theory

The theory for this non-adiabatic tripod transition was presented by Dr. Bharath H.M. in ref. [53]. A short summary of the theory will be presented in this section in order to facilitate in the discussions which follow. The four levels of the tripod transition consist of three lower levels coupled to one excited level which mediates the transitions. This level structure is illustrated in Figure 5.2, with labels indicating which levels in the ground-state hyperfine structure of ^{87}Rb are involved. Each of the $F = 1$ levels is coupled to the excited state $|2, 0\rangle$ via a microwave-frequency oscillating magnetic field. The Hamiltonian for this microwave interaction is Eqn. 3.14. We will take the detuning, δ , of each transition in the tripod to be equal, as this is sufficient for generating arbitrary transformations.

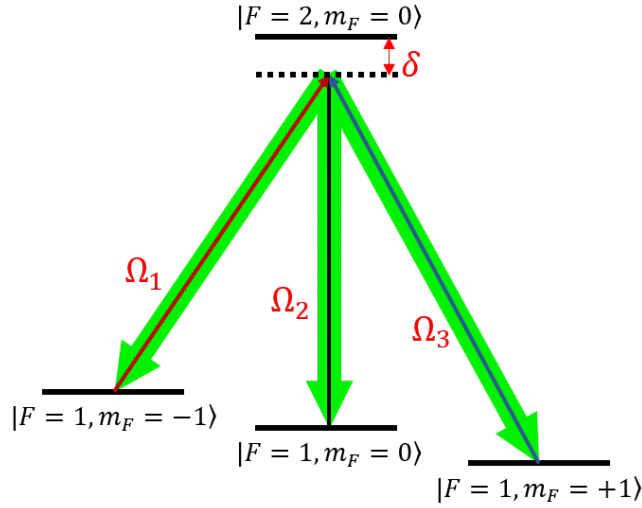


Figure 5.2: The tripod transition, three-level coupling to a mediating state. The Rabi rate of each coupling is denoted as Ω_i for $i = 1, 2, 3$. The detuning of each driving field is δ .

Following ref. [53], we will write this Hamiltonian in the interaction picture and take the rotating wave approximation giving:

$$H = \begin{pmatrix} \delta & \frac{1}{2}\Omega_1 & \frac{1}{2}\Omega_2 & \frac{1}{2}\Omega_3 \\ \frac{1}{2}\Omega_1^* & 0 & 0 & 0 \\ \frac{1}{2}\Omega_2^* & 0 & 0 & 0 \\ \frac{1}{2}\Omega_3^* & 0 & 0 & 0 \end{pmatrix} \quad (5.1)$$

Where Ω_i (for $i = 1, 2, 3$) is the complex-valued coupling strength. This Hamiltonian has the eigenenergies and eigenvectors shown in table 5.1. Here, a collective coupling strength is defined as $|\Omega|^2 = |\Omega_1|^2 + |\Omega_2|^2 + |\Omega_3|^2$.

Table 5.1: The eigenenergies and corresponding eigenvectors for Hamiltonian 5.1

Eigenvalue	Eigenvector
0	$-\Omega_3 1\rangle + \Omega_1 3\rangle$
0	$-\Omega_2 1\rangle + \Omega_1 2\rangle$
$\frac{1}{2}(\delta + \sqrt{\delta^2 + \Omega ^2})$	$(\delta + \sqrt{\delta^2 + \Omega ^2}) e\rangle + \Omega_1^* 1\rangle + \Omega_2^* 2\rangle + \Omega_3^* 3\rangle$
$\frac{1}{2}(\delta - \sqrt{\delta^2 + \Omega ^2})$	$(\delta - \sqrt{\delta^2 + \Omega ^2}) e\rangle + \Omega_1^* 1\rangle + \Omega_2^* 2\rangle + \Omega_3^* 3\rangle$

The important features of this eigenstructure are the states with zero-valued eigenvalues. The two corresponding eigenvectors are *dark states*, which are unaffected by the action of Hamiltonian 5.1.

$$|D_1\rangle = \frac{1}{\sqrt{|\Omega_1|^2 + |\Omega_3|^2}} (\Omega_3|1\rangle - \Omega_1|3\rangle) \quad (5.2)$$

$$|D_2\rangle = \frac{1}{\sqrt{|\Omega_1|^2 + |\Omega_2|^2}} (\Omega_2|1\rangle - \Omega_1|2\rangle) \quad (5.3)$$

Orthogonal to these two dark states, there is a *bright state*, $|B\rangle$, orthogonal to both dark states such that

$$\langle D_1|B\rangle = \langle D_2|B\rangle = 0$$

Solving for $|B\rangle$, the bright state is found to be

$$|B\rangle = \frac{1}{\Omega} (\Omega_1^*|1\rangle + \Omega_2^*|2\rangle + \Omega_3^*|3\rangle) \quad (5.4)$$

Note that this bright state is not an eigenstate of the Hamiltonian. Unlike the dark states, this bright state does evolve under the Hamiltonian 5.1, through excitation to the excited state $|e\rangle$. There are special revival times, t_n , in the evolution under the Hamiltonian Eqn. 5.1

when the excited state population goes to zero, and the population returns fully to the lower ($F = 1$) energy levels.

$$t_n = \frac{2n\pi}{\sqrt{\delta^2 + \Omega^2}} \quad (5.5)$$

At these times the state transformation is given by ([53]):

$$\begin{aligned} e^{-iHt_n} |D_1\rangle &\rightarrow |D_1\rangle \\ e^{-iHt_n} |D_2\rangle &\rightarrow |D_2\rangle \\ e^{-iHt_n} |B\rangle &\rightarrow e^{-in\pi} e^{-i\frac{n\pi\delta}{\sqrt{\delta^2 + \Omega^2}}} |B\rangle \end{aligned} \quad (5.6)$$

This defines the evolution for the tripod transition. A state initialized in the bright state will simply acquire a phase at the revival times t_n . A general state will evolve with the projection into the bright state acquiring this phase, while the remainder of the state is dark and acquires no phase. Additionally, it can be seen from Eqn. 5.6 that although the bright state is not an eigenstate of the Hamiltonian Eqn. 5.1, it is an eigenstate of a dressed Hamiltonian, with a term of the form $|B\rangle\langle B|$. This provides a new dressed state picture for the state evolution under the tripod. Manipulations performed with the tripod transition can be chosen through control of the amplitude and phase of each coupling strength ($\Omega_1, \Omega_2, \Omega_3$) and the detuning (δ) of the driving microwave fields. The bright state for the Hamiltonian corresponding to these parameters can then be easily determined, and each bright state determines a corresponding evolution for the tripod transition. It is interesting to note that setting one of the couplings to zero reduces the tripod to the Λ transition, and setting two couplings to zero gives the two-level Rabi problem.

5.2 Special Case: Λ Transition

For the Λ transition, we can set one of the coupling strengths of the tripod to zero (e.g. $\Omega_3 = 0$). In this case, there is a useful parameterization of the remaining two coupling

strengths, following ref. [67]

$$|B\rangle = e^{i\phi} \sin\left(\frac{\theta}{2}\right) |1\rangle - \cos\left(\frac{\theta}{2}\right) |2\rangle \quad (5.7)$$

This parameterization for θ and ϕ gives a simple unit vector that defines the axis of rotation resulting from the Λ transition. The state on the Bloch sphere rotates around $\hat{\mathbf{n}}$, given by

$$\hat{\mathbf{n}} = (\sin(\theta) \cos(\phi), \sin(\theta) \sin(\phi), \cos(\theta)) \quad (5.8)$$

5.3 Example Bright State

As an example, one transformation which we would like to be able to perform is the equivalent of the rf transition ($\pi/2$ -pulse) between the $F = 1$ levels. This transition (in the rf case) has equal coupling strength from $m_F = 0$ to each of the $m_F = -1$ and $m_F = +1$ states. With the tripod transition, a bright state corresponding to the Hamiltonian which would drive the equivalent of an rf transition in the $F = 1$ levels is:

$$|B_{rf}\rangle = (\Omega)|1, 1\rangle + (\sqrt{2}\Omega)|1, 0\rangle + (\Omega)|1, -1\rangle \quad (5.9)$$

Here, the coupling strengths are $(\Omega_1, \Omega_2, \Omega_3) = (\Omega, \sqrt{2}\Omega, \Omega)$ and the detuning is $\delta = 0$. A simulated result of the tripod transition applied by a Hamiltonian with this bright state is shown in Figure 5.3. At the time t_n , here $209 \mu\text{s}$, the population is equivalent to that of the rf-transition $\pi/2$ pulse, where there is complete transfer of population from the $m_F = 0$ state to the $m_F = -1$ and $m_F = +1$ states.

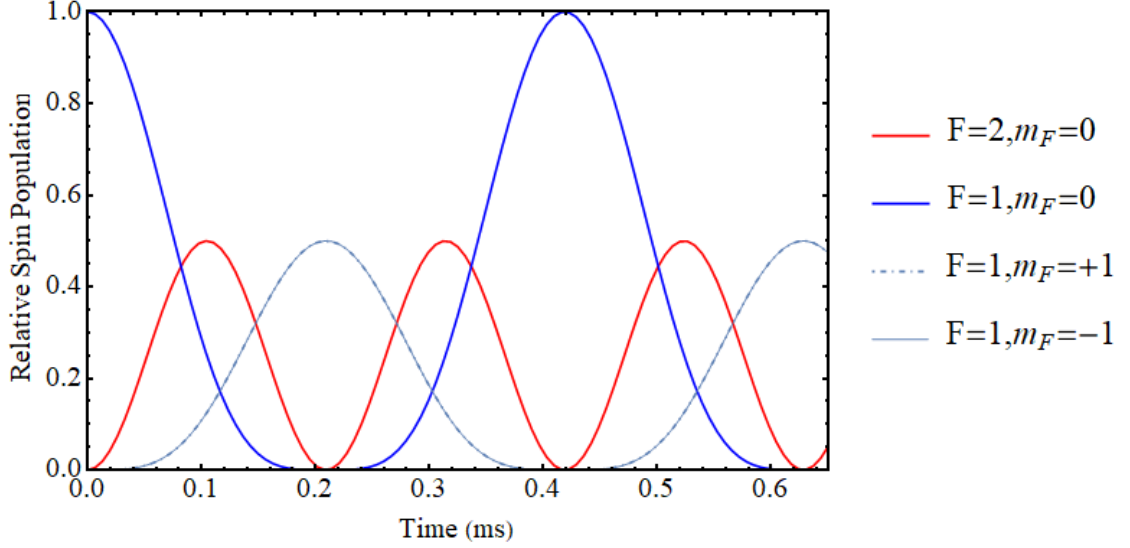


Figure 5.3: The tripod evolution of the initial state $|1, 0\rangle$ under the Hamiltonian 5.1 with the bright state $|B_{rf}\rangle$, Eqn. 5.9. The legend on the right indicates the states corresponding the different plotted lines. Here, $\Omega = 15$ kHz and the detuning was zero ($\delta = 0$ Hz). For this bright state and detunings, the revival time $t_n = n \cdot 209 \mu\text{s}$. Note: the $|1, 1\rangle$ and $|1, -1\rangle$ states coincide exactly.

5.4 Adiabatic vs Non-Adiabatic Evolution

The tripod and Λ transitions are example of fan-linkage type transformations, with multiple lower energy levels coupled to one excited energy level [57]. There are two distinct classes of evolution in transitions such as the tripod transition, adiabatic or non-adiabatic. A system initialized in the dark state will remain in this dark state under evolution of the Hamiltonian. Conversely, the bright state will evolve under this Hamiltonian. This section will briefly compare the two classes for the tripod transition.

Adiabatic

In the adiabatic case, the Hamiltonian is time-dependent and within the adiabatic approximation. The system is prepared in a dark state of the Hamiltonian. Then the Hamiltonian

is slowly tuned, such that the state adiabatically follows the changing dark state. This is discussed in, for instance, ref. [118]. Notice that in the case of the adiabatic evolution, the excited level ($|e\rangle$) with initially zero population will remain unpopulated. That is, there will be no excitation to this excited state since adiabaticity is satisfied. An example of this is the STIRAP transition.

A benefit of this adiabatic evolution is the robustness to spontaneous decay from the excited state, since there is no excitation to the excited state. This is a concern for a transformation based on optical transitions with short lifetimes [75]. However, this spontaneous decay is not of concern for transformations based on microwave transitions between hyperfine levels, which offer long lifetimes. One downside of the adiabatic transformation is the complication of varying the Hamiltonian adiabatically in time, which places a limit the rate of manipulation.

Non-Adiabatic

In the non-adiabatic case, the transformation is effected through excitation to the excited level ($|e\rangle$), where this excited state acts as a mediating state. In this case the Hamiltonian is time-independent other than the overall amplitude envelope (turning the fields on and off). A system initially prepared within the lower energy level subspace $\{|0\rangle, |1\rangle, |2\rangle\}$ and is coupled to the excited state and within the state space $\{|0\rangle, |1\rangle, |2\rangle, |e\rangle\}$. In the case that the two-photon resonances are satisfied (i.e. equal detuning for all driving fields), there are special times when the excited state population goes to zero ($\langle e|e\rangle \rightarrow 0$). At these population revival times the state returns to the lower energy level subspace leaving the excited state unpopulated. At this point, the tripod fields are shut off, and an $SU(3)$ transformation has been performed on the $\{|0\rangle, |1\rangle, |2\rangle\}$ subspace. This non-adiabatic class of transformations can be faster than the adiabatic transformations, since there is not a limitation set by the rate of Hamiltonian change. Additionally, these transformations can be simpler in implementation, since the driving fields do not need to be modulated, only

gated on with control of the initial phases and the time-independent relative amplitudes.

The tripod transition we studied fell within this non-adiabatic class of transformations. The intended use of this tripod is twofold:

- The tripod transformation allows for arbitrary control of the spin-1 state via non-adiabatic transformations. With the application of two tripod transformations, any arbitrary SU(3) operation could be performed on the spin-1 state [53].
- The all-microwave based tripod would allow for measurements of arbitrary expectation values. At half the revival time t_1 , i.e. $t_1/2$, the bright state is mapped to the $|2, 0\rangle$ state, with amplitude determined by the detuning. At this point, the population in the upper $F = 2$ hyperfine level can be measured, giving the projection of atoms that were initially in the bright state. This can be repeated multiple times on the population left in the $F = 1$ state to measure several expectation values on the same prepared population of atoms. Note that such a scheme cannot be realized in the adiabatic transformations, such in an optical tripod transition, since the excited electronic states are not populated.

5.5 Attempts at a Tripod Implementation

The main complication in the implementation of the tripod in the ^{87}Rb ground state is the presence of unwanted, degenerate transitions. The tripod couplings within the level structure are illustrated in Figure 5.4. In order to lift the degeneracies, we implemented an off resonant optical field to selectively shift the energies of different ground state levels. Then, a “multi-tone” microwave setup was designed to provide all the needed microwave fields for the three couplings of the tripod transition. This section will discuss both the light shift and the multi-tone setup.

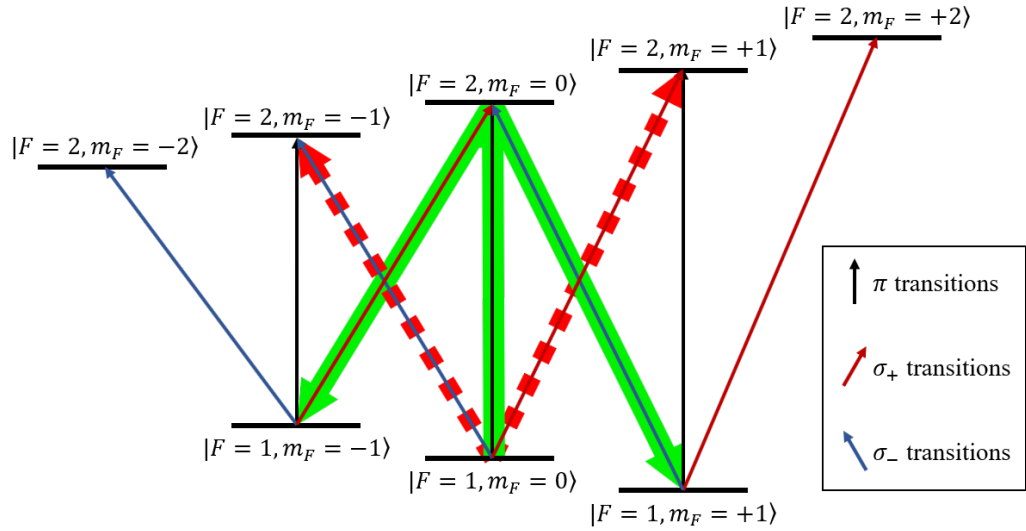


Figure 5.4: The tripod in the eight-level hyperfine structure. The tripod transformation couplings are highlighted in green. The undesired degenerate coupling is highlighted in dashed red.

5.5.1 Light Shift

A scheme identified to lift this degeneracy was a light shift, or the AC stark shift from a laser detuned from the D1 transition (this transition wavelength is ≈ 794.979 nm). A related use of a light shift in combination with microwave transitions can be seen in, for instance, ref. [119], where light shift was used to shift lattice sites into resonance with an applied microwave field. For the tripod transition, the intent was to use the light shift to detune the energy levels which are not participating in the tripod, specifically the $|F = 2, m_F = \pm 1\rangle$ states. In this way, the scattering rate from these levels was not directly important, as these levels should not be populated by the tripod transition. The key idea behind the light shift for the tripod transition is to take advantage of the dipole transition matrix elements for the π -polarized D1 transition from $F = 2$ to $F' = 2$. This transition features a zero-valued matrix element for the $m_F = 0 \rightarrow m'_F = 0$ transition, and non-zero elements for the $m_F = \pm 1 \rightarrow m'_F = \pm 1$ transitions. With a carefully set laser polarization relative to the

bias field direction, the undesired transitions can be light-shifted out of degeneracy with the tripod transitions. The energy levels with this light shift are illustrated in Figure 5.5.

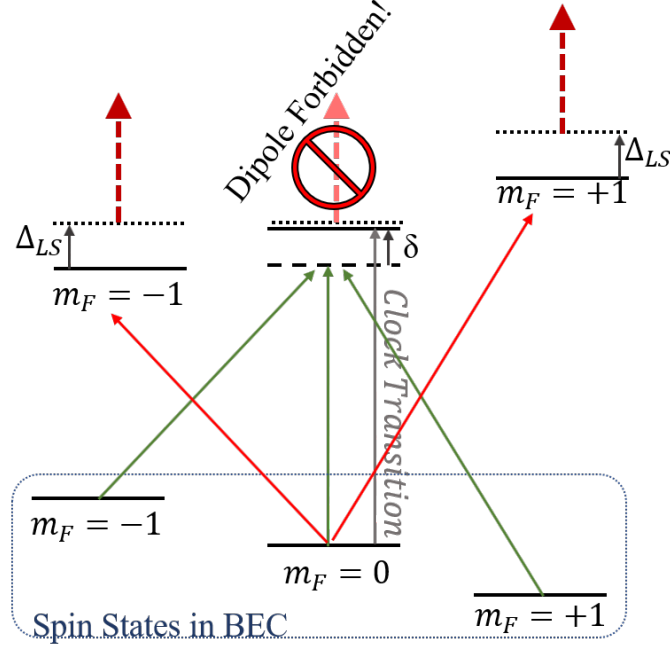


Figure 5.5: The light shift used to detune the undesirable Δ transitions and lift the degeneracy around the tripod transitions. Here, Δ_{LS} represents the light-shifted energy level. The green arrows show the tripod couplings. The solid red arrows show the degenerate Δ transitions. The red dashed arrows illustrate the applied light shift from the D1 laser light.

5.5.2 Calculation for Light Shift and Scattering Rate

Light Shift

Aside from the $F = 2 \rightarrow F' = 2$ transitions, the transitions from $F = 2 \rightarrow F' = 1$ also play a role in the light shift and scattering from the $F = 2$ level. In order to calculate the amplitude of the light shift accurately, a calculation was performed including contributions from all the nearby transitions. Following ref. [120], the amplitude of the shift for a two-level atom is given by

$$\Delta E = \pm \frac{|\langle e|\mu|g\rangle|^2}{\Delta_{D1}} |E|^2 = \pm \frac{3\pi c^2 \Gamma}{2\omega_0^3} \frac{I}{\Delta_{D1}}$$

where $\Delta_{D1} = \omega - \omega_0$ is the detuning of the driving D1 laser electric field (of frequency ω) from the transition frequency ω_0 , I is the electric field intensity ($I = 2\epsilon_0 c |E|^2$), and

$$\Gamma = \frac{\omega_0^3}{3\pi\epsilon_0\hbar c^3} |\langle e|\mu|g\rangle|^2 \quad (5.10)$$

is the lifetime of the excited state. The extension of this to multiple levels is simply a summation over individual two-level transitions in the case where cross-correlations (such as multi-photon processes) are negligible. This two-level summation is justified here as the light shift will be small in amplitude compared to the level separations, and each transition is separated by at least Δ , the linear Zeeman energy shift.

$$\Delta E_i = \frac{3\pi c^2 \Gamma}{2\omega_0^3} I \sum_j \frac{c_{ij}^2}{\Delta_{ij}} \quad (5.11)$$

where Γ is again the decay rate, c_{ij} are the reduced matrix coefficients, such that $\mu_{ij} = c_{ij} \|\mu\|$, and j is the index of each excited state $|e_j\rangle$ coupled to the ground state $|g_i\rangle$. The term $\|\mu\|$ is a reduced matrix element for the transition and is contained in $\Gamma = \frac{\omega_0^3}{3\pi\epsilon_0\hbar c^3} \|\mu\|^2$. Each coupling has a distinct line strength and detuning, described by each transition coefficient c_{ij} and detuning Δ_{ij} .

In the table below, the transition coefficients c_{ij} are given for π transitions expressed as multiples of $\|\mu\|$ for the D₁ ($5^2S_{1/2} \rightarrow 5^2P_{1/2}$) transition [112]. Notice that the $m_F = 0$ transition matrix element for $F = 2 \rightarrow F' = 2$ is zero-valued. This is the key to the application of the differential light shift, which will shift the $m_F \neq 0$ transitions, but not this $m_F = 0$ transition.

Scattering Rate

However, the light shift is only half of the story here. The light which sets up the light shift also can scatter from the shifted transitions. It is therefore also necessary to calculate scat-

Table 5.2: Transition matrix elements for the π polarization $F = 2 \rightarrow F'$ D1 transitions in ^{87}Rb . For these transitions, the initial and final m_F are equal ($m'_F = m_F$).

$(m'_F = m_F)$	$m_F = -2$	$m_F = -1$	$m_F = 0$	$m_F = 1$	$m_F = 2$
$F = 2 \rightarrow F' = 2$	$-\sqrt{\frac{1}{3}}$	$-\sqrt{\frac{1}{12}}$	0	$\sqrt{\frac{1}{12}}$	$\sqrt{\frac{1}{3}}$
$F = 2 \rightarrow F' = 1$		$\sqrt{\frac{1}{4}}$	$\sqrt{\frac{1}{3}}$	$\sqrt{\frac{1}{4}}$	

tering rates for each channel that participates in the light shift. This calculation similarly follows that of ref. [120], but is extended to all the scattering channels. For the two-level problem, the scattering rate has the form:

$$\Gamma_{sc} = \frac{3\pi c^2}{2\hbar\omega_0^3} \left(\frac{\Gamma}{\Delta_{D1}} \right)^2 I \quad (5.12)$$

Similarly, a sum is taken over all the matrix elements to account for all the scattering channels to get the form of

$$\Gamma_{sc} = \frac{3\pi c^2}{2\hbar\omega_0^3} (\Gamma)^2 I \sum_j \left(\frac{c_{ij}^2}{\Delta_{ij}} \right)^2 \quad (5.13)$$

Numerical Results for Light Shift and Scatter

Using Eqns. 5.11 and 5.13, the light shift and photon scattering rate were calculated for each of the hyperfine sublevels. The objective of using this light shift is to detune the undesired transitions outside of the microwave linewidth for the individual transitions for the tripod. For this purpose, there are two quantities of main interest: the differential light shift and the scattering rate. The differential light shift is the difference in the light shift between the levels for the tripod transitions (green transitions in Figure 5.4) and the unwanted, degenerate transitions (red dashed transitions in Figure 5.4). Since the light shift is small and similar for the $F = 1$ levels, the differential light shift is approximately the shift of the $|2, 0\rangle$ state compared to the $|2, \pm 1\rangle$ states. The important scattering rates are for the levels involved in the tripod transition. The $|2, 0\rangle$ level shows the most significant

scattering rate out of these tripod levels, due to the detuned coupling of $F = 2 \rightarrow F' = 1$. Results from this calculation are tabulated below for detunings of 200 MHz, 50 MHz, and 25 MHz, and each with a different intensity, such that the differential light shift was similar. From these results, it is clear that π -polarized light with a similar differential light shift but at lower detuning has correspondingly lower scattering rates from the $|2, 0\rangle$ state.

Table 5.3: Light shift at 200 MHz detuning

m_F state:	$m_F = -2$	$m_F = -1$	$m_F = 0$	$m_F = 1$	$m_F = 2$
Light Shift (Hz) $F = 2$	74303	29539	14617	29539	74303
Light Shift (Hz) $F = 1$		-2318	-2240.	-2318	
Scattering Rate (Hz) $F = 2$	28112	2368.92	1088	2369	28112
Scattering Rate (Hz) $F = 1$		16	26	16	
Intensity (mW/cm ²)			2.568		

Table 5.4: Light shift at 50 MHz detuning

m_F state:	$m_F = -2$	$m_F = -1$	$m_F = 0$	$m_F = 1$	$m_F = 2$
Light Shift (Hz) $F = 2$	63606	18654	3670.	18654	63606
Light Shift (Hz) $F = 1$		-485	-469	-485	
Scattering Rate (Hz) $F = 2$	96257	6196	320	6196	96257
Scattering Rate (Hz) $F = 1$		3	5	3	
Intensity (mW/cm ²)			0.550		

Table 5.5: Light shift at 25 Hz detuning

m_F state:	$m_F = -2$	$m_F = -1$	$m_F = 0$	$m_F = 1$	$m_F = 2$
Light Shift (Hz) $F = 2$	61805.	16828.	1836	16828	61805.
Light Shift (Hz) $F = 1$		-235	-227	-235	
Scattering Rate (Hz) $F = 2$	187065.	11784	165	11784	187065.
Scattering Rate (Hz) $F = 1$		2	3	2	
Intensity (mW/cm ²)			0.212		

Implementation of Light Shift

We implemented a D1 laser setup with an adjustable detuning from the $|F = 2, m_F = 0\rangle \rightarrow |F' = 2, m'_F = 0\rangle$ transition (see Figure 2.6). The polarization was set carefully with a Glan-Thompson prism, which should have exceptional linear polarization extinction ratio. This polarizer was mounted in a rotation mount between a chamber viewport and the output of an optical fiber with the D1 light. The orientation of the laser polarization requires precise alignment, since this method relies on driving purely the π transition. The orientation could be set both with the rotation of this polarizer and also with the direction of the bias field. For alignment of the polarization, the laser intensity was increased and the detuning was decreased, such that the transition was strongly driven. For a perfect π -polarization alignment, the $|F = 2, m_f = 0\rangle$ state will be unaffected by this light (except for a small contribution from the $F = 2 \rightarrow F' = 1$ coupling). However, any deviation from this alignment meant there was a projection of σ_{\pm} polarization to drive the transition—then atoms would be excited by this laser and lost from the trap.

In order to align the polarization, the BEC was initialized in the $|1, 0\rangle$ state. Then, a microwave π -pulse resonant with the clock transition was applied to populate the $|2, 0\rangle$ state and the D1 light shift laser was pulsed on. This laser was seen to excite atoms in the trap, measured as atom loss. The parameters of the D1 laser (intensity, detuning, and

pulse duration) were varied such that many atoms still remained in the trap. The angle of either the polarizer or the bias field could then be varied to try to reduce the atom loss. Reduced atom loss corresponded to a smaller projection of laser electric field into undesired σ polarizations. This process was iterated until the smallest depletion of atoms from the trap was measured.

Light Shift Results

Using this setup, differential light shifts of the tripod transitions relative to the undesired transitions were measured through microwave spectra. Three different types microwave spectra could be compared for each applied light shift. Two of the spectra were simply taken as usual by scanning the microwave frequency and measuring the resonance frequency of the clock transition $|1, 0\rangle \rightarrow |2, 0\rangle$ and one of the delta transitions $|1, 0\rangle \rightarrow |2, \pm 1\rangle$. The shift of each of these transition frequencies is the sum of the light shifts of the two levels involved. The delta transition measured this way should see a larger light shift than the clock by the differential light shift. The third type of spectrum is a measurement of the transition $|1, \pm 1\rangle \rightarrow |2, 0\rangle$. This spectrum was measured by first applying a rf $\pi/2$ -pulse to transfer the atoms to equal populations in the $|1, \pm 1\rangle$ states. With these states populated, a microwave spectrum is taken to measure the $|1, \pm 1\rangle \rightarrow |2, 0\rangle$ transitions. These transitions should show a light shift amplitude similar to the clock transition, as the light shift is primarily due to the shift of the $|2, 0\rangle$ level for both transitions. An example of these different spectra can be seen in Figure 5.6.

The most successful measurements of the light shift were made using a large detuning ($\delta = 200$ kHz) for the D1 laser. This was problematic, however, since the larger detuning required a greater intensity to induce a similar light shift. And although there the special zero-valued matrix element blocks the $|F = 2, m_F = 0\rangle \rightarrow |F' = 2, m'_F = 0\rangle$ transition, the matrix element for the $|F = 2, m_F = 0\rangle \rightarrow |F' = 1, m'_F = 0\rangle$ transition is non-zero. This meant the clock transition $|F = 1, m_F = 0\rangle \rightarrow |F' = 2, m_F = 0\rangle$ also

saw a significant light shift, even in the case of pure π -polarization (see table 5.3). A differential light shift of about 12 kHz was measured, where the undesired transitions were shifted by about 24 kHz but the tripod transitions were also shifted by about 12 kHz. Note that the ratio of these light shifts is in agreement with table 5.3, for which the amplitude is slightly larger as the calculation was made for a slightly higher intensity than used in the experiment. With this 12 kHz differential light shift at 200 MHz detuning from the $F = 2 \rightarrow F' = 2$ transition, there was difficulty in driving the transitions needed for the tripod coherently. The microwave transitions with the light shift applied were measured to have lower maximal amplitudes, indicating decoherence, either scattering from the σ -polarizations or instabilities in the light-shift laser. Measurements of spectra with the light shift applied at 200 MHz detuning can be seen in Figure 5.6.

From the numerical calculations, the polarization-selection based differential light shift should perform better with lower detunings from the $|F = 2, m_F = 0\rangle \rightarrow |F' = 2, m'_F = 0\rangle$ transition, assuming the light is π -polarized, since there is proportionally lower scatter. At these lower detunings, the zero-valued matrix element makes a significant difference. However, in experiment, several lower detunings were tried between 20 MHz and 200 MHz. For the lower detunings, the transitions showed such significant prohibitive levels of decoherence such that the spectra could not be reliably measured, let alone used to accurately measure a resonance to determine the amplitude of light shift. With the excess of decoherence, and moderately small differential light shift (e.g. 12 kHz), this light shift was not sufficient to lift the degeneracies for an implementation of the tripod transition without the unwanted transitions.

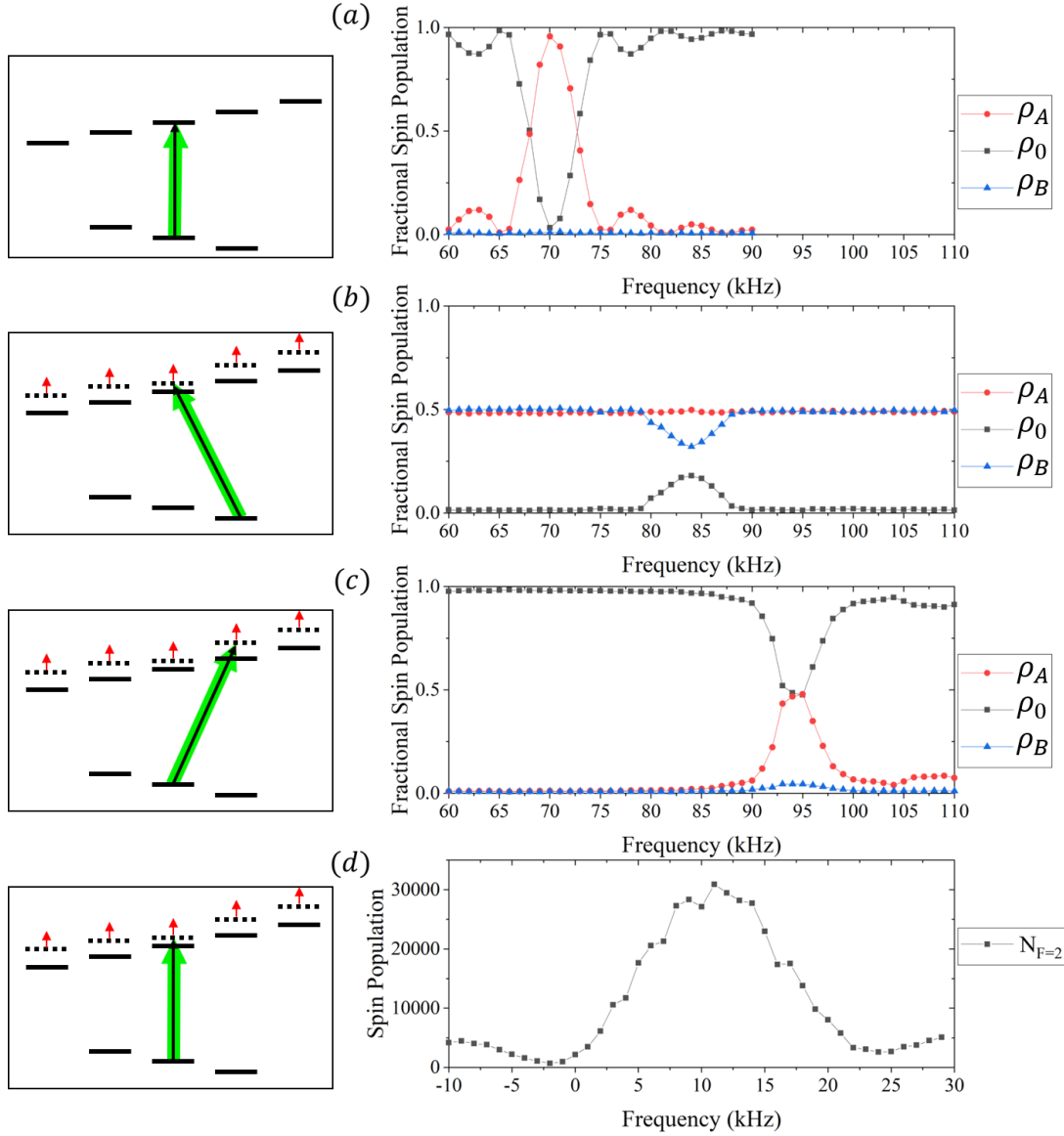


Figure 5.6: Microwave spectra showing the effect of the 200 MHz detuned light shift. Energy level diagrams (on left) indicate the transition with the corresponding spectrum measured (on right). The red vertical arrows indicate the presence of the light shift. (a) The $|1, 0\rangle \rightarrow |2, +1\rangle$ resonance with no light shift applied is measured at 70.6 kHz. (b) The $|1, +1\rangle \rightarrow |2, 0\rangle$ resonance is measured at 83.8 kHz with an initial rf $\pi/2$ -pulse and the light shift applied. (c) The $|1, 0\rangle \rightarrow |2, +1\rangle$ resonance is measured at 94.4 kHz with the light shift applied. (d) The $|1, 0\rangle \rightarrow |2, 0\rangle$ resonance is measured at 11.1 kHz with the light shift applied. The differential light shift is approximately between the values $(94.4 \text{ kHz} - 70.6 \text{ kHz}) - 11.1 \text{ kHz} = 12.7 \text{ kHz}$, and $94.4 \text{ kHz} - 83.8 \text{ kHz} = 10.6 \text{ kHz}$, calculated from the measured light shifts presented here

5.5.3 Multi-Tone Microwave Setup

The tripod transition requires three microwave fields, each with a separate frequency, amplitude, and relative phase. An arbitrary waveform generator (AWG) is capable of outputting the sum of three such waveforms, however, an AWG at microwave frequencies is cost-prohibitive. An alternative approach was attempted using a lower frequency AWG to generate the sum of three signals with the correct amplitudes, phases, and frequency differences, at a much lower carrier frequency (e.g. around 10 MHz). These this multiple-tone (“multi-tone”) signal could then be mixed, via an upconverting mixer, with a microwave signal offset from the clock transition by the carrier frequency of the AWG (e.g. 6.834 GHz – 10 MHz). The output of the upconverting mixer will have all the tones needed for the tripod transition, as well as additional sidebands greatly detuned by twice the AWG carrier frequency. Altogether, this setup is quite simple. The parameters needed for the tripod transition can be set by the AWG. The signal, mixed up to the correct microwave frequency, is amplified and applied with a single microwave antenna. A schematic of the setup is shown in Figure 5.7.

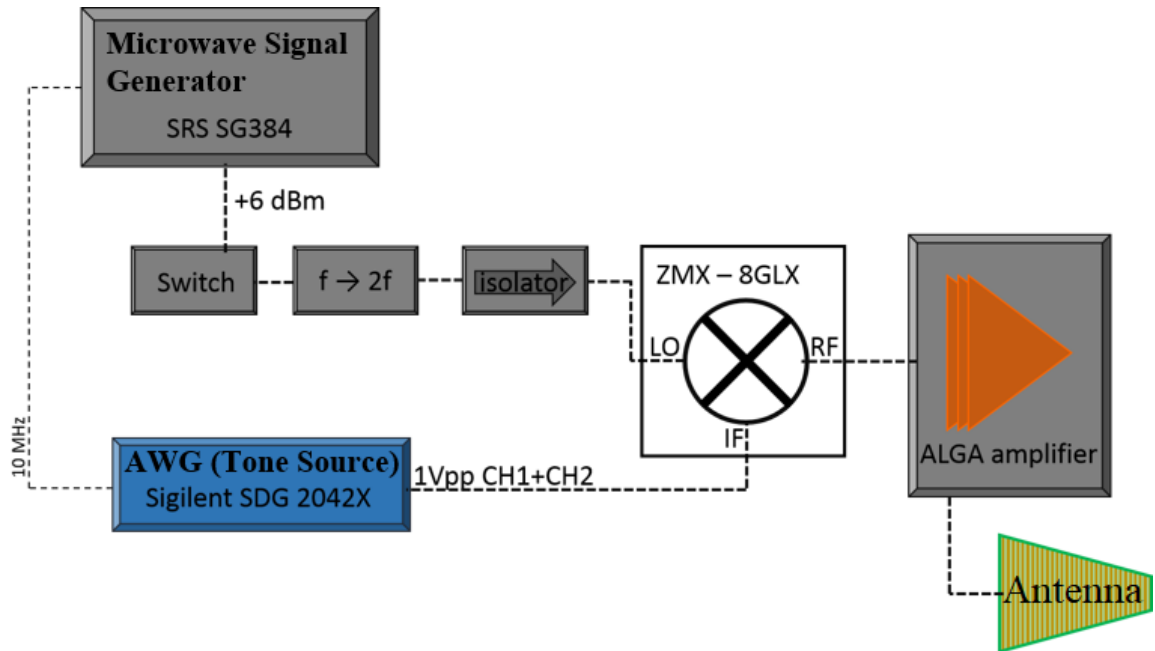


Figure 5.7: Schematic setup for multi-tone microwave signal generation. The multi-tone signal is produced by the AWG (Sigilent SDG 2042X). The microwave signal is produced by an SRS SG384 signal generator, with the output switched and frequency doubled before the mixer. The upconverting mixer (Minicircuits ZMX-8GLX) receives the rf multi-tone signal on the IF input and the microwave-frequency input on the LO input. The output (RF) is amplified by the Alga Microwave amplifier (model ALPA 647240-50-01).

Using this setup, the multi-tone microwave was applied to the atoms with the tones for the Λ transition between the levels $|1, 1\rangle$, $|1, 0\rangle$, and $|2, 1\rangle$, as indicated in Figure 5.8. The level couplings are that of a Λ transition together with an undesired degenerate coupling. The result of this measurement can be seen in Figure 5.9. This figure shows a two-frequency multi-tone signal applied and measured as a Rabi cycle. This measurement shows that the multi-tone setup does indeed generate the desired tones. The individual Rabi rates for the two-level transitions of this Λ transition (green highlighted transitions in Figure 5.8) were measured separately. These Rabi rates were used to simulate the application of this multi-tone field with the degenerate coupling. The result of this simulation is seen in Figure 5.10. This simulation is successful in capturing some of the features measured for the multi-tone

Rabi. After further evaluations of this multi-tone system, it was determined that there was non-linearity in the multi-tone upconversion mixing. Measurements with a microwave-frequency spectrum analyzer indicated the multi-tone signal was distorted. Additionally for the multiple tones, each with an opposite sideband, limit the amount of power in each tone, as the amplifier has a limit for input power. Despite some success with this multi-tone setup, this non-linearity makes the particular hardware used in this setup inadequate for application of the tripod transition. The quantitative disagreement between the measurement with the two-tone microwave (Figure 5.9) and the simulated results (Figure 5.10) are likely due to the difference in the measured single transition Rabi rates (used for the simulation) and the reduced amplitude of these Rabi rates as a result to the non-linearity in the multi-tone microwave circuitry.

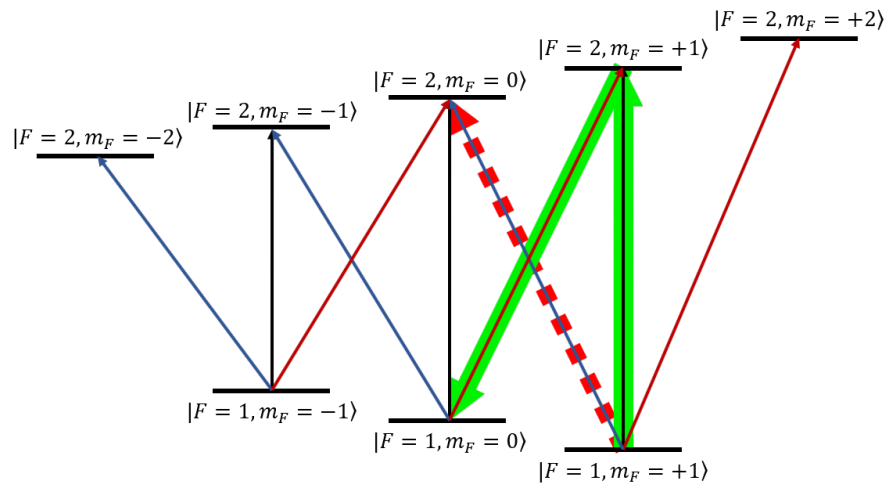


Figure 5.8: The level structure indicating which transitions were driven in the multi-tone Λ shown in Figure 5.9.

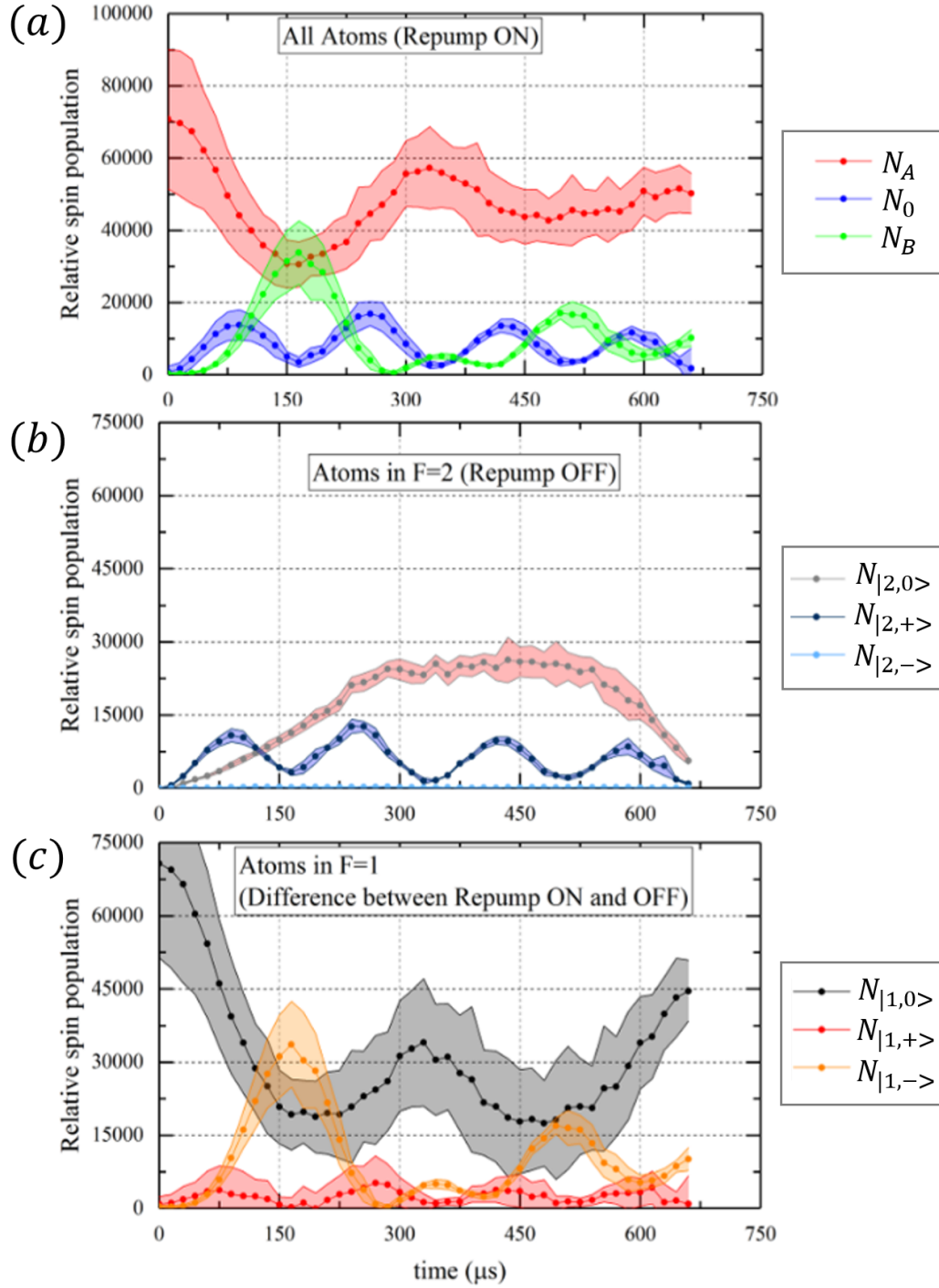


Figure 5.9: A two-tone Rabi cycle. Two microwave tones are applied through the multi-tone setup. (a) Shows the measurement with the the atoms in both $F = 1$ and $F = 2$. (b) Shows the measurement with only the populations in $F = 2$. (c) Shows the calculated atoms in $F = 1$, computed as the difference between the populations in (a) and (b).

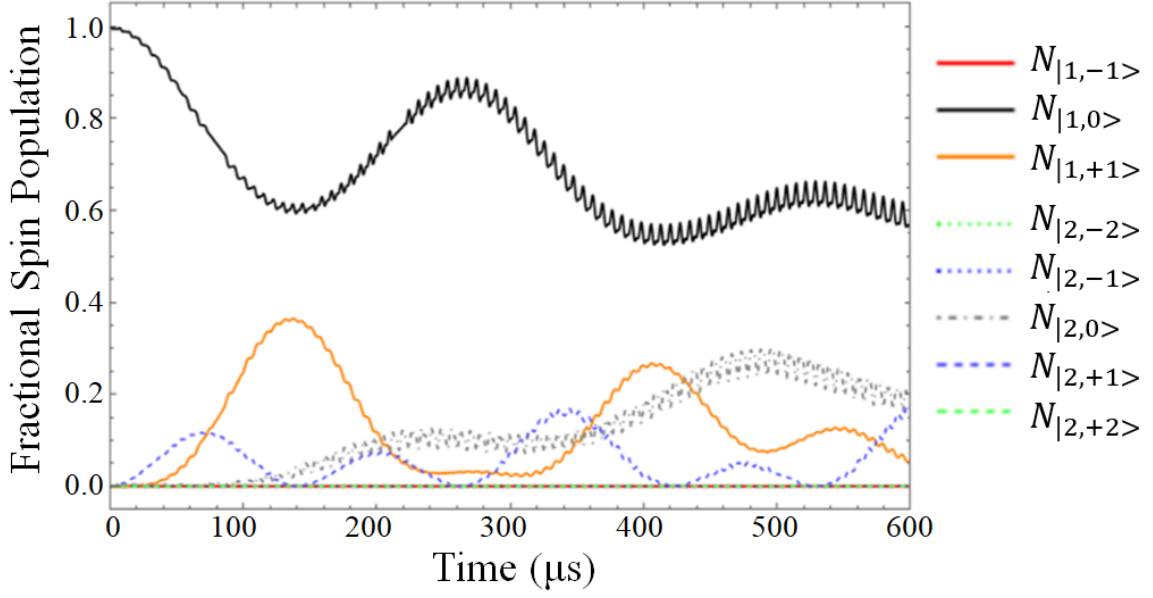


Figure 5.10: A simulation of the two-tone Rabi cycle, using Rabi rates as measured in the experiment. The populations show qualitative similarities with Figure 5.9. The Λ transition, highlighted green in Figure 5.9, suffers from the degeneracy of another transition, shown highlighted dashed red in Figure 5.9.

5.6 Concluding Remarks

It is clear following the success of the circularly polarized microwave study that a similar method could be used for the implementation of a tripod transformation. The tripod transition includes one transition of each of the π , σ_+ , and σ_- polarizations. This tripod transition therefore requires a second handedness of co-aligned circular-polarized microwave field. This represents an engineering challenge, but also a clear path towards the implementation of an all-microwave tripod transition. Here the selectivity of the microwave polarizations would block the undesired transitions, selecting only the couplings needed for the tripod transition. Since such a scheme needs both separately-controllable circular polarizations of opposite handedness, a tripod implementation would require additional development, along with more a somewhat more sophisticated microwave antenna setup.

Although the tripod transition was not successful in the end, this chapter presents a couple of interesting ideas on possible implementations of such a tripod transformation. The main difficulty in implementing this tripod scheme in ground-state ^{87}Rb is the presence of nearly-degenerate transitions at low field. This was precisely why the circular-polarization selection of hyperfine transitions studied.

CHAPTER 6

CONCLUSION

This thesis presents the body of work required and performed for the implementation of a microwave-frequency oscillating magnetic field with a circular polarization which can be used in the context of cold neutral atoms to select or block transitions of σ_{\pm} polarization. This study is motivated by potential applications in quantum state control. The results measured herein provide strong evidence for the effectiveness of the transition selectivity. At this point, I would like to make the strong point that this polarized microwave field provided an additional control parameter to our experiment with minimal added complexity. Several applications of this polarized field were studied, and ideas motivating additional studies were suggested, as well.

6.1 Circularly Polarized Microwave Manipulations

The results shown herein included experimental measurements confirming polarization selection of transitions by a factor of $(45.3 \pm 0.6)^{-1}$. This selectivity was more than sufficient to implement a high fidelity Λ -type three level transformation within the rubidium-87 hyperfine levels—resulting in a measured fidelity not limited by the methods developed herein, but instead by the measurement and the apparatus. This conclusion is drawn from a comparison with a measurement of a two-level microwave transition in the same system. Additionally, evidence was provided for useful low-field hyperfine transitions or, in a related way, faster hyperfine manipulations. These results are supported by simulated models of the measurements, which confirm the conclusions made based on the experimental measurements. One clear extension of this all-microwave manipulation study would be the use of circularly polarized microwaves in the implementation of a tripod transition, a topic also presented in this thesis. This falls within the category of viable *Future Work*. Additionally,

the field orientation of the microwave antenna was a surprise in this experiment. The orientation of the k -vector measured by the atoms was offset by 50° from the expectation, a detail that is additionally unexpected since measurements made with this antenna indicated very high circular polarization quality. This problem should be studied or solved if these methods are to be extended to the tripod transition, which requires a second, co-aligned microwave field.

6.2 The Tripod

A discussion of the tripod transition for arbitrary control of the spin-1 state provided theoretical and experimental insight into this scheme. The results from the tripod attempt were presented for posterity, and could provide inspiration (*...or caution...*) for similar problems elsewhere. A careful selection of window to preserve the polarization of the optical field for the light shift could be beneficial, perhaps allowing for a successful implementation of the differential light shift with a smaller detuning. Additionally, the multi-tone microwave setup had some shortcomings as well which are likely tractable problems if deemed worth pursuing. The tone generation method for the tripod could alternatively be implemented using separate amplifiers and perhaps combining the tones using a power combiner if a single antenna is desired. An improved implementation scheme of the tripod can be envisioned with the use of dual-handedness of circular polarization microwave fields.

6.3 The End.

It is my hope that this study provides the information and impetus necessary for the groups working in similar systems to implement such microwave tools. This might help in the pursuit of simple, yet fully-arbitrary quantum state control of hyperfine states.

Appendices

APPENDIX A
THE MAGNETIC DIPOLE TRANSITION MATRICES

This appendix contains all the magnetic dipole transition matrices $\langle F, m_F | \Sigma_i | F', m'_F \rangle$, as described in Chapter 3 of the thesis.

$$\langle F, m_F | \Sigma_z | F', m'_F \rangle = \begin{pmatrix} \frac{1}{2} & 0 & 0 & 0 & -\frac{\sqrt{3}}{2} & 0 & 0 & 0 \\ 0 & 0 & 0 & 0 & 0 & -1 & 0 & 0 \\ 0 & 0 & -\frac{1}{2} & 0 & 0 & 0 & -\frac{\sqrt{3}}{2} & 0 \\ 0 & 0 & 0 & -1 & 0 & 0 & 0 & 0 \\ -\frac{\sqrt{3}}{2} & 0 & 0 & 0 & -\frac{1}{2} & 0 & 0 & 0 \\ 0 & -1 & 0 & 0 & 0 & 0 & 0 & 0 \\ 0 & 0 & -\frac{\sqrt{3}}{2} & 0 & 0 & 0 & \frac{1}{2} & 0 \\ 0 & 0 & 0 & 0 & 0 & 0 & 0 & 1 \end{pmatrix}$$

$$\langle F, m_F | \Sigma_x | F', m'_F \rangle = \begin{pmatrix} 0 & -\frac{1}{2\sqrt{2}} & 0 & -\frac{\sqrt{3}}{2} & 0 & \frac{1}{2\sqrt{2}} & 0 & 0 \\ -\frac{1}{2\sqrt{2}} & 0 & -\frac{1}{2\sqrt{2}} & 0 & -\frac{\sqrt{3}}{2} & 0 & \frac{\sqrt{3}}{2} & 0 \\ 0 & -\frac{1}{2\sqrt{2}} & 0 & 0 & 0 & -\frac{1}{2\sqrt{2}} & 0 & \frac{\sqrt{3}}{2} \\ -\frac{\sqrt{3}}{2} & 0 & 0 & 0 & \frac{1}{2} & 0 & 0 & 0 \\ 0 & -\frac{\sqrt{3}}{2} & 0 & \frac{1}{2} & 0 & \frac{\sqrt{3}}{2} & 0 & 0 \\ \frac{1}{2\sqrt{2}} & 0 & -\frac{1}{2\sqrt{2}} & 0 & \frac{\sqrt{3}}{2} & 0 & \frac{\sqrt{3}}{2} & 0 \\ 0 & \frac{\sqrt{3}}{2} & 0 & 0 & 0 & \frac{\sqrt{3}}{2} & 0 & \frac{1}{2} \\ 0 & 0 & \frac{\sqrt{3}}{2} & 0 & 0 & 0 & \frac{1}{2} & 0 \end{pmatrix}$$

$$\langle F, m_F | \Sigma_y | F', m'_F \rangle =$$

$$\begin{pmatrix} 0 & -\frac{i}{2\sqrt{2}} & 0 & \frac{i\sqrt{3}}{2} & 0 & \frac{i}{2\sqrt{2}} & 0 & 0 \\ \frac{i}{2\sqrt{2}} & 0 & -\frac{i}{2\sqrt{2}} & 0 & \frac{1}{2}i\sqrt{\frac{3}{2}} & 0 & \frac{1}{2}i\sqrt{\frac{3}{2}} & 0 \\ 0 & \frac{i}{2\sqrt{2}} & 0 & 0 & 0 & \frac{i}{2\sqrt{2}} & 0 & \frac{i\sqrt{3}}{2} \\ -\frac{i\sqrt{3}}{2} & 0 & 0 & 0 & \frac{i}{2} & 0 & 0 & 0 \\ 0 & -\frac{1}{2}i\sqrt{\frac{3}{2}} & 0 & -\frac{i}{2} & 0 & \frac{1}{2}i\sqrt{\frac{3}{2}} & 0 & 0 \\ -\frac{i}{2\sqrt{2}} & 0 & -\frac{i}{2\sqrt{2}} & 0 & -\frac{1}{2}i\sqrt{\frac{3}{2}} & 0 & \frac{1}{2}i\sqrt{\frac{3}{2}} & 0 \\ 0 & -\frac{1}{2}i\sqrt{\frac{3}{2}} & 0 & 0 & 0 & -\frac{1}{2}i\sqrt{\frac{3}{2}} & 0 & \frac{i}{2} \\ 0 & 0 & -\frac{i\sqrt{3}}{2} & 0 & 0 & 0 & -\frac{i}{2} & 0 \end{pmatrix}$$

APPENDIX B
TEMPORAL DARK MOT SEQUENCE

A temporal dark MOT sequence is used to load atoms from the MOT into the CO₂ laser trap. This involves several steps including decreasing the MOT magnetic field gradient, decreasing the repump laser power, and increasing the detuning of the cycling laser from the $F = 2 \rightarrow F' = 3$ cycling transition. This sequence has been empirically determined based on the temperature and number of atoms loaded into the dipole trap. The currently used sequence is shown in a time line in Figure B.1. The times are given as they are in the operation of our experimental sequence. The MOT is on for 15 s prior to the zero-time of this time line, and the dipole trap is loaded at 310 ms.

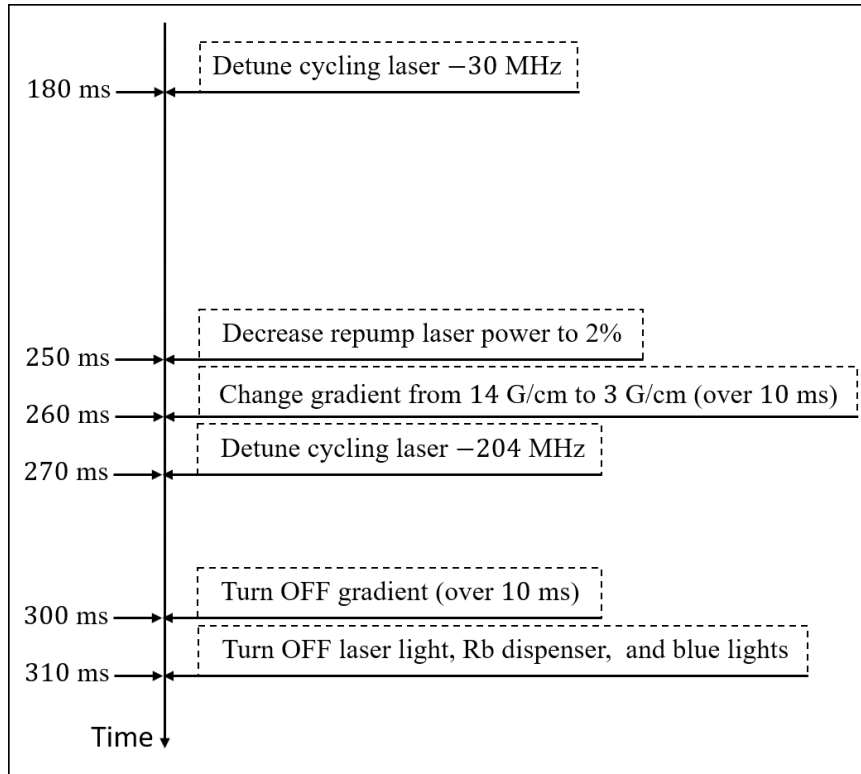


Figure B.1: A time line showing the multiple steps involved in the temporal dark MOT sequence

APPENDIX C

CIRCUITS USED IN APPARATUS

C.1 IGBT Circuit

The experiment uses IGBTs to rapidly switch ON and OFF the current for the Stern-Gerlach gradient coils. In order to safely operate the IGBTs with an inductive load (like the gradient coils), it is necessary to deal with the inductive kickback. We chose to use a circuit with a varistor to dissipate the flyback current, as well as a large flyback diode. For this flyback diode, we actually used the freewheeling diode from a previous IGBT module what was damaged due to misuse and improper handling of the inductive load. The circuit for this IGBT setup is shown schematically in figure C.1.

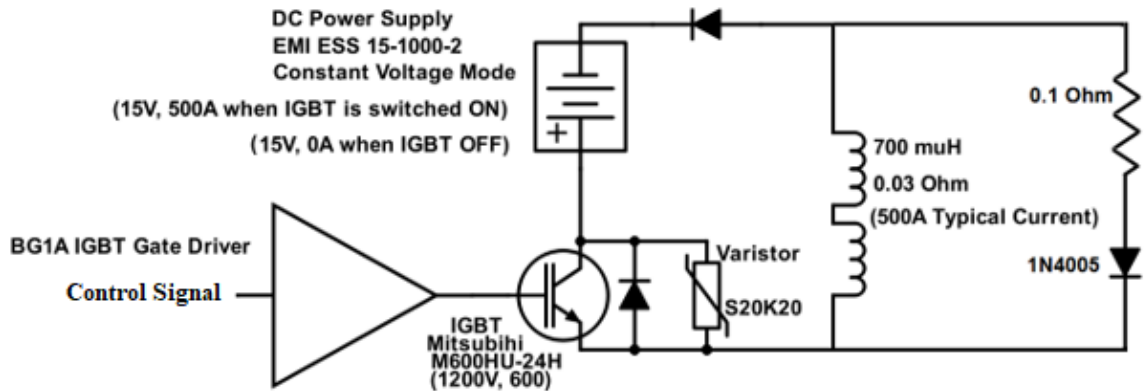


Figure C.1: IGBT circuit, including Stern-Gerlach gradient coils as the inductive load.

A current probe was used to measure the switching time for this IGBT circuit. The measurement of this switching time is shown in Figure C.2. This figure shows a measurement of 400 A of current switched off in about 1 ms.

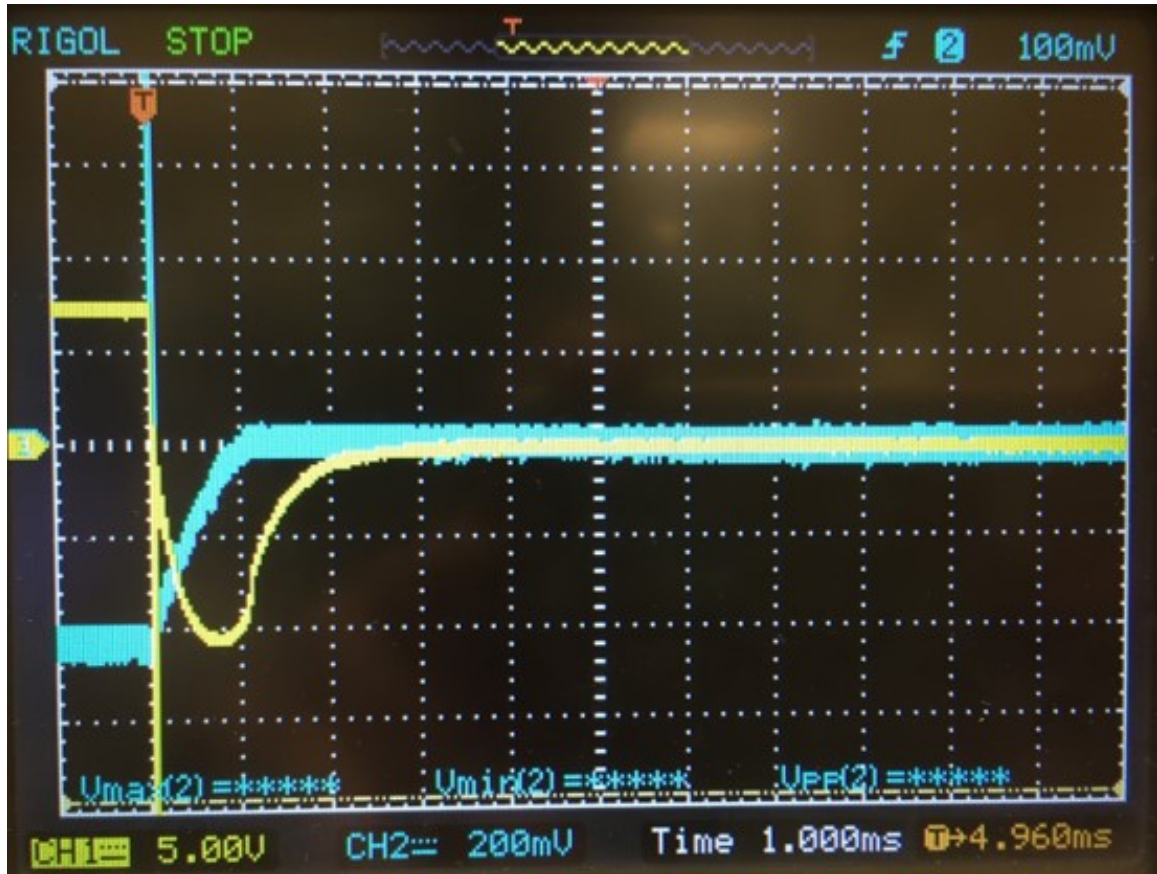


Figure C.2: An oscilloscope trace of a measurement of the current in the Stern-Gerlach coils switched off with the IGBT circuit. The current, measured with a current probe, is the blue trace (CH2) with 1 mV corresponding to 1 mA.

The IGBT circuit includes a shunt for the negative flyback on shut off. The resistor (along with the coil inductance) sets the decay time scale. For a LR series circuit, $V e^{-RLt}$. This diode-resistor shunt decreases the shut off time by about a factor of 4, compared to switching without this shunt.

Note that due to the finite lifetime of varistors and their very low cost, we replace the varistor periodically about once a month.

C.2 60Hz Line Trigger

The experiment is triggered off the 60 Hz AC line cycle. The result is a more stable experiment with less fluctuation in the magnetic field at the experiment time. This is accomplished by triggering one of the cards in a RTSI configuration to synchronize the NI-DAQ cards that control the apparatus. The trigger signal is generated by a simple circuit which generates a 5 V square wave from the 60 Hz signal. The circuit is as shown in figure

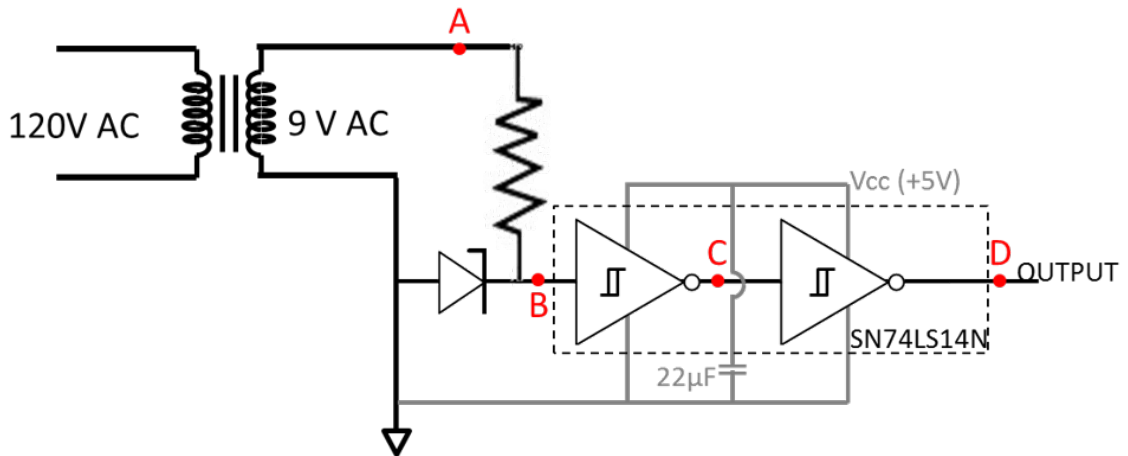


Figure C.3: 60Hz line trigger circuit.

The approximate waveform as it would be measured at several points in the circuit is shown in below in Figure C.4.

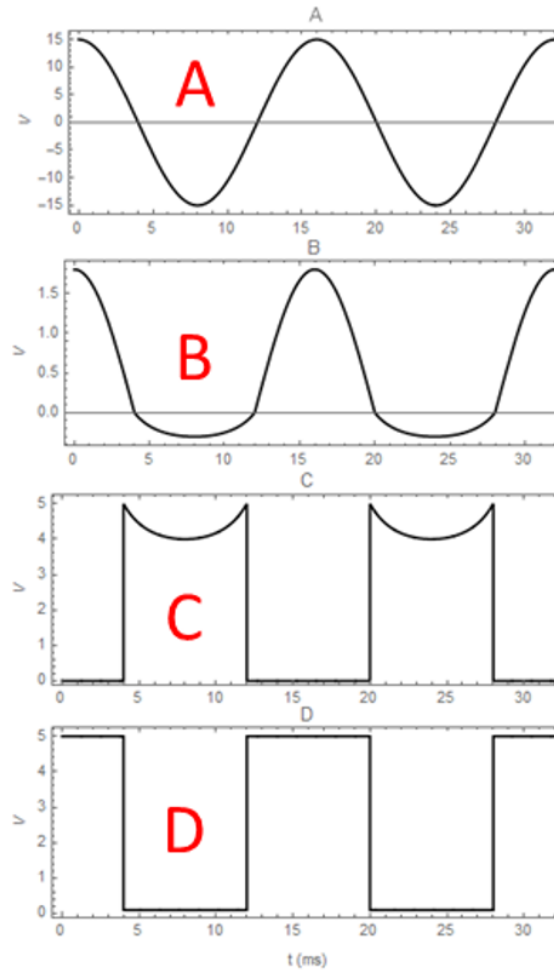


Figure C.4: The approximate waveform at several points in the 60Hz line trigger circuit. The letters correspond to probe locations lettered similarly in Figure C.3.

C.3 Unity Gain Buffer Circuit

This simple circuit was designed to increase the input impedance of the analog control input for a couple of devices in the lab (e.g. acousto-optical modulator (AOM) drivers). This is a step that was taken to mitigate ground loops between devices in the lab. The connections are quite simple. The input BNC signal pin is connected to $V_{IN,+}$ and the input BNC shield is connected to $V_{IN,-}$. The circuit is powered with a bipolar DC supply. The ground of the supply voltage is tied to the output ground (“Device GND”). The output, which is

connected to the device (e.g. AOM driver input), is connected to the “Device Signal” and “Device GND” pins. The device ground is also tied to the Device GND connection.

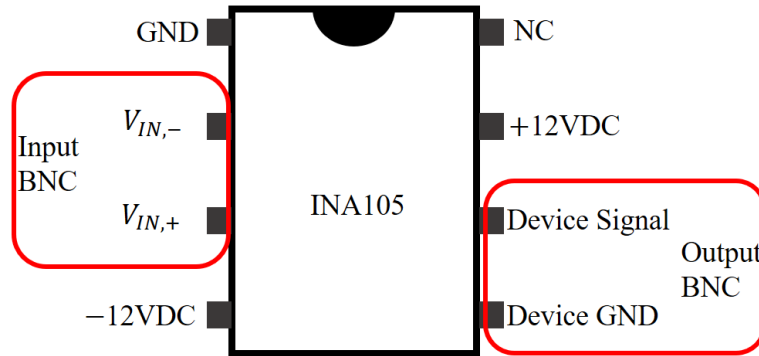


Figure C.5: Connections for the unity-gain buffer circuit.

C.4 Slave Laser Current Modulation Circuit

The main cycling-transition laser for the experiments uses an injection-locked slave laser which is varied in frequency using seed light that is frequency shifted with an acousto-optical modulator (AOM). This circuit is a small proportional amplifier which varies the slave laser current in proportion to the frequency shift. The frequency shift is set by the voltage on a voltage-controlled oscillator (VCO) which is the frequency source for the AOM. This circuit uses this VCO control voltage as its input and the output is connected to the current modulation input for the slave laser. The circuit is shown in Figure C.6. The gain is adjustable by swapping the resistor R_3 .

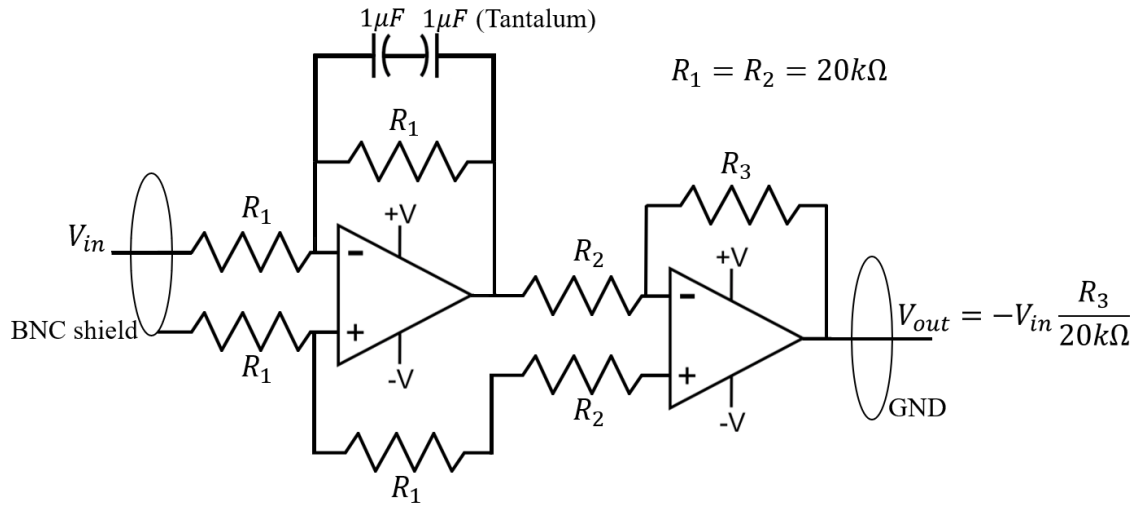


Figure C.6: The slave current modulation amplifier circuit.

APPENDIX D

FLUORESCENCE COLLECTION CALCULATION

Below are the calculations performed to estimate the conversion to number of atoms in a fluorescent measurement of the atom cloud. This gives a value for expected counts per atom, or “CPA”

$$\frac{CPA}{t_{probe}} = \left(\frac{\Gamma}{2}\right) \left(\frac{\Omega}{4\pi}\right) (\eta) (gain)$$

$$\frac{CPA}{t_{probe}} = \left(\frac{\Gamma}{2}\right) \left(\frac{(NA)^2}{4}\right) (\eta) (gain)$$

Γ is the transition linewidth for the D2 transition in ^{87}Rb

Ω is the solid angle subtended by the imaging lens

NA is alternatively the numerical aperture of the imaging lens

η is the quantum efficiency of the CCD sensor

$gain$ is the gain multiplier for the camera. Additionally other attenuations, such as for a line-filter or ND filter are multiplied here. Note: Our experiments use Andor cameras. There have been a few separate occasions when the value for the gain multiplier obtained from the Andor camera manual was misinterpreted is the inverse quantity.

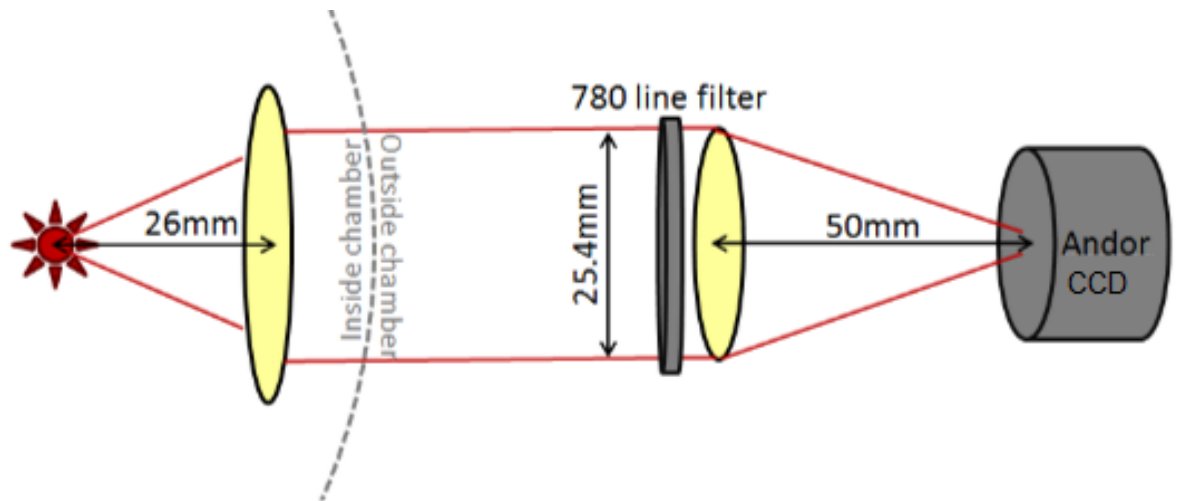


Figure D.1: A schematic of a fluorescence imaging setup used for an example calculation of the expected number of reported camera counts per atom. The atoms are represented schematically as the red dot on the left side. The lenses are shown schematically in yellow (black outline). Here, an example setup with a 50 mm (1" diameter) re-imaging lens and a 780 nm line filter in place. The current version of the apparatus typically uses a 100 mm (2" diameter) re-imaging lens and no line filter.

APPENDIX E

BAKEOUT PROCEDURE

A rather specific bakeout procedure was necessary for the BEC chamber used for the work in this thesis. This necessity arose from the conflict between needing ultra-high vacuum (UHV) for long lifetimes (longer than the evaporation timescale in the trap) and the limitations of the zinc-selenide viewports required for the CO₂ laser. Obtaining ultra-high vacuum at the level of E-11 torr required a bakeout of the vacuum components while the vacuum system is being pumped down. For the pumping, we used an in-house built pumping station consisting of a turbo pump, backed by a roughing pump, with an ion gauge and residual gas analyzer (RGA). A flexible metal bellows is used to connect this pumping station to the vacuum chamber for pumping. The vacuum chamber itself has an ion pump which is not used during this procedure. The magnets required for the ion pump operation preclude this, as their Curie temperature is too low.

For the “baking,” the chamber must be heated to a fairly uniform temperature to avoid leaks resulting from thermal stresses. We like to use an oven (built in-house) with a circulating convection fan. We also sometimes use fiberglass heat tape and foil when not using the oven (e.g. if the chamber is installed in place on the optical table). Higher temperature bakes help significantly in obtaining UHV. Bakeout temperatures of 300° C to 400° C are used when the vacuum components allow. However, in the case of the zinc-selenide components, the maximum bakeout allowable was less than 200° C.

The best procedure found to reach UHV using these zinc-selenide viewports was a two-step bakeout. In the first step, the chamber was assembled without the zinc-selenide components. The zinc-selenide ports on the chamber were instead sealed with pyrex viewports or solid flanges, to be removed later. The chamber was baked at high temperature for as long as permissible (1-2 weeks). The levels of residual gas could be monitored during

this time via the RGA on the pump station to chose a suitable end condition. Following this bakeout, the chamber was vented with dry nitrogen and clean zinc-selenide components were installed, minimizing the exposure time of the chamber to atmosphere. Step two was a low temperature bakeout with the zinc-selenide components. This was a bakeout at about 150 degrees Celsius, again for 1 to 2 weeks with the residual gasses monitored.

REFERENCES

- [1] M. H. Anderson, J. R. Ensher, M. R. Matthews, C. E. Wieman, and E. A. Cornell, “Observation of bose-einstein condensation in a dilute atomic vapor,” *Science*, vol. 269, no. 5221, pp. 198–201, 1995.
- [2] K. B. Davis, M. O. Mewes, M. R. Andrews, N. J. van Druten, D. S. Durfee, D. M. Kurn, and W. Ketterle, “Bose-einstein condensation in a gas of sodium atoms,” *Phys. Rev. Lett.*, vol. 75, pp. 3969–3973, 22 1995.
- [3] E. L. Raab, M. Prentiss, A. Cable, S. Chu, and D. E. Pritchard, “Trapping of neutral sodium atoms with radiation pressure,” *Phys. Rev. Lett.*, vol. 59, pp. 2631–2634, 23 1987.
- [4] W. D. Phillips, “Nobel lecture: Laser cooling and trapping of neutral atoms,” *Rev. Mod. Phys.*, vol. 70, pp. 721–741, 3 1998.
- [5] J. Dalibard and C. Cohen-Tannoudji, “Laser cooling below the doppler limit by polarization gradients: Simple theoretical models,” *J. Opt. Soc. Am. B*, vol. 6, no. 11, pp. 2023–2045, 1989.
- [6] M. R. Andrews, C. G. Townsend, H.-J. Miesner, D. S. Durfee, D. M. Kurn, and W. Ketterle, “Observation of interference between two bose condensates,” *Science*, vol. 275, no. 5300, pp. 637–641, 1997.
- [7] I. Bloch, T. W. Hänsch, and T. Esslinger, “Measurement of the spatial coherence of a trapped bose gas at the phase transition,” *Nature*, vol. 403, no. 6766, pp. 166–170, 2000.
- [8] M.-O. Mewes, M R. Andrews, D M. Kurn, D. Durfee, C G. Townsend, and W Ketterle, “Output coupler for bose-einstein condensed atoms,” *Physical Review Letters*, vol. 78, pp. 582–585, Jan. 1997.
- [9] E. W. Hagley, L. Deng, M. Kozuma, J. Wen, K. Helmerson, S. L. Rolston, and W. D. Phillips, “A well-collimated quasi-continuous atom laser,” *Science*, vol. 283, no. 5408, pp. 1706–1709, 1999.
- [10] I. Bloch, T. W. Hänsch, and T. Esslinger, “Atom laser with a cw output coupler,” *Phys. Rev. Lett.*, vol. 82, pp. 3008–3011, 15 1999.

- [11] C. J. Myatt, E. A. Burt, R. W. Ghrist, E. A. Cornell, and C. E. Wieman, “Production of two overlapping bose-einstein condensates by sympathetic cooling,” *Phys. Rev. Lett.*, vol. 78, pp. 586–589, 4 1997.
- [12] E. A. Cornell, D. S. Hall, M. R. Matthews, and C. E. Wieman, “Having it both ways: Distinguishable yet phase-coherent mixtures of bose-einstein condensates,” *Journal of Low Temperature Physics*, vol. 113, no. 3, pp. 151–165, 1998.
- [13] D. M. Stamper-Kurn, M. R. Andrews, A. P. Chikkatur, S. Inouye, H.-J. Miesner, J. Stenger, and W. Ketterle, “Optical confinement of a bose-einstein condensate,” *Phys. Rev. Lett.*, vol. 80, pp. 2027–2030, 10 1998.
- [14] M. D. Barrett, J. A. Sauer, and M. S. Chapman, “All-optical formation of an atomic bose-einstein condensate,” *Phys. Rev. Lett.*, vol. 87, p. 010404, 1 2001.
- [15] H.-J. Miesner, D. M. Stamper-Kurn, J. Stenger, S. Inouye, A. P. Chikkatur, and W. Ketterle, “Observation of metastable states in spinor bose-einstein condensates,” *Phys. Rev. Lett.*, vol. 82, pp. 2228–2231, 11 1999.
- [16] D. M. Stamper-Kurn, H.-J. Miesner, A. P. Chikkatur, S. Inouye, J. Stenger, and W. Ketterle, “Quantum tunneling across spin domains in a bose-einstein condensate,” *Phys. Rev. Lett.*, vol. 83, pp. 661–665, 4 1999.
- [17] Y. Kawaguchi and M. Ueda, “Spinor bose–einstein condensates,” *Physics Reports*, vol. 520, no. 5, pp. 253–381, 2012, Spinor Bose–Einstein condensates.
- [18] D. M. Stamper-Kurn and M. Ueda, “Spinor bose gases: Symmetries, magnetism, and quantum dynamics,” *Rev. Mod. Phys.*, vol. 85, pp. 1191–1244, 3 2013.
- [19] M.-S. Chang, C. D. Hamley, M. D. Barrett, J. A. Sauer, K. M. Fortier, W. Zhang, L. You, and M. S. Chapman, “Observation of spinor dynamics in optically trapped ^{87}Rb bose-einstein condensates,” *Phys. Rev. Lett.*, vol. 92, p. 140403, 14 2004.
- [20] W. Zhang, D. L. Zhou, M.-S. Chang, M. S. Chapman, and L. You, “Coherent spin mixing dynamics in a spin-1 atomic condensate,” *Phys. Rev. A*, vol. 72, p. 013602, 1 2005.
- [21] M.-S. Chang, Q. Qin, W. Zhang, L. You, and M. S. Chapman, “Coherent spinor dynamics in a spin-1 bose condensate,” *Nature Physics*, vol. 1, no. 2, pp. 111–116, 2005.
- [22] E. M. Bookjans, C. D. Hamley, and M. S. Chapman, “Strong quantum spin correlations observed in atomic spin mixing,” *Phys. Rev. Lett.*, vol. 107, p. 210406, 21 2011.

- [23] C. D. Hamley and et. al., “Spin-nematic squeezed vacuum in a quantum gas,” *Nat. Phys.*, vol. 8, pp. 305–308, 208 2012.
- [24] L. Pezzè, A. Smerzi, M. K. Oberthaler, R. Schmied, and P. Treutlein, “Quantum metrology with nonclassical states of atomic ensembles,” *Rev. Mod. Phys.*, vol. 90, p. 035 005, 3 2018.
- [25] O. Hosten, N. J. Engelsen, R. Krishnakumar, and M. A. Kasevich, “Measurement noise 100 times lower than the quantum-projection limit using entangled atoms,” *Nature*, vol. 529, 505 EP –, 2016.
- [26] I. Kruse, K. Lange, J. Peise, B. Lücke, L. Pezzè, J. Arlt, W. Ertmer, C. Lisdat, L. Santos, A. Smerzi, and C. Klempt, “Improvement of an atomic clock using squeezed vacuum,” *Phys. Rev. Lett.*, vol. 117, p. 143 004, 14 2016.
- [27] R. J. Sewell, M. Koschorreck, M. Napolitano, B. Dubost, N. Behbood, and M. W. Mitchell, “Magnetic sensitivity beyond the projection noise limit by spin squeezing,” *Phys. Rev. Lett.*, vol. 109, p. 253 605, 25 2012.
- [28] W. Muessel, H. Strobel, D. Linnemann, D. B. Hume, and M. K. Oberthaler, “Scalable spin squeezing for quantum-enhanced magnetometry with bose-einstein condensates,” *Phys. Rev. Lett.*, vol. 113, p. 103 004, 10 2014.
- [29] C. S. Gerving, T. M. Hoang, B. J. Land, M. Anquez, C. D. Hamley, and M. S. Chapman, “Non-equilibrium dynamics of an unstable quantum pendulum explored in a spin-1 bose-einstein condensate,” *Nature Communications*, vol. 3, 1169 EP –, 2012, Article.
- [30] B. Lücke, J. Peise, G. Vitagliano, J. Arlt, L. Santos, G. Tóth, and C. Klempt, “Detecting multiparticle entanglement of dicke states,” *Phys. Rev. Lett.*, vol. 112, p. 155 304, 15 2014.
- [31] Y.-Q. Zou, L.-N. Wu, Q. Liu, X.-Y. Luo, S.-F. Guo, J.-H. Cao, M. K. Tey, and L. You, “Beating the classical precision limit with spin-1 dicke states of more than 10,000 atoms,” *Proceedings of the National Academy of Sciences*, vol. 115, no. 25, pp. 6381–6385, 2018.
- [32] Z Zhang and L. M. Duan, “Quantum metrology with dicke squeezed states,” *New Journal of Physics*, vol. 16, no. 10, p. 103 037, 2014.
- [33] G. Vitagliano, I. Apellaniz, M. Kleinmann, B. Lücke, C. Klempt, and G. Tóth, “Entanglement and extreme spin squeezing of unpolarized states,” *New Journal of Physics*, vol. 19, no. 1, p. 013 027, 2017.

- [34] X.-Y. Luo, Y.-Q. Zou, L.-N. Wu, Q. Liu, M.-F. Han, M. K. Tey, and L. You, “Deterministic entanglement generation from driving through quantum phase transitions,” *Science*, vol. 355, no. 6325, pp. 620–623, 2017.
- [35] Y.-A. Chen, X.-H. Bao, Z.-S. Yuan, S. Chen, B. Zhao, and J.-W. Pan, “Heralded generation of an atomic noon state,” *Phys. Rev. Lett.*, vol. 104, p. 043 601, 4 2010.
- [36] N. Friis, O. Marty, C. Maier, C. Hempel, M. Holzäpfel, P. Jurcevic, M. B. Plenio, M. Huber, C. Roos, R. Blatt, and B. Lanyon, “Observation of entangled states of a fully controlled 20-qubit system,” *Phys. Rev. X*, vol. 8, p. 021 012, 2 2018.
- [37] X.-L. Wang, L.-K. Chen, W. Li, H.-L. Huang, C. Liu, C. Chen, Y.-H. Luo, Z.-E. Su, D. Wu, Z.-D. Li, H. Lu, Y. Hu, X. Jiang, C.-Z. Peng, L. Li, N.-L. Liu, Y.-A. Chen, C.-Y. Lu, and J.-W. Pan, “Experimental ten-photon entanglement,” *Phys. Rev. Lett.*, vol. 117, p. 210 502, 21 2016.
- [38] R. McConnell, H. Zhang, J. Hu, S. Cuk, and V. Vuletic, “Entanglement with negative wigner function of almost 3,000 atoms heralded by one photon,” *Nature*, vol. 519, 439 EP –, 2015.
- [39] K. Lange, J. Peise, B. Lücke, I. Kruse, G. Vitagliano, I. Apellaniz, M. Kleinmann, G. Tóth, and C. Klempt, “Entanglement between two spatially separated atomic modes,” *Science*, vol. 360, no. 6387, pp. 416–418, 2018.
- [40] D. J. Wineland, J. J. Bollinger, W. M. Itano, and D. J. Heinzen, “Squeezed atomic states and projection noise in spectroscopy,” *Phys. Rev. A*, vol. 50, pp. 67–88, 1 1994.
- [41] O. E. Müstecaplıoğlu, M. Zhang, and L. You, “Spin squeezing and entanglement in spinor condensates,” *Phys. Rev. A*, vol. 66, p. 033 611, 3 2002.
- [42] L.-M. Duan, J. I. Cirac, and P. Zoller, “Quantum entanglement in spinor bose-einstein condensates,” *Phys. Rev. A*, vol. 65, p. 033 619, 3 2002.
- [43] A. Sørensen, L.-M. Duan, J. I. Cirac, and P. Zoller, “Many-particle entanglement with bose-einstein condensates,” *Nature*, vol. 409, no. 6816, pp. 63–66, 2001.
- [44] G. Vitagliano, P. Hyllus, I. n. L. Egusquiza, and G. Tóth, “Spin squeezing inequalities for arbitrary spin,” *Phys. Rev. Lett.*, vol. 107, p. 240 502, 24 2011.
- [45] H. Strobel, W. Muessel, D. Linnemann, T. Zibold, D. B. Hume, L. Pezzè, A. Smerzi, and M. K. Oberthaler, “Fisher information and entanglement of non-gaussian spin states,” *Science*, vol. 345, no. 6195, pp. 424–427, 2014.

- [46] J. Goold, L. Heaney, T. Busch, and V. Vedral, “Detection and engineering of spatial mode entanglement with ultracold bosons,” *Phys. Rev. A*, vol. 80, p. 022 338, 2 2009.
- [47] P. Kunkel, M. Prüfer, H. Strobel, D. Linnemann, A. Frölian, T. Gasenzer, M. Gärttner, and M. K. Oberthaler, “Spatially distributed multipartite entanglement enables epr steering of atomic clouds,” *Science*, vol. 360, no. 6387, pp. 413–416, 2018.
- [48] M. Fadel, T. Zibold, B. Décamps, and P. Treutlein, “Spatial entanglement patterns and einstein-podolsky-rosen steering in bose-einstein condensates,” *Science*, vol. 360, no. 6387, pp. 409–413, 2018.
- [49] A. Einstein, B. Podolsky, and N. Rosen, “Can quantum-mechanical description of physical reality be considered complete?” *Phys. Rev.*, vol. 47, pp. 777–780, 10 1935.
- [50] M. D. Reid, “Demonstration of the einstein-podolsky-rosen paradox using nondegenerate parametric amplification,” *Phys. Rev. A*, vol. 40, pp. 913–923, 2 1989.
- [51] A. Peres, *Quantum Theory: Concepts and Methods*, ser. Fundamental Theories of Physics. Springer Netherlands, 1995, ISBN: 9780792336327.
- [52] G. M. Huang, T. J. Tarn, and J. W. Clark, “On the controllability of quantum-mechanical systems,” *Journal of Mathematical Physics*, vol. 24, no. 11, pp. 2608–2618, 1983.
- [53] H. M. Bharath, “Geometry, topology and control of spin-1 quantum systems,” PhD thesis, Georgia Institute of Technology, 2018.
- [54] P. Kunkel, M. Prüfer, S. Lannig, R. Rosa-Medina, A. Bonnin, M. Gärttner, H. Strobel, and M. K. Oberthaler, “Simultaneous readout of noncommuting collective spin observables beyond the standard quantum limit,” *arXiv preprint arXiv:1904.01471*, 2019.
- [55] I. I. Rabi, “Space quantization in a gyrating magnetic field,” *Phys. Rev.*, vol. 51, pp. 652–654, 8 1937.
- [56] J. J. Sakurai and J. Napolitano, *Modern Quantum Mechanics*, 2nd ed. Cambridge University Press, 2017.
- [57] B. W. Shore, “Two-state behavior in n-state quantum systems: The morris–shore transformation reviewed,” *Journal of Modern Optics*, vol. 61, no. 10, pp. 787–815, 2014.

- [58] P. A. Ivanov, N. V. Vitanov, and K. Bergmann, “Spontaneous emission in stimulated raman adiabatic passage,” *Phys. Rev. A*, vol. 72, p. 053 412, 5 2005.
- [59] A. F. Linskens, I. Holleman, N. Dam, and J. Reuss, “Two-photon rabi oscillations,” *Phys. Rev. A*, vol. 54, pp. 4854–4862, 6 1996.
- [60] C. Foot, *Atomic physics*, ser. Oxford master series in physics. Oxford University Press, 2005, ISBN: 9780198506966.
- [61] J. Bateman, A. Xuereb, and T. Freearge, “Stimulated raman transitions via multiple atomic levels,” *Phys. Rev. A*, vol. 81, p. 043 808, 4 2010.
- [62] C. Monroe, D. M. Meekhof, B. E. King, W. M. Itano, and D. J. Wineland, “Demonstration of a fundamental quantum logic gate,” *Phys. Rev. Lett.*, vol. 75, pp. 4714–4717, 25 1995.
- [63] M. A. Rowe, D. Kielpinski, V. Meyer, C. A. Sackett, W. M. Itano, C. Monroe, and D. J. Wineland, “Experimental violation of a bell’s inequality with efficient detection,” *Nature*, vol. 409, no. 6822, pp. 791–794, 2001.
- [64] G. K. Brennen, C. M. Caves, P. S. Jessen, and I. H. Deutsch, “Quantum logic gates in optical lattices,” *Phys. Rev. Lett.*, vol. 82, pp. 1060–1063, 5 1999.
- [65] A. Imamoglu, D. D. Awschalom, G. Burkard, D. P. DiVincenzo, D. Loss, M. Sherwin, and A. Small, “Quantum information processing using quantum dot spins and cavity qed,” *Phys. Rev. Lett.*, vol. 83, pp. 4204–4207, 20 1999.
- [66] U. Gaubatz, P. Rudecki, S. Schiemann, and K. Bergmann, “Population transfer between molecular vibrational levels by stimulated raman scattering with partially overlapping laser fields. a new concept and experimental results,” *The Journal of Chemical Physics*, vol. 92, no. 9, pp. 5363–5376, 1990.
- [67] E. Sjöqvist, D. M. Tong, L. M. Andersson, B. Hessmo, M. Johansson, and K. Singh, “Non-adiabatic holonomic quantum computation,” *New Journal of Physics*, vol. 14, no. 10, p. 103 035, 2012.
- [68] E. Sjöqvist, “Nonadiabatic holonomic single-qubit gates in off-resonant Λ systems,” *Physics Letters A*, vol. 380, no. 1, pp. 65 –67, 2016.
- [69] P. Zanardi and M. Rasetti, “Holonomic quantum computation,” *Physics Letters A*, vol. 264, no. 2, pp. 94 –99, 1999.
- [70] L.-M. Duan, J. I. Cirac, and P. Zoller, “Geometric manipulation of trapped ions for quantum computation,” *Science*, vol. 292, no. 5522, pp. 1695–1697, 2001.

- [71] A. A. Abdumalikov Jr, J. M. Fink, K. Juliusson, M. Pechal, S. Berger, A. Wallraff, and S. Filipp, “Experimental realization of non-abelian non-adiabatic geometric gates,” *Nature*, vol. 496, 482 EP –, 2013.
- [72] C. Zu, W.-B. Wang, L. He, W.-G. Zhang, C.-Y. Dai, F. Wang, and L.-M. Duan, “Experimental realization of universal geometric quantum gates with solid-state spins,” *Nature*, vol. 514, 72 EP –, 2014.
- [73] Y. Sekiguchi, N. Niikura, R. Kuroiwa, H. Kano, and H. Kosaka, “Optical holonomic single quantum gates with a geometric spin under a zero field,” *Nature Photonics*, vol. 11, 309 EP –, 2017, Article.
- [74] D. Møller, L. B. Madsen, and K. Mølmer, “Geometric phase gates based on stimulated raman adiabatic passage in tripod systems,” *Phys. Rev. A*, vol. 75, p. 062 302, 6 2007.
- [75] F. Leroux, K. Pandey, R. Rehbi, F. Chevy, C. Miniatura, B. Grémaud, and D. Wilkowski, “Non-abelian adiabatic geometric transformations in a cold strontium gas,” *Nature Communications*, vol. 9, no. 1, p. 3580, 2018.
- [76] S. T. Merkel, P. S. Jessen, and I. H. Deutsch, “Quantum control of the hyperfine-coupled electron and nuclear spins in alkali-metal atoms,” *Phys. Rev. A*, vol. 78, p. 023 404, 2 2008.
- [77] A Smith, B E. Anderson, H Sosa-Martinez, C. Riofrio, I. Deutsch, and P S. Jessen, “Quantum control in the cs $6s_{1/2}$ ground manifold using rf and μw magnetic fields,” Aug. 2013.
- [78] C. Hamley, “Spin-nematic squeezing in a bose-einstein condensate,” PhD thesis, Georgia Institute of Technology, 2012.
- [79] H. M. Bharath, M. Boguslawski, M. Barrios, L. Xin, and M. S. Chapman, “Singular loops and their non-abelian geometric phases in spin-1 ultracold atoms,” *arXiv preprint arXiv:1801.00586*, 2018.
- [80] M. D. Barrett, “A quest for bec : An all optical alternative,” PhD thesis, Georgia Institute of Technology, 2002.
- [81] M.-S. Chang, “Coherent spin dynamics of a spin-1 bose-einstein condensate,” PhD thesis, Georgia Institute of Technology, 2006.
- [82] T. Hoang, “Quantum control of a many-body system in a spin-1 bose-einstein condensate,” PhD thesis, Georgia Institute of Technology, 2013.

- [83] M. Anquez, “Kibble-zurek mechanism in a spin-1 bose-einstein condensate,” PhD thesis, Georgia Institute of Technology, 2015.
- [84] H. J. Metcalf and P. van der Straten, *Laser Cooling and Trapping*. Springer, New York, 1999.
- [85] C. Klempt, T. van Zoest, T. Henninger, O. Topic, E. Rasel, W. Ertmer, and J. Arlt, “Ultraviolet light-induced atom desorption for large rubidium and potassium magneto-optical traps,” *Phys. Rev. A*, vol. 73, p. 013410, 1 2006.
- [86] E. Bookjans, “Relative number squeezing in a spin-1 bose-einstein condensate,” PhD thesis, Georgia Institute of Technology, 2010.
- [87] C. A. Balanis, *Antenna Theory: Analysis and Design (3rd ed.)* John Wiley and Sons, Inc., 2005.
- [88] R. Wakabayashi, K. Shimada, H. Kawakami, and G. Sato, “Circularly polarized log-periodic dipole antenna for emi measurements,” *IEEE Transactions on Electromagnetic Compatibility*, vol. 41, no. 2, pp. 93–99, 1999.
- [89] K. S. Raja, C. Kathiravan, R. Ramesh, M. Rajalingam, and I. V. Barve, “Design and performance of a low-frequency cross-polarized log-periodic dipole antenna,” *The Astrophysical Journal Supplement Series*, vol. 207, no. 1, p. 2, 2013.
- [90] E. M. Turner, *Spiral slot antenna*, US Patent, US2863145A, 1955.
- [91] H. H. Tran and T. T. Le, “Ultrawideband, high-gain, high-efficiency, circularly polarized archimedean spiral antenna,” *AEU - International Journal of Electronics and Communications*, vol. 109, pp. 1–7, 2019.
- [92] R. J. M. John D. Kraus, *Antennas for All Applications*. McGraw-Hill, 2002.
- [93] H. King and J. Wong, “Characteristics of 1 to 8 wavelength uniform helical antennas,” *IEEE Transactions on Antennas and Propagation*, vol. 28, no. 2, pp. 291–296, 1980.
- [94] H. Nakano, H. Takeda, T. Honma, H. Mimaki, and J. Yamauchi, “Extremely low-profile helix radiating a circularly polarized wave,” *IEEE Transactions on Antennas and Propagation*, vol. 39, no. 6, pp. 754–757, 1991.
- [95] Z.-H. Wu and E. K. N. Yung, “Short helical antenna with extremely small pitch angle,” *Microwave and Optical Technology Letters*, vol. 49, no. 1, pp. 17–19, 2007.

- [96] S. Fu, Y. Cao, Y. Zhou, and S. Fang, “Improved low-profile helical antenna design for inmarsat applications,” *International Journal of Antennas and Propagation*, vol. 2012, no. 829371, pp. 1–5, 2012.
- [97] U. R. Kraft and G. Monich, “Main-beam polarization properties of modified helical antennas,” *IEEE Transactions on Antennas and Propagation*, vol. 38, no. 5, pp. 589–597, 1990.
- [98] C. D. Bruzewicz, J. Chiaverini, R. McConnell, and J. M. Sage, “Trapped-ion quantum computing: Progress and challenges,” *Applied Physics Reviews*, vol. 6, no. 2, p. 021 314, 2019.
- [99] G. E. Marti, R. B. Hutson, A. Goban, S. L. Campbell, N. Poli, and J. Ye, “Imaging optical frequencies with 100 μ hz precision and 1.1 μ m resolution,” *Phys. Rev. Lett.*, vol. 120, p. 103 201, 10 2018.
- [100] W. Muessel, H. Strobel, D. Linnemann, T. Zibold, B. Juliá-Díaz, and M. K. Oberthaler, “Twist-and-turn spin squeezing in bose-einstein condensates,” *Phys. Rev. A*, vol. 92, p. 023 603, 2 2015.
- [101] C. H. Townes and A. L. Schawlow, *Microwave spectroscopy*. Dover Publications, 1975.
- [102] J. R. Eshbach and M. W. P. Strandberg, “Apparatus for zeeman effect measurements on microwave spectra,” *Review of Scientific Instruments*, vol. 23, pp. 623–628, 1952.
- [103] J. R. Eshbachand, R. E. Hillger, and M. W. Strandberg, “The nuclear magnetic moment of s³³ from microwave spectroscopy,” *Physical Review*, vol. 85, pp. 532–539, Feb. 1952.
- [104] J. R. Eshbach and M. W. P. Strandberg, “Rotational magnetic moments of ¹ Σ molecules,” *Phys. Rev.*, vol. 85, pp. 24–34, 1 1952.
- [105] M. Mrózek, J. Mlynarczyk, D. S. Rudnicki, and W. Gawlik, “Circularly polarized microwaves for magnetic resonance study in the ghz range: Application to nitrogen-vacancy in diamonds,” *Applied Physics Letters*, vol. 107, no. 1, p. 013 505, 2015.
- [106] K. Nagata, K. Kuramitani, Y. Sekiguchi, and H. Kosaka, “Universal holonomic quantum gates over geometric spin qubits with polarised microwaves,” *Nature Communications*, vol. 9, no. 1, p. 3227, 2018.
- [107] A. Einstein, B. Podolsky, and N. Rosen, “Addressing spin transitions on ²⁰⁹Bi donors in silicon using circularly polarized microwaves,” *Phys. Rev.*, vol. 47, pp. 777–780, 10 1935.

- [108] J. Koepsell, T. Thiele, J. Deiglmayr, A. Wallraff, and F. Merkt, “Measuring the polarization of electromagnetic fields using rabi-rate measurements with spatial resolution: Experiment and theory,” *Phys. Rev. A*, vol. 95, p. 053 860, 5 2017.
- [109] T. Thiele, Y. Lin, M. O. Brown, and C. A. Regal, “Self-calibrating vector atomic magnetometry through microwave polarization reconstruction,” *Phys. Rev. Lett.*, vol. 121, p. 153 202, 15 2018.
- [110] D. A. Steck, “Sodium d line data,” Jan. 2003.
- [111] —, “Cesium d line data,” Jan. 2003.
- [112] —, “Rubidium 87 d line data,” Jan. 2003.
- [113] S Bize, Y Sortais, M. S Santos, C Mandache, A Clairon, and C Salomon, “High-accuracy measurement of the 87Rb ground-state hyperfine splitting in an atomic fountain,” *Europhysics Letters (EPL)*, vol. 45, no. 5, pp. 558–564, 1999.
- [114] P. J. Mohr and B. N. Taylor, “CODATA recommended values of the fundamental physical constants: 1998,” *Rev. Mod. Phys.*, vol. 72, pp. 351–495, 2 2000.
- [115] E. Arimondo, M. Inguscio, and P. Violino, “Experimental determinations of the hyperfine structure in the alkali atoms,” *Rev. Mod. Phys.*, vol. 49, pp. 31–75, 1 1977.
- [116] A. Corney, *Atomic and Laser Spectroscopy*. Oxford University Press, 1977.
- [117] J. M. Best, L. Clayton, J. H. Cook, H. L. Crispin, C. H. Currie, D. M. Fraley, R. A. Heaton, L. H. Hemming, T. G. Hickman, J. S. Hollis, S. F. Hutchins, T. J. Lyon, C. C. Morris, R. E. Pidgeon, and T. D. Smit, *Microwave Antenna Measurement*. Scientific-Atlanta, Inc., 1969.
- [118] P Solinas, M Sasseti, P Truini, and N Zanghì, “On the stability of quantum holonomic gates,” *New Journal of Physics*, vol. 14, no. 9, p. 093 006, 2012.
- [119] C. Weitenberg, M. Endres, J. F. Sherson, M. Cheneau, P. Schauß, T. Fukuhara, I. Bloch, and S. Kuhr, “Single-spin addressing in an atomic Mott insulator,” *Nature*, vol. 471, 319 EP –, 2011, Article.
- [120] R. Grimm, M. Weidemüller, and Y. B. Ovchinnikov, “Optical dipole traps for neutral atoms,” in, ser. *Advances In Atomic, Molecular, and Optical Physics*, B. Bederson and H. Walther, Eds., vol. 42, Academic Press, 2000, pp. 95 –170.